Weak localization with nonlinear bosonic matter waves

Timo Hartmann[a], Josef Michl[a], Cyril Petitjean[b,c], Thomas Wellens[d], Juan-Diego Urbina[a],
Klaus Richter[a], Peter Schlagheck[e]

[a]*Institut für Theoretische Physik, Universität Regensburg, 93040 Regensburg, Germany*
[b]*SPSMS-INAC-CEA, 17 Rue des Martyrs, 38054 Grenoble Cedex 9, France*
[c]*Laboratoire de Physique, ENS Lyon, 46, Allée d'Italie, 69007 Lyon, France*
[d]*Institut für Physik, Albert-Ludwigs-Universität Freiburg, Hermann-Herder-Str. 3, 79104 Freiburg, Germany*
[e]*Département de Physique, Université de Liège, 4000 Liège, Belgium*

Abstract

We investigate the coherent propagation of dilute atomic Bose-Einstein condensates through irregularly shaped billiard geometries that are attached to uniform incoming and outgoing waveguides. Using the mean-field description based on the nonlinear Gross-Pitaevskii equation, we develop a diagrammatic theory for the self-consistent stationary scattering state of the interacting condensate, which is combined with the semiclassical representation of the single-particle Green function in terms of chaotic classical trajectories within the billiard. This analytical approach predicts a universal dephasing of weak localization in the presence of a small interaction strength between the atoms, which is found to be in good agreement with the numerically computed reflection and transmission probabilities of the propagating condensate. The numerical simulation of this quasi-stationary scattering process indicates that this interaction-induced dephasing mechanism may give rise to a signature of weak antilocalization, which we attribute to the influence of non-universal short-path contributions.

Keywords:
weak localization, coherent backscattering, Bose-Einstein condensates, semiclassical theory, nonlinear wave propagation, quantum transport

1. Introduction

Recent technological advances in the manipulation of ultracold atoms on microscopic length scales have paved the way towards the exploration of scattering and transport phenomena with coherent interacting matter waves. Key experiments in this context include the creation of flexible waveguide geometries with optical dipole beams [1] and on atom chips [2, 3], the coherent propagation of Bose-Einstein condensed atoms in such waveguides by means of guided atom lasers [4, 5], the realization of optical billiard confinements [6, 7, 8] and microscopic scattering and disorder potentials for cold atoms [9, 10], as well as the detection of individual atoms within a condensate through photoionization on an atom chip [11]. Moreover, it was recently demonstrated [12] that artificial gauge potentials, which lead to a

breaking of time-reversal invariance in the same way as do magnetic fields for electrons, can be induced for cold atoms by means of Raman dressing with two laser beams that include a finite orbital angular momentum [13, 14, 15]. Together with the possibility of combining different atomic (bosonic and fermionic) species and of manipulating their interaction through Feshbach resonances, the combination of these tools gives rise to a number of possible scattering and transport scenarios that are now ready for experimental investigation.

A particularly prominent quantum transport phenomenon in mesoscopic physics is *weak localization* [16, 17]. This concept refers to an appreciable enhancement of the reflection (or, in the solid-state context, of the electronic resistance) in the presence of a two- or three-dimensional ballistic or disordered scattering region, as compared to the expectation based on a classical, i.e. incoherent, transport process. This enhancement, which in turn implies a reduction of the transmission (or of the electronic conductance) due to current conservation, is in particular caused by "coherent backscattering", i.e. by the constructive interference between backscattered classical paths and their time-reversed counterparts, which was first observed in experiments on the scattering of laser light from disordered media [18, 19]. In the solid-state context, weak localization is most conveniently detected by measuring the electronic conductance in dependence of a weak magnetic field that is oriented perpendicular to the scattering region, such that it causes a dephasing between backscattered paths and their time-reversed counterparts. A characteristic peak structure at zero magnetic field is then tyipcally observed [20, 21].

From the electronic point of view, the presence of interaction between the particles that participate at this scattering process is generally expected to give rise to an additional dephasing mechanism of this subtle interference phenomenon [22, 23, 24]. In the context of ultracold bosonic atoms, this expectation is partly confirmed by previous theoretical studies on the coherent propagation of an interacting Bose-Einstein condensate through a two-dimensional disorder potential [25], which employed numerical simulations as well as diagrammatic representations based on the mean-field description of the condensate in terms of the nonlinear Gross-Pitaevskii equation. This study did indeed reveal a reduction of the height of the coherent backscattering peak with increasing effective interaction strength between the atoms. It also predicted, however, that this coherent backscattering peak might turn into a *dip* at finite (but still rather small) interaction strengths [25]. This scenario is reminiscent of weak antilocalization due to spin-orbit interaction, which was observed in mesoscopic magnetotransport [26].

In order to gain a new perspective on this novel phenomenon, we investigate, in this work, the coherent propagation of Bose-Einstein condensates through ballistic scattering geometries that exhibit chaotic classical dynamics. Such propagation processes could be experimentally realized by guided atom lasers in which the optical waveguides are locally "deformed" by means of additional optical potentials (e.g. by focusing another red-detuned laser onto this waveguide). Alternatively, atom chips [2, 3] or atom-optical billiards [6, 7, 8] could be used in order to engineer chaotic scattering geometries for ultracold atoms. From the theoretical point of view, the wave transport through such scattering geometries can be described using the semiclassical representation of the Green function in terms of classical trajectories. The constructive intereference of reflected trajectories with their time-reversed

counterparts gives then rise to coherent backscattering [27], while a complete understanding of weak localization, in particular the corresponding reduction of the transmitted current, requires additional, classically correlated trajectory pairs [28, 29].

In order to account for the presence of atom-atom interaction on the mean-field level of the nonlinear Gross-Pitaevskii equation, we combine, in this paper, the semiclassical approach with the framework of nonlinear diagrammatic theory developed in Refs. [30, 31, 32]. For the sake of simplicity, we shall, as is described in Section 2, restrict ourselves to ideal chaotic billiard dynamics consisting of free motion that is confined by hard-wall boundaries. Since such billiard geometries give rise to uniform average densities within the scattering region, we can, as demonstrated in Sections 3 and 4, derive explicit analytical expressions for the retro-reflection and transmission probabilities as a function of the effective interaction strength. As shown in Section 5, these expressions agree very well with the numerically computed retro-reflection and transmission probabilities for two exemplary billiard geometries as far as the deviation from the case of noninteracting (single-particle) transport is concerned. On the absolute scale, however, the height of the weak localization peak is reduced in this noninteracting case by the presence of short-path contributions, in particular by self-retracing trajectories, which, as shown in Section 5, consequently turn this peak into a finite dip in the presence of a small interaction strength. We shall therefore argue in Section 6 that such short-path contributions are at the origin of this weak antilocalization-like phenomenon.

2. Setup of the nonlinear scattering process

We consider the quasistationary transport of coherent bosonic matter waves through two-dimensional waveguide structures that are perturbed by the presence of a wide quantum-dot-like scattering potential. Such propagating matter waves can be generated by means of a guided atom laser [4, 5] where ultracold atoms are coherently outcoupled from a trapping potential that contains a Bose-Einstein condensate. The control of the outcoupling process, which, e.g., can be achieved by applying a radiofrequency field that flips the spin of the atoms in the (magnetic) trap [4], permits one, in principle, to generate an energetically well-defined beam of atoms that propagate along the (horizontally oriented) waveguide in its transverse ground mode [33]. This waveguide, as well as the quantum-dot-like scattering potential, can be engineered by means of focused red-detuned laser beams which provide an attractive effective potential for the atoms that is proportional to their intensity. The restriction to two spatial dimensions can, furthermore, be realized by applying, in addition, a tight one-dimensional optical lattice perpendicular to the waveguide (i.e. oriented along the vertical direction).

The central object of study in this work is the phenomenon of weak localization. In the context of electronic mesoscopic physics, this quantum interference phenomenon can be detected by measuring the electronic conductance, which is directly related to the quantum transmission through the Landauer-Büttiker theory [34, 35, 36], as a function of the strength of an externally applied magnetic field which breaks time-reversal invariance within the scattering region. Such a time-reversal breaking mechanism can also be induced for cold atoms
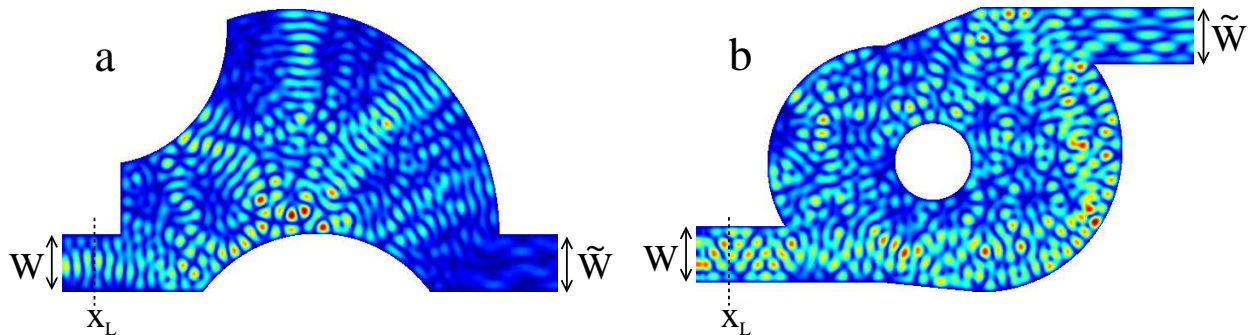
Figure 1: Shapes of the billiards a and b under consideration, plotted together with the density of a stationary scattering state. We indicate, in addition, the widths W and $\tilde{W}$ of the incident and the transmitted waveguides, respectively, as well as the horizontal position x_L at which the incident and reflected parts of the scattering wavefunction are decomposed in transverse eigenmodes of the waveguide. The semiclassical average that is undertaken in order to obtain the mean retro-reflection probability involves an average of the retro-reflection probability within a finite window of chemical potentials μ for different incident channels and different locations of the circular and the lower semicircular obstacle in the case of billiards a and b, respectively.

[12, 13, 14, 15], e.g., by coherently coupling two intra-atomic levels via a STIRAP process, using two laser beams of which one involves a nonvanishing orbital angular momentum [13]. This gives rise to an effective vector potential in the kinetic term of the Schrödinger equation, which is assumed such that it generates an effective "magnetic field" that is homogeneous within the scattering region and vanishes within the attached waveguides.

The main purpose of this study is to investigate how the scenario of weak localization is affected by the presence of a weak atom-atom interaction within the matter-wave beam. In lowest order in the interaction strength, the presence of such an atom-atom interaction is accounted for by a nonlinear contribution to the effective potential in the Schrödinger equation describing the motion of the atoms, which is proportional to the local density of atoms and which gives rise to the celebrated Gross-Pitaevskii equation [37]. The strength of this nonlinear contribution can be controlled by the scale of the confinement in the transverse (vertical) spatial direction. We shall make, in the following, the simplifying assumption that this nonlinearity is present only within the scattering region and vanishes within the waveguides. We furthermore assume that the waveguides are perfectly uniform, and that the two-dimensional scattering geometry can be described by perfect "billiard" potentials which combine a vanishing potential background within the waveguides and the scattering region with infinitely high hard walls along their boundaries. These assumptions considerably simplify the analytical and numerical treatment of the problem, and allow for the identification of well-defined asymptotic scattering states within the waveguides. Two such billiard configurations are shown in Fig. 1.

The dynamics of this matter-wave scattering process is then well modelled by an inho-

mogeneous two-dimensional Gross-Pitaevskii equation [38]

$$i\hbar\frac{\partial}{\partial t}\Psi(\mathbf{r},t) = \left[-\frac{1}{2m}\left(\frac{\hbar}{i}\nabla - \mathbf{A}(\mathbf{r})\right)^2 + V(\mathbf{r}) + g\frac{\hbar^2}{2m}|\Psi(\mathbf{r},t)|^2\right]\Psi(\mathbf{r},t) + S(\mathbf{r},t) \quad (1)$$

with $\mathbf{r} \equiv (x,y)$. Here m is the mass of the atoms and $V(\mathbf{r})$ represents the confinement potential that defines the waveguides and the scattering region. The effective vector potential $\mathbf{A}(\mathbf{r})$ vanishes within the waveguides. Within the scattering billiard we choose it as

$$\mathbf{A}(\mathbf{r}) \equiv \frac{1}{2}B\mathbf{e}_z \times (\mathbf{r} - \mathbf{r}_0) = \frac{1}{2}B[(x - x_0)\mathbf{e}_y - (y - y_0)\mathbf{e}_x] \quad (2)$$

where $\mathbf{r}_0 \equiv (x_0, y_0)$ represents an arbitrarily chosen reference point and $\mathbf{e}_x, \mathbf{e}_y, \mathbf{e}_z$ are the unit vectors in our spatial coordinate system. In the presence of an harmonic transverse (vertical) confinement with oscillation frequency $\omega_\perp \equiv \omega_\perp(\mathbf{r})$, the effective two-dimensional interaction strength is given by $g(\mathbf{r}) = 4\sqrt{2\pi}a_s/a_\perp(\mathbf{r})$ with $a_\perp(\mathbf{r}) \equiv \sqrt{\hbar/[m\omega_\perp(\mathbf{r})]}$ where a_s denotes the s-wave scattering length of the atoms. As stated above, we assume that g is constant within the billiard and vanishes in the waveguides.

The source amplitude $S(\mathbf{r},t)$ describes the coherent injection of atoms from the Bose-Einstein condensate within the reservoir trap. Assuming that only one transverse eigenmode in the waveguide is populated, we may write S as

$$S(\mathbf{r},t) = S_0\chi_i(y)\delta(x - x_L)\exp\left(-\frac{i}{\hbar}\mu t\right) \quad (3)$$

where $\chi_i(y)$ denotes the normalized wavefunction associated with the transverse eigenmode with the excitation index i, characterized by the energy E_i, into which the source injects the atoms from the condensate (typically one would attempt to achieve coherent injection into the transverse ground mode, with $i = 1$, in an atom-laser experiment [4]). x_L represents an arbitrary longitudinal coordinate within the waveguide (which, without loss of generality, is assumed to be oriented along the x axis) and μ is the chemical potential with which the atoms are injected into the waveguide. Making the ansatz

$$\Psi(\mathbf{r},t) \equiv \psi(\mathbf{r},t)\exp\left(-\frac{i}{\hbar}\mu t\right) \quad (4)$$

we obtain

$$i\hbar\frac{\partial}{\partial t}\psi(\mathbf{r},t) = (H - \mu)\psi(\mathbf{r},t) + g\frac{\hbar^2}{2m}|\psi(\mathbf{r},t)|^2\psi(\mathbf{r},t) + S_0\chi_i(y)\delta(x - x_L) \quad (5)$$

with the single-particle Hamiltonian

$$H = \frac{1}{2m}\left[\frac{\hbar}{i}\nabla - \mathbf{A}(\mathbf{r})\right]^2 + V(\mathbf{r})\,. \quad (6)$$

The time evolution of the scattering wavefunction can be considered to take place in the presence of an adiabatically slow increase of the source amplitude S_0 from zero to a given maximal value. In the absence of interaction, this process would necessarily lead to a stationary scattering state, whose decomposition into the transverse eigenmodes within the waveguides allows one to determine the associated channel-resolved reflection and transmission amplitudes. In the special case of a perfectly uniform waveguide without any scattering potential and in the absence of the vector potential $\mathbf{A}$, this stationary state is given by

$$\psi(x, y) = -i \frac{mS_0}{\hbar p_i^{\rm l}(\mu)} \chi_i(y) \exp\left[-\frac{i}{\hbar} p_i^{\rm l}(\mu) |x - x_L|\right] \qquad (7)$$

where $p_i^{\rm l}(\mu) \equiv \sqrt{2m\mu - E_i}$ denotes the longitudinal component of the momentum associated with the transverse mode χ_i. Such a stationary scattering state is, in general, not obtained in the presence of interaction. Indeed, a finite nonlinearity strength g may, in combination with a weak scattering potential, lead to a permanently time-dependent, turbulent-like flow across the scattering region [39, 40, 41, 25, 38], which in dimensionally restricted waveguide geometries should correspond to a loss of coherence on a microscopic level of the many-body scattering problem [38].

In the following, we shall restrict ourselves to rather small nonlinearities for which we still obtain, in most cases, stable quasistationary scattering states within the billiard under consideration [42]. In the subsequent two sections, we shall develop a semiclassical theory for the self-consistent scattering state that is obtained as a solution of Eq. (5). Section 3 focuses on contributions related to coherent backscattering, while loop corrections in next-to leading order in the inverse number of energetically accessible channels are taken into account in section 4.

3. Semiclassical theory of nonlinear coherent backscattering

3.1. Coherent backscattering in the linear case

The key ingredient of a semiclassical description of this nonlinear scattering process is the representation of the retarded quantum Green function

$$G_0(\mathbf{r}, \mathbf{r}', E) \equiv \langle \mathbf{r} | (E - H_0 + i0)^{-1} | \mathbf{r}' \rangle \qquad (8)$$

in terms of all classical (single-particle) trajectories $(\mathbf{p}_\gamma, \mathbf{q}_\gamma)(t)$ within the billiard, indexed by γ, that propagate from the initial point $\mathbf{r}'$ to the final point $\mathbf{r}$ at total energy E. Here, we deliberately exclude the vector potential $\mathbf{A}(\mathbf{r})$, i.e. the underlying Hamiltonian is given by

$$H_0 = \frac{\hat{\mathbf{p}}^2}{2m} + V(\mathbf{r}) \qquad (9)$$

where $\hat{\mathbf{p}} \equiv -i\hbar \nabla$ represents the quantum momentum operator. The semiclassical representation of the Green function can be derived from the Fourier transform of the quantum

propagator in Feynman's path integral representation, which is evaluated in the formal limit $\hbar \to 0$ using the method of stationary phase. It reads [43]

$$G_0(\mathbf{r}, \mathbf{r}', E) = \sum_\gamma A_\gamma(\mathbf{r}, \mathbf{r}', E) \exp\left[\frac{i}{\hbar} S_\gamma(\mathbf{r}, \mathbf{r}', E) - i\frac{\pi}{2}\mu_\gamma\right]. \tag{10}$$

Here,

$$S_\gamma(\mathbf{r}, \mathbf{r}', E) = \int_0^{T_\gamma} \mathbf{p}_\gamma(t) \cdot \dot{\mathbf{q}}_\gamma(t) dt \tag{11}$$

is the classical action integral along the trajectory γ (T_γ denotes the total propagation time from $\mathbf{r}'$ to $\mathbf{r}$), μ_γ represents the integer Maslov index that counts the number of conjugate points along the trajectory (which, in a billiard, also involves twice the number of bouncings at the walls, in addition to the number of conjugate points inside the billiard), and

$$A_\gamma(\mathbf{r}, \mathbf{r}', E) = \frac{2\pi}{\sqrt{2\pi i \hbar}^3} \sqrt{|\det D^2 S_\gamma(\mathbf{r}, \mathbf{r}', E)|} \tag{12}$$

is an amplitude that smoothly depends on $\mathbf{r}$ and $\mathbf{r}'$, with

$$|\det D^2 S_\gamma(\mathbf{r}, \mathbf{r}', E)| = \left|\det \frac{\partial(\mathbf{p}', \mathbf{r}', T)}{\partial(\mathbf{r}, \mathbf{r}', E)}\right|. \tag{13}$$

the Jacobian of the transformation from the initial phase space variables $(\mathbf{p}', \mathbf{r}')$ and the propagation time T to the final and initial positions $(\mathbf{r}, \mathbf{r}')$ and the energy E.

The presence of a weak effective magnetic field is now incorporated in a perturbative manner using the eikonal approximation. As shown in Appendix Appendix B, this yields the well-known modification of the Green function

$$G(\mathbf{r}, \mathbf{r}', E) = \sum_\gamma A_\gamma(\mathbf{r}, \mathbf{r}', E) \exp\left\{\frac{i}{\hbar}[S_\gamma(\mathbf{r}, \mathbf{r}', E) - \phi_\gamma(\mathbf{r}, \mathbf{r}', E)] - i\frac{\pi}{2}\mu_\gamma\right\} \tag{14}$$

with $\phi_\gamma(\mathbf{r}, \mathbf{r}', E) = -\varphi_\gamma(\mathbf{r}, \mathbf{r}', E) - \tilde{\varphi}_\gamma(\mathbf{r}, \mathbf{r}', E)$ and

$$\varphi_\gamma(\mathbf{r}, \mathbf{r}', E) \equiv \frac{1}{m}\int_0^{T_\gamma} \mathbf{p}_\gamma(t) \cdot \mathbf{A}[\mathbf{q}_\gamma(t)] dt, \tag{15}$$

$$\varphi_\gamma^{(d)}(\mathbf{r}, \mathbf{r}', E) \equiv -\frac{1}{2m}\int_0^{T_\gamma} \mathbf{A}^2[\mathbf{q}_\gamma(t)] dt \tag{16}$$

where the integration is peformed along the unperturbed trajectory $\mathbf{q}_\gamma(t)$. While the latter (diamagnetic) contribution $\varphi_\gamma^{(d)}$ gives only rise to a spatial modulation of the effective potential background within the billiard, the former (paramagnetic) contribution φ_γ explicitly breaks the time-reversal symmetry of the system and plays a crucial role for the intensity of coherent backscattering.

This expression for the Green function can be directly used in order to construct the scattering state $\psi(\mathbf{r})$ that arises as a stationary solution of Eq. (5). We obtain

$$\psi(\mathbf{r}) = S_0 \int G[\mathbf{r}, (x_L, y'), \mu] \chi_i(y') dy' \tag{17}$$

where χ_i represents the energetically lowest transverse eigenmode within the waveguide. Assuming billiard-like waveguides with a vanishing potential background and infinitely high hard walls along their boundaries, the nth normalized transverse eigenmode ($n > 0$) is given by

$$\chi_n(y) = \sqrt{\frac{2}{W}} \sin\left(\frac{p_n y}{\hbar}\right) = \frac{1}{2i} \sqrt{\frac{2}{W}} \left[\exp\left(\frac{i}{\hbar} p_n y\right) - \exp\left(-\frac{i}{\hbar} p_n y\right)\right] \text{ for } 0 \leq y \leq W \tag{18}$$

and $\chi_n(y) = 0$ otherwise. $p_n \equiv n\pi\hbar/W$ is the quantized transverse momentum and W represents the width of the waveguide. We can therefore write

$$\psi(\mathbf{r}) = \frac{S_0}{i} \sqrt{\frac{\pi\hbar}{W}} \left\{\overline{G}\left[\mathbf{r}, (x_L, p_i), \mu\right] - \overline{G}\left[\mathbf{r}, (x_L, -p_i), \mu\right]\right\} \tag{19}$$

where

$$\overline{G}[\mathbf{r}, (x', p_y'), E] \equiv \frac{1}{\sqrt{2\pi\hbar}} \int_0^W G[\mathbf{r}, (x', y'), E] \exp\left(\frac{i}{\hbar} p_y' y'\right) dy' \tag{20}$$

denotes a partial Fourier transform of $G[\mathbf{r}, (x', y'), E]$.

Inserting the semiclassical expression (14) for the Green function G, this partial Fourier transform can again be evaluated using the stationary phase approximation. The stationary phase condition yields $(\mathbf{p}_\gamma^i)_y[\mathbf{r}, (x', y'), E] = p_y'$, i.e. p_y' should be the y-component of the initial momentum of the trajectory. The integration over y' yields the prefactor $\sqrt{2\pi i\hbar/\alpha}$ with

$$\alpha \equiv \frac{\partial^2}{\partial y'^2} S_\gamma[\mathbf{r}, (x', y'), E] = -\frac{\partial[\mathbf{r}, (x', p_y'), E]}{\partial[\mathbf{r}, (x', y'), E]}. \tag{21}$$

Combining it with the prefactor $\sqrt{|\det D^2 S_\gamma|}$ according to the expression (13) and with the other prefactors that are contained within the amplitude A_γ, we finally obtain

$$\overline{G}(\mathbf{r}, \mathbf{z}', E) = \sum_\gamma \overline{A}_\gamma(\mathbf{r}, \mathbf{z}', E) \exp\left\{\frac{i}{\hbar}\left[\overline{S}_\gamma(\mathbf{r}, \mathbf{z}', E) - \overline{\phi}_\gamma(\mathbf{r}, \mathbf{z}', E)\right] - i\frac{\pi}{2}\overline{\mu}_\gamma\right\} \tag{22}$$

with

$$\overline{A}_\gamma(\mathbf{r}, \mathbf{z}', E) = \frac{2\pi\sqrt{i}}{\sqrt{2\pi i\hbar^3}} \sqrt{\left|\det \frac{\partial[\mathbf{p}', (x', y'), T]}{\partial[\mathbf{r}, (x', p_y'), E]}\right|}, \tag{23}$$

$$\overline{\mu}_\gamma = \mu_\gamma + \begin{cases} 1 : \frac{\partial^2}{\partial y'^2} S_\gamma(\mathbf{r}, \mathbf{r}', E) < 0 \\ 0 : \text{otherwise} \end{cases}, \tag{24}$$

$$\overline{S}_\gamma(\mathbf{r}, \mathbf{z}', E) = S_\gamma\left\{\mathbf{r}, \left[x', y_\gamma'(\mathbf{r}, \mathbf{z}', E)\right], E\right\} + p_y' y_\gamma'(\mathbf{r}, \mathbf{z}', E), \tag{25}$$

8

and $\overline{\phi}_\gamma(\mathbf{r}, \mathbf{z}', E)$ defined according to Eq. (B.9), where the initial phase-space point of the trajectories γ is given by the combination $\mathbf{z}' \equiv (x', p_y')$ and $y_\gamma'(\mathbf{r}, \mathbf{z}', E)$ denotes the resulting initial y coordinate.

Channel-resolved reflection and transmission amplitudes can now be computed by projecting ψ onto the transverse eigenmodes of the waveguides. This involves again a partial Fourier transform of the Green function, this time in the final coordinate. In particular, the reflection amplitude into channel n is obtained from

$$
\begin{aligned}
\psi_n &\equiv \int_0^W \chi_n^*(y) \psi(x_L, y) dy \qquad (26) \\
&= S_0 \frac{\pi\hbar}{W} \Big\{ \overline{\widetilde{G}}[(x_L, p_n), (x_L, p_i), \mu] - \overline{\widetilde{G}}[(x_L, p_n), (x_L, -p_i), \mu] \\
&\quad - \overline{\widetilde{G}}[(x_L, -p_n), (x_L, p_i), \mu] + \overline{\widetilde{G}}[(x_L, -p_n), (x_L, -p_i), \mu] \Big\} \\
&\equiv S_0 \frac{\pi\hbar}{W} \Big[\overline{\widetilde{G}}(\mathbf{z}_n^-, \mathbf{z}_1^+, \mu) - \overline{\widetilde{G}}(\mathbf{z}_n^+, \mathbf{z}_1^+, \mu) - \overline{\widetilde{G}}(\mathbf{z}_n^-, \mathbf{z}_1^-, \mu) + \overline{\widetilde{G}}(\mathbf{z}_n^+, \mathbf{z}_1^-, \mu) \Big] \qquad (27)
\end{aligned}
$$

with

$$
\widetilde{G}[(x, p_y), \mathbf{r}', E] \equiv \frac{1}{\sqrt{2\pi\hbar}} \int_0^W G[(x, y), \mathbf{r}', E] \exp\left(-\frac{i}{\hbar} p_y y \right) dy \,, \qquad (28)
$$

$$
\overline{\widetilde{G}}[(x, p_y), \mathbf{z}', E] \equiv \frac{1}{\sqrt{2\pi\hbar}} \int_0^W \overline{G}[(x, y), \mathbf{z}', E] \exp\left(-\frac{i}{\hbar} p_y y \right) dy \qquad (29)
$$

where we define

$$
\mathbf{z}_n^\pm \equiv \begin{cases} (x_L, \pm p_n) & \text{for incoming trajectories (with } p_x' > 0) \\ (x_L, \mp p_n) & \text{for outgoing trajectories (with } p_x < 0) \end{cases} . \qquad (30)
$$

Similarly as for $\overline{G}$, the semiclassical evaluation of this Fourier transform using Eq. (22) yields [27, 44, 45]

$$
\overline{\widetilde{G}}(\mathbf{z}, \mathbf{z}', E) = \sum_\gamma \overline{\widetilde{A}}_\gamma(\mathbf{z}, \mathbf{z}', E) \exp\left\{ \frac{i}{\hbar} \left[\overline{\widetilde{S}}_\gamma(\mathbf{z}, \mathbf{z}', E) - \overline{\widetilde{\phi}}_\gamma(\mathbf{z}, \mathbf{z}', E) \right] - i\frac{\pi}{2} \overline{\widetilde{\mu}}_\gamma \right\} \qquad (31)
$$

with

$$
\overline{\widetilde{A}}_\gamma(\mathbf{z}, \mathbf{z}', E) = \frac{2\pi i}{\sqrt{2\pi i \hbar}^3} \sqrt{\left| \det \frac{\partial[(p_x', p_y'), (x', y'), T]}{\partial[(x, p_y), (x', p_y'), E]} \right|} \,, \qquad (32)
$$

$$
\overline{\widetilde{\mu}}_\gamma = \overline{\mu}_\gamma + \begin{cases} 1 : \frac{\partial^2}{\partial y^2} \overline{S}_\gamma(\mathbf{r}, \mathbf{z}', E) < 0 \\ 0 : \text{otherwise} \end{cases} , \qquad (33)
$$

$$
\overline{\widetilde{S}}_\gamma(\mathbf{z}, \mathbf{z}', E) = \overline{S}_\gamma \{ [x, y_\gamma(\mathbf{z}, \mathbf{z}', E)], \mathbf{z}', E \} - p_y y_\gamma(\mathbf{z}, \mathbf{z}', E) \,, \qquad (34)
$$

and $\overline{\widetilde{\phi}}_\gamma(\mathbf{z}, \mathbf{z}', E)$ defined according to Eq. (B.9), where the final phase-space point of the trajectories γ is given by the combination $\mathbf{z} \equiv (x, p_y)$ (and y_γ is the final y coordinate).

9

From Eq. (31) it becomes obvious that subtle interferences between different classical trajectories may give rise to channel-resolved reflection and transmission probabilities that strongly fluctuate under variation of the incident chemical potential $\mu \equiv E$. Those fluctuations generally cancel, however, when performing an average within a finite window of chemical potentials. Specifically, the calculation of $|\psi_n|^2$ involves sums over pairs of trajectories γ and γ', whose contributions contain phase factors that depend on the difference $\widetilde{S}_\gamma - \widetilde{S}_{\gamma'}$ of the associated action integrals. These differences strongly vary with the chemical potential μ unless the two trajectories γ and γ' are somehow correlated.

An obvious correlation arises if the two trajectories happen to be identical, in which case the phase factor is unity. In the framework of the *diagonal approximation*, we only take into account this specific case, i.e., we approximate the double sum $\sum_{\gamma,\gamma'}$ by a single sum $\sum_\gamma$ where γ' is taken to be identical to γ. The energy average $\langle |\psi_n|^2 \rangle$ of $|\psi_n|^2$ is then given by

$$\langle |\psi_n|^2 \rangle \quad \simeq \quad \langle |\psi_n|^2 \rangle_{\mathrm{d}} \tag{35}$$

$$= \quad \left| S_0 \frac{\pi\hbar}{W} \right|^2 \left[\left\langle \left| \widetilde{\overline{G}}(\mathbf{z}_n^+, \mathbf{z}_1^+, \mu) \right|^2 \right\rangle_{\mathrm{d}} + \left\langle \left| \widetilde{\overline{G}}(\mathbf{z}_n^+, \mathbf{z}_1^-, \mu) \right|^2 \right\rangle_{\mathrm{d}} \right.$$

$$\left. + \left\langle \left| \widetilde{\overline{G}}(\mathbf{z}_n^-, \mathbf{z}_1^+, \mu) \right|^2 \right\rangle_{\mathrm{d}} + \left\langle \left| \widetilde{\overline{G}}(\mathbf{z}_n^-, \mathbf{z}_1^-, \mu) \right|^2 \right\rangle_{\mathrm{d}} \right] \tag{36}$$

with $\left\langle \left| \widetilde{\overline{G}}(\mathbf{z}, \mathbf{z}', E) \right|^2 \right\rangle_{\mathrm{d}} = \sum_\gamma \left\langle \left| \widetilde{\overline{A}}_\gamma(\mathbf{z}, \mathbf{z}', E) \right|^2 \right\rangle$.

As shown in Appendix Appendix C, this sum is evaluated using the generalized Hannay-Ozorio de Almeida sum rule [46, 47]. Defining by τ_D the "dwell time" of the system, i.e. the mean evolution time that a classical trajectory spends within the billiard before escaping to one of the waveguides, and introducing the "Heisenberg time" as $\tau_H \equiv m\Omega/\hbar$ where Ω denotes the area of the billiard, we obtain [see Eq. (C.15)]

$$\left\langle \left| \widetilde{\overline{G}}(\mathbf{z}, \mathbf{z}', E) \right|^2 \right\rangle_{\mathrm{d}} = \left(\frac{mW}{2\pi\hbar^2} \right)^2 \frac{\tau_D}{\tau_H} \frac{1}{\sqrt{2mE - p_y^2}} \frac{1}{\sqrt{2mE - p_y'^2}} . \tag{37}$$

Inserting this expression into Eq. (36) and defining

$$p_n^{\mathrm{l}}(E) \equiv \sqrt{2mE - p_n^2} = \sqrt{2mE - (n\pi\hbar/W)^2} \tag{38}$$

as the longitudinal component of the momentum that is associated with the transverse mode χ_n finally yields

$$\langle |\psi_n|^2 \rangle_{\mathrm{d}} = \left| \frac{mS_0}{\hbar} \right|^2 \frac{\tau_D}{\tau_H} \frac{1}{p_n^{\mathrm{l}}(\mu) p_i^{\mathrm{l}}(\mu)} . \tag{39}$$

This expression can be used in order to determine the steady current j_n of atoms that are reflected into channel n, according to

$$j_n = \frac{p_n^{\mathrm{l}}(\mu)}{m} \langle |\psi_n|^2 \rangle . \tag{40}$$

10

Dividing it by the incident current which is derived from Eq. (7) as

$$j^{\mathrm{i}} = \frac{m|S_0|^2}{\hbar^2 p_i^1(\mu)} ,$$ (41)

we obtain the reflection probability into channel n as

$$r_{ni} \equiv j_n/j^{\mathrm{i}} = \tau_D/\tau_H .$$ (42)

The same reasoning can be applied to the outgoing waveguide on the other, transmitted side of the billiard. Again we obtain $t_{ni} = \tau_D/\tau_H$ as the probability for transmission into the transverse channel n of the outgoing waveguide, even if its witdh $\tilde{W}$ is different from the width W of the incoming guide. The total reflection and transmission probabilities R and T are then simply related to the numbers of open channels N_c and $\tilde{N}_c$ in the incoming and outgoing waveguide according to $R = N_c \tau_D/\tau_H$ and $T = \tilde{N}_c \tau_D/\tau_H$, where we evaluate $N_c = 2W/\lambda_{\mathrm{dB}}$ and $\tilde{N}_c = 2\tilde{W}/\lambda_{\mathrm{dB}}$ in the semiclassical limit, with $\lambda_{\mathrm{dB}} \equiv 2\pi\hbar/\sqrt{2m\mu}$ the de Broglie wavelength of the atoms. We can furthermore use the general expression [27, 28]

$$\tau_D = \frac{\pi\Omega}{(W + \tilde{W})v}$$ (43)

for the mean survival time of a classical particle propagating with velocity v in a chaotic billiard with area Ω that contains two openings of width W and $\tilde{W}$, which yields

$$\frac{\tau_D}{\tau_H} = \frac{\lambda_{\mathrm{dB}}/2}{W + \tilde{W}} = \frac{1}{N_c + \tilde{N}_c} .$$ (44)

We then arrive at the intuitive results $R = W/(W + \tilde{W})$ and $T = \tilde{W}/(W + \tilde{W})$, i.e. the total reflection and transmission probabilities are simply given by the relative widths of the corresponding waveguides.

The diagonal approximation therefore yields predictions for reflection and transmission that are expected for incoherent, classical particles in a chaotic cavity. It represents in leading order in the inverse total channel number $(N_c + \tilde{N}_c)^{-1}$ the contributions for all channels on the transmitted side, and for all reflected channels except for the channel $n = i$ in which the matter-wave beam is injected into the billiard. In this incident channel, there is another, equally important possibility to pair the trajectories γ and γ' in the double sums that are involved in the calculation of $|\psi_i|^2$: γ' can be chosen to be the *time-reversed counterpart* of γ, the existence of which is guaranteed by the time-reversal symmetry of H_0.

Consequently, Eq. (35) has to be corrected for the special case $n = i$ according to

$$\langle |\psi_i|^2 \rangle \simeq \langle |\psi_i|^2 \rangle_{\mathrm{d}} + \langle |\psi_i|^2 \rangle_{\mathrm{c}}$$ (45)

where the "crossed" or "Cooperon"-type contribution

$$
\langle |\psi_i|^2 \rangle_{\mathrm{c}} = \left| S_0 \frac{\pi\hbar}{W} \right|^2 \left[\left\langle \left| \widetilde{G}(\mathbf{z}_i^+, \mathbf{z}_i^+, \mu) \right|^2 \right\rangle_{\mathrm{c}} + \left\langle \left| \widetilde{G}(\mathbf{z}_i^-, \mathbf{z}_i^-, \mu) \right|^2 \right\rangle_{\mathrm{c}} \right.
$$
$$
\left. + \left\langle \widetilde{G}^*(\mathbf{z}_i^+, \mathbf{z}_i^-, \mu) \widetilde{G}(\mathbf{z}_i^-, \mathbf{z}_i^+, \mu) \right\rangle_{\mathrm{c}} + \left\langle \widetilde{G}^*(\mathbf{z}_i^-, \mathbf{z}_i^+, \mu) \widetilde{G}(\mathbf{z}_i^+, \mathbf{z}_i^-, \mu) \right\rangle_{\mathrm{c}} \right] \quad (46)
$$

11

contains all those combinations of trajectories for which γ' is the time-reversed counterpart of γ. Obviously, the action integrals $\widetilde{\overline{S}}_\gamma$ and Maslov indices $\widetilde{\overline{\mu}}_\gamma$ are identical for the trajectories $\underline{\gamma}$ and their time-reversed counterparts. This is not the case, however, for the modification $\widetilde{\overline{\phi}}_\gamma$ of the action integral that is induced by the vector potential, whose paramagnetic part $\widetilde{\overline{\varphi}}_\gamma$ [Eq. (15)] changes sign when integrating along the trajectory γ in the opposite direction. We therefore obtain

$$\left\langle \widetilde{\overline{G}}^*(\mathbf{z}', \mathbf{z}, E) \, \widetilde{\overline{G}}(\mathbf{z}, \mathbf{z}', E) \right\rangle_{\mathrm{c}} = \sum_\gamma \left\langle \left| \widetilde{\overline{A}}_\gamma(\mathbf{z}, \mathbf{z}', E) \right|^2 \exp\left[\frac{2i}{\hbar}\widetilde{\overline{\varphi}}_\gamma(\mathbf{z}, \mathbf{z}', E)\right] \right\rangle . \qquad (47)$$

To provide some physical insight into the role of this additional phase factor, we use the representation (2) of the vector potential within the billiard. Using $\mathbf{p}_\gamma(t) = m\dot{\mathbf{q}}_\gamma(t)$ along trajectories γ generated by H_0, the paramagnetic contribution to the effective action integral reads then

$$\widetilde{\overline{\varphi}}_\gamma(\mathbf{z}, \mathbf{z}', E) = \frac{B}{2}\,\mathbf{e}_z \cdot \int_0^{T_\gamma} [\mathbf{q}_\gamma(t) - \mathbf{r}_0] \times \dot{\mathbf{q}}_\gamma(t)\,dt \qquad (48)$$

where $\mathbf{r}_0$ is an arbitrarily chosen reference point. Within the billiard, the trajectories $(\mathbf{p}_\gamma, \mathbf{q}_\gamma)(t)$ can be decomposed into segments of straight lines that connect subsequent reflection points at the billiard boundary. Denoting those reflection points by $\mathbf{q}_\gamma^{(1)}, \ldots, \mathbf{q}_\gamma^{(N-1)}$ and defining $\mathbf{q}_\gamma^{(0)} \equiv \mathbf{r}'$ and $\mathbf{q}_\gamma^{(N)} \equiv \mathbf{r}$, the initial and final points of the trajectory, we rewrite Eq. (48) as

$$\widetilde{\overline{\varphi}}_\gamma(\mathbf{z}, \mathbf{z}', E) = B \sum_{j=1}^N a_j \equiv B\mathcal{A} \qquad (49)$$

where

$$a_j = \frac{1}{2}\,\mathbf{e}_z \cdot \left[(\mathbf{q}_\gamma^{(j-1)} - \mathbf{r}_0) \times (\mathbf{q}_\gamma^{(j)} - \mathbf{r}_0)\right] \qquad (50)$$

is the directed area of the triangle spanned by the reflection points $\mathbf{q}_\gamma^{(j-1)}$ and $\mathbf{q}_\gamma^{(j)}$ as well as by the reference point $\mathbf{r}_0$. Quite obviously, $\widetilde{\overline{\varphi}}_\gamma$ is independent of the particular choice of $\mathbf{r}_0$, or of any other gauge transformation $\mathbf{A} \mapsto \mathbf{A} + \nabla\chi$ that vanishes within the waveguide, provided the initial and final points $\mathbf{r}'$ and $\mathbf{r}$ of the trajectory γ are identical or, less restrictively, lie both within the same, incident waveguide where the vector potential vanishes (in which case a straight-line integration $\int \mathbf{A} \cdot d\mathbf{q}$ from $\mathbf{r}'$ to $\mathbf{r}$ would formally close the trajectory without adding any further contribution to $\widetilde{\overline{\varphi}}_\gamma$).

The central limit theorem is now applied in order to obtain the probability distribution $P(T_\gamma, \mathcal{A})$ for accumulating the area $\mathcal{A}$ after the propagation time T_γ [27, 28, 44, 45]. We have

$$P(T_\gamma, \mathcal{A}) = \frac{1}{\sqrt{\pi\eta\Omega^{3/2}vT_\gamma}}\exp\left(-\frac{\mathcal{A}^2}{\eta\Omega^{3/2}vT_\gamma}\right) \qquad (51)$$

where Ω is the area of the billiard, v is the velocity of the particle, and η is a dimensionless scaling parameter that characterizes the geometry of the system and that can be numerically computed from the classical dynamics within the billiard as described in Appendix

Appendix D. This distribution is now used to obtain an average value of the magnetic phase factor according to

$$\left\langle \exp\left[\frac{2i}{\hbar}\widetilde{\overline{\varphi}}_\gamma(\mathbf{z}, \mathbf{z}', E)\right] \right\rangle = \int_{-\infty}^{+\infty} P(T_\gamma, \mathcal{A}) \exp\left(\frac{2i}{\hbar} B \mathcal{A}\right) d\mathcal{A} = \exp\left(-\frac{T_\gamma}{\tau_B}\right) \qquad (52)$$

with

$$\tau_B \equiv \frac{\hbar^2}{\eta \Omega^{3/2} v B^2} \qquad (53)$$

the characteristic time scale for magnetic dephasing.

With this information, we can now follow the derivation of the Hannay-Ozorio de Almeida sum rule, as explicited in Appendix Appendix C, in order to evaluate the expression (47), with the only complication that each contribution in the sum over trajectories needs to be weighted by the "dephasing" factor $\exp(-T_\gamma/\tau_B)$. This yields

$$\left\langle \widetilde{\overline{G}}^*(\mathbf{z}', \mathbf{z}, E) \widetilde{\overline{G}}(\mathbf{z}, \mathbf{z}', E) \right\rangle_{\mathrm{c}} = \left(\frac{mW}{2\pi\hbar^2}\right)^2 \left(\frac{\tau_H}{\tau_D} + \frac{\tau_H}{\tau_B}\right)^{-1} \frac{1}{\sqrt{2mE - p_y^2}} \frac{1}{\sqrt{2mE - p_y'^2}}. \qquad (54)$$

Hence, we obtain

$$\langle |\psi_i|^2 \rangle_{\mathrm{c}} = \left|\frac{mS_0}{\hbar p_i^1(\mu)}\right|^2 \left(\frac{\tau_H}{\tau_D} + \frac{\tau_H}{\tau_B}\right)^{-1} \qquad (55)$$

in very close analogy with Eq. (39), which altogether yields

$$\langle |\psi_i|^2 \rangle \simeq \langle |\psi_i|^2 \rangle_{\mathrm{d}} + \langle |\psi_i|^2 \rangle_{\mathrm{c}} = \left|\frac{mS_0}{\hbar p_i^1(\mu)}\right|^2 \left(1 + \frac{1}{1 + \tau_D/\tau_B}\right) \frac{\tau_D}{\tau_H}. \qquad (56)$$

This gives rise to an enhanced probability for retro-reflection into the incident channel $n = i$, namely

$$r_{ii} = \left(1 + \frac{1}{1 + \tau_D/\tau_B}\right) \frac{\tau_D}{\tau_H} = \left(1 + \frac{1}{1 + B^2/B_0^2}\right) \frac{\tau_D}{\tau_H} \qquad (57)$$

with

$$B_0 \equiv \frac{\hbar}{\sqrt{\eta v \tau_D \Omega^{3/2}}}, \qquad (58)$$

as compared to reflection into different channels described by Eq. (42), which is the characteristic signature of coherent backscattering. Note that, due to conservation of the total flux, increased retro-reflection for $n = i$ implies decreased reflection or transmission into other channels $n \neq i$. This will be subject of Section 4 below.

The above prediction (57) is expected to be valid for chaotic cavities in the semiclassical limit of small $\hbar$ (i.e. of a small de Broglie wavelength as compared to the size of the scattering region) and in the limit of small widths of the leads. Leads of finite widths, as the ones that are considered in the scattering geometries shown in Fig. 1, will give rise to non-universal corrections to Eq. (57) that are related to short reflected or transmitted paths. In particular,

the presence of *self-retracing* trajectories, which are identical to their time-reversed counterparts, affects the probability for retro-reflection due to coherent backscattering, as those trajectories are evidently doubly counted in the addition of ladder and crossed contributions. Hence, the enhancement of this retro-reflection probability with respect to the incoherent ladder background (42) will, in practice, be reduced as compared to Eq. (57), due to the presence of short and therefore semiclassically relevant self-retracing trajectories.

3.2. Diagrammatic representation of nonlinear scattering states

We now consider the presence of a weak interaction strength $g > 0$ in the Gross-Pitaevskii equation (5). As a consequence, the scattering process becomes nonlinear and the final (stationary or time-dependent) scattering state may depend on the "history" of the process, i.e. on the initial matter-wave population within the scattering region as well as on the specific ramping process of the source amplitude. We shall assume that the scattering region is initially empty (i.e., $\psi(\mathbf{r}, t) = 0$ for $t \to -\infty$) and that the source amplitude S_0 is adiabatically ramped from zero to a given maximal value $\tilde{S}_0$, on a time scale that is much larger than any other relevant time scale of the scattering system. This adiabatic ramping is formally expressed as $S_0(t) = \tilde{S}_0 f(t/t_R)$ where $f(\tau)$ is a real dimensionless function that monotonously increases from 0 (for $t \to -\infty$) to 1 (for $t \to \infty$) and $t_R \to \infty$ is a very large ramping time scale. Redefining $\psi(\mathbf{r}, t) \equiv f(t/t_R)\tilde{\psi}(\mathbf{r}, t)$ and neglecting terms of the order of $1/t_R$, we obtain from Eq. (5)

$$i\hbar\frac{\partial}{\partial t}\tilde{\psi}(\mathbf{r}, t) = (H - \mu)\tilde{\psi}(\mathbf{r}, t) + \tilde{S}(\mathbf{r}, t) \tag{59}$$

as effective Gross-Pitaevskii equation for $\tilde{\psi}$, with

$$\tilde{S}(\mathbf{r}, t) \equiv S_0\chi_i(y)\delta(x - x_L) + \tilde{g}(t)\frac{\hbar^2}{2m}|\tilde{\psi}(\mathbf{r}, t)|^2\tilde{\psi}(\mathbf{r}, t) \tag{60}$$

and $\tilde{g}(t) \equiv f^2(t/t_R)g$. For weak enough nonlinearities g and long enough ramping time scales t_R, Eq. (59) can be considered as describing an effectively linear scattering problem the source term of which is gradually adapted according to Eq. (60). We can therefore express the time-dependent scattering wavefunction as

$$\tilde{\psi}(\mathbf{r}, t) = \int d^2r' G(\mathbf{r}, \mathbf{r}', \mu)\tilde{S}(\mathbf{r}', t) \tag{61}$$

where $G \equiv (\mu - H + i0)^{-1}$ is the Green function of the linear scattering problem [see Eq. (14)]. In the limit of long evolution times $t \to \infty$, we thereby obtain

$$\psi(\mathbf{r}) = S_0\int G[\mathbf{r}, (x_L, y'), \mu]\chi_i(y')dy' + \int d^2r' G(\mathbf{r}, \mathbf{r}', \mu)g\frac{\hbar^2}{2m}|\psi(\mathbf{r}')|^2\psi(\mathbf{r}') \tag{62}$$

as self-consistent equation for the scattering wavefunction, which generalizes the expression (17) obtained for the linear case.

In rather close analogy with the numerical procedure that is employed for computing a stationary scattering state, we can construct a self-consistent solution of Eq. (62) by starting with the expression (17) for the linear case and by iteratively inserting the subsequent expressions obtained for $\psi(\mathbf{r})$ on the right-hand side of Eq. (62). This naturally leads to a power series in the nonlinearity,

$$\psi(\mathbf{r}) = \psi^{(0)}(\mathbf{r}) + \sum_{n=1}^{\infty} g^n \delta\psi^{(n)}(\mathbf{r}),\tag{63}$$

where $\psi^{(0)}(\mathbf{r})$ represents the solution of Eq. (17), i.e. the scattering state of the noninteracting system.

It is instructive to evaluate the semiclassical representation of the first-order correction to the linear scattering wavefunction $\psi^{(0)}$, given by

$$\delta\psi^{(1)}(\mathbf{r}) = \frac{\hbar^2}{2m} \int d^2r' G(\mathbf{r}, \mathbf{r}', \mu) |\psi^{(0)}(\mathbf{r}')|^2 \psi^{(0)}(\mathbf{r}').\tag{64}$$

Using the expression (19) for the scattering state of the noninteracting system, we obtain

$$\delta\psi^{(1)}(\mathbf{r}) = \frac{\hbar^2}{2m} \frac{S_0}{i} \sqrt{\frac{\pi\hbar}{W}} |S_0|^2 \frac{\pi\hbar}{W} \sum_{\nu_1,\nu_2,\nu_3=\pm 1} \nu_1\nu_2\nu_3$$
$$\times \int d^2r' G(\mathbf{r}, \mathbf{r}', \mu) \overline{G}(\mathbf{r}', \mathbf{z}_i^{\nu_1}, \mu) \overline{G}^*(\mathbf{r}', \mathbf{z}_i^{\nu_2}, \mu) \overline{G}(\mathbf{r}', \mathbf{z}_i^{\nu_3}, \mu)\tag{65}$$

with $\mathbf{z}_i^{\pm 1} \equiv \mathbf{z}_i^{\pm}$ as defined in Eq. (30). Inserting the semiclassical expansion for the Green function, given by Eqs. (14) and (22), yields

$$\delta\psi^{(1)}(\mathbf{r}) = \frac{\hbar^2}{2m} \frac{S_0}{i} \sqrt{\frac{\pi\hbar}{W}} |S_0|^2 \frac{\pi\hbar}{W} \sum_{\nu_1,\nu_2,\nu_3=\pm 1} \nu_1\nu_2\nu_3$$
$$\times \int d^2r' \sum_{\gamma_0} \sum_{\gamma_1,\gamma_2,\gamma_3} A_{\gamma_0}(\mathbf{r}, \mathbf{r}', \mu) \overline{A}_{\gamma_1}(\mathbf{r}', \mathbf{z}_i^{\nu_1}, \mu) \overline{A}^*_{\gamma_2}(\mathbf{r}', \mathbf{z}_i^{\nu_2}, \mu) \overline{A}_{\gamma_3}(\mathbf{r}', \mathbf{z}_i^{\nu_3}, \mu)$$
$$\times \exp\left\{\frac{i}{\hbar}\left[S_{\gamma_0}(\mathbf{r}, \mathbf{r}', \mu) + \overline{S}_{\gamma_1}(\mathbf{r}', \mathbf{z}_i^{\nu_1}, \mu) - \overline{S}_{\gamma_2}(\mathbf{r}', \mathbf{z}_i^{\nu_2}, \mu) + \overline{S}_{\gamma_3}(\mathbf{r}', \mathbf{z}_i^{\nu_3}, \mu)\right]\right\}$$
$$\times \exp\left\{-\frac{i}{\hbar}\left[\phi_{\gamma_0}(\mathbf{r}, \mathbf{r}', \mu) + \overline{\phi}_{\gamma_1}(\mathbf{r}', \mathbf{z}_i^{\nu_1}, \mu) - \overline{\phi}_{\gamma_2}(\mathbf{r}', \mathbf{z}_i^{\nu_2}, \mu) + \overline{\phi}_{\gamma_3}(\mathbf{r}', \mathbf{z}_i^{\nu_3}, \mu)\right]\right\}$$
$$\times \exp\left[-\frac{i\pi}{2}\left(\mu_{\gamma_0} + \overline{\mu}_{\gamma_1} - \overline{\mu}_{\gamma_2} + \overline{\mu}_{\gamma_3}\right)\right]\tag{66}$$

where the indices γ_0 and γ_ℓ ($\ell = 1, 2, 3$) represent trajectories that connect $\mathbf{r}'$ and $\mathbf{r}$ as well as $\mathbf{z}_i^{\nu_\ell}$ and $\mathbf{r}'$, respectively.

Neglecting, as done in Section 3, the modification of the trajectories γ_0 and $\gamma_{1/2/3}$ due to the presence of the weak magnetic field, a stationary-phase evaluation of the spatial integral in Eq. (66) yields the condition

$$\mathbf{p}^i_{\gamma_0}(\mathbf{r}, \mathbf{r}', \mu) + \mathbf{p}^f_{\gamma_2}(\mathbf{r}', \mathbf{z}_i^{\nu_2}, \mu) = \mathbf{p}^f_{\gamma_1}(\mathbf{r}', \mathbf{z}_i^{\nu_1}, \mu) + \mathbf{p}^f_{\gamma_3}(\mathbf{r}', \mathbf{z}_i^{\nu_3}, \mu).\tag{67}$$

Noting that all involved momenta are evaluated at the same spatial point $\mathbf{r}'$, this condition is satisfied if and only if

$$\mathbf{p}^{\mathrm{i}}_{\gamma_0}(\mathbf{r}, \mathbf{r}', \mu) = \mathbf{p}^{\mathrm{f}}_{\gamma_1}(\mathbf{r}', \mathbf{z}^{\nu_1}_i, \mu) \quad \text{and} \quad \mathbf{p}^{\mathrm{f}}_{\gamma_2}(\mathbf{r}', \mathbf{z}^{\nu_2}_i, \mu) = \mathbf{p}^{\mathrm{f}}_{\gamma_3}(\mathbf{r}', \mathbf{z}^{\nu_3}_i, \mu) \tag{68}$$

or

$$\mathbf{p}^{\mathrm{i}}_{\gamma_0}(\mathbf{r}, \mathbf{r}', \mu) = \mathbf{p}^{\mathrm{f}}_{\gamma_3}(\mathbf{r}', \mathbf{z}^{\nu_3}_i, \mu) \quad \text{and} \quad \mathbf{p}^{\mathrm{f}}_{\gamma_2}(\mathbf{r}', \mathbf{z}^{\nu_2}_i, \mu) = \mathbf{p}^{\mathrm{f}}_{\gamma_1}(\mathbf{r}', \mathbf{z}^{\nu_1}_i, \mu) \tag{69}$$

or

$$\mathbf{p}^{\mathrm{i}}_{\gamma_0}(\mathbf{r}, \mathbf{r}', \mu) = -\mathbf{p}^{\mathrm{f}}_{\gamma_2}(\mathbf{r}', \mathbf{z}^{\nu_2}_i, \mu) \quad \text{and} \quad \mathbf{p}^{\mathrm{f}}_{\gamma_1}(\mathbf{r}', \mathbf{z}^{\nu_1}_i, \mu) = -\mathbf{p}^{\mathrm{f}}_{\gamma_3}(\mathbf{r}', \mathbf{z}^{\nu_3}_i, \mu) \tag{70}$$

holds true. The cases (68) and (69) are essentially equivalent and imply , in case (68) [or in case (69)], that the trajectories γ_2 and γ_3 (or γ_2 and γ_1) are identical and that γ_0 represents the direct continuation of the trajectory γ_1 (or γ_3) from $\mathbf{r}'$ to $\mathbf{r}$. This latter condition determines the stationary points of $\mathbf{r}'$, which have to lie along the trajectories from $\mathbf{z}^{\nu_1}_i$ (or $\mathbf{z}^{\nu_3}_i$) to $\mathbf{r}$.

Case (70) is more involved. It implies, on the one hand, that the time-reversed counterpart of trajectory γ_3 represent the direct continuation of trajectory γ_1 (using the fact that the scattering system under consideration is, in the absence of the magnetic field, invariant with respect to time reversal), which determines the stationary points of $\mathbf{r}'$ along reflected trajectories from $\mathbf{z}^{\nu_1}_i$ to $\mathbf{z}^{\nu_3}_i$. On the other hand, γ_0 represents a part of the time-reversed counterpart of trajectory γ_2, which necessarily implies that the point of observation $\mathbf{r}$ has to lie along γ_2. This latter condition generally represents an additional restriction of the set of stationary points in Eq. (66) (namely that $\mathbf{r}'$ lie on the continuation of a trajectory from $\mathbf{z}^{\nu_2}_i$ to $\mathbf{r}$), which substantially reduces the weight of contributions resulting from case (70) as compared to those emanating from cases (68) and (69). An exception of this rule arises if the point of observation $\mathbf{r}$ is identical with or lies rather close to $\mathbf{z}^{\nu_2}_i$, in which case all contributions resulting from Eqs. (68)–(70) are of comparable order.

In full generality, we can express the first-order correction to the linear scattering wavefunction in the semiclassical regime as

$$\delta\psi^{(1)}(\mathbf{r}) = 2\delta\psi^{(1)}_\ell(\mathbf{r}) + \delta\psi^{(1)}_c(\mathbf{r}) \tag{71}$$

where $\delta\psi^{(1)}_\ell(\mathbf{r})$ and $\delta\psi^{(1)}_c(\mathbf{r})$ contain the contributions that respectively emanate from the cases (68), (69) as well as from the case (70). Considering an observation point $\mathbf{r}$ that lies deep inside the billiard, we neglect $\psi^{(1)}_c(\mathbf{r})$ for the moment. The expression for $\delta\psi^{(1)}_\ell(\mathbf{r})$ can be cast in a form that is, apart from a source-dependent prefactor, exactly equivalent to the first-order term in the Born series of a perturbed Green function, where the effective perturbation Hamiltonian δH corresponds here to the density $|\psi^{(0)}(\mathbf{r})|^2_{\mathrm{d}}$ of the noninteracting scattering wavefunction as evaluated by the diagonal approximation, i.e. to

$$|\psi^{(0)}(\mathbf{r})|^2_{\mathrm{d}} = |S_0|^2 \frac{\pi\hbar}{W} \left[\sum_\gamma \left| \overline{A}_\gamma(\mathbf{r}, \mathbf{z}^+_i, \mu) \right|^2 + \sum_\gamma \left| \overline{A}_\gamma(\mathbf{r}, \mathbf{z}^-_i, \mu) \right|^2 \right]. \tag{72}$$

16

In close analogy with the first-order modification (B.6) of the semiclassical Green function in the presence of a weak perturbation, we then obtain

$$
\delta\psi_\ell^{(1)}(\mathbf{r}) = \frac{S_0}{i}\sqrt{\frac{\pi\hbar}{W}}\sum_{\nu=\pm 1}\nu\sum_\gamma\left(-\frac{i}{\hbar}\right)\frac{\hbar^2}{2m}\int_0^{T_\gamma}|\psi^{(0)}[\mathbf{q}_\gamma(t)]|_{\mathrm{d}}^2\,dt
$$

$$
\times\overline{A}_\gamma(\mathbf{r},\mathbf{z}_i^\nu,\mu)\exp\left\{\frac{i}{\hbar}\left[\overline{S}_\gamma(\mathbf{r},\mathbf{z}_i^\nu,\mu)-\overline{\phi}_\gamma(\mathbf{r},\mathbf{z}_i^\nu,\mu)\right]-i\frac{\pi}{2}\overline{\mu}_\gamma\right\} \tag{73}
$$

$\delta\psi_\ell^{(1)}$ and $\delta\psi_c^{(1)}$ shall, in the following, be termed "ladder" and "crossed" contributions, respectively.

To illustrate this point, it is useful to introduce a diagrammatic representation for this nonlinear scattering problem. Following Ref. [32], we represent by ⟶▶ and ⟶▶ the Green function $G(\mathbf{r},\mathbf{r}',\mu)$ and its complex conjugate $G^*(\mathbf{r},\mathbf{r}',\mu)$, respectively. The (four-legged) vertex ■ represents a scattering event of ψ at its own density modulations, described by the second term of the right-hand side of Eq. (62), and ■ denotes the corresponding vertex for ψ^*, appearing in the complex conjugate counterpart of Eq. (62). The source is depicted by the vertical bar |, i.e. |⟶▶ represents the scattering wavefunction of the noninteracting system, given by the convolution of the Green function with the source. We can then express Eq. (62) and its complex conjugate as

$$\tag{74}$$

$$\tag{75}$$

where |⟶▶ and |⟶▶ respectively represent the self-consistent stationary scattering wavefunction $\psi(\mathbf{r})$ of the nonlinear system and its complex conjugate $\psi^*(\mathbf{r})$. Going up to the

second order in the power-series expansion (63), we obtain the diagrammatic representation

$$+ \, \mathcal{O}(g^3) \, . \qquad (76)$$

The semiclassical evaluation of the first-order term according to Eqs. (71) and (73), neglecting the contribution of $\delta\psi_c^{(1)}$, can be expressed as

$$\qquad (77)$$

in diagrammatic terms. In close analogy with the corresponding ladder diagrams in disordered systems [30, 31, 32], the parallel arrows ⟹ symbolize the semiclassical evaluation of G^*G in the diagonal approximation, with G and G^* following the same trajectories that connects a given initial with a given final point. The diagram ⊢▸■▸, on the other hand, indicates that the nonlinearity event takes place along a continuous trajectory that connects the source with a given final point at the end of the arrow. As already discussed above, the factor 2 in Eqs. (71) and (77) originates from the two equivalent conditions (68) and (69). In other words, the red arrow on the left-hand side of Eq. (77) can be paired with either one of the two incoming black arrows.

3.3. Ladder contributions

It is suggestive to pursue the analogy with the Born series of a linear Green function and to introduce a modified Green function G_ℓ (the ℓ stands for "ladder contributions"), symbolized by ⟹, in which the contribution of the density-induced perturbation is summed up to all orders in the nonlinearity g. The Dyson equation that this Green function satisfies is represented as

$$\qquad (78)$$

Applying the stationary phase approximation, the explicit expression for this modified Green function reads, in analogy with Eq. (B.8),

$$G_\ell(\mathbf{r}, \mathbf{r}', \mu) = \sum_\gamma A_\gamma(\mathbf{r}, \mathbf{r}', \mu) \exp\left\{ \frac{i}{\hbar} \left[S_\gamma(\mathbf{r}, \mathbf{r}', \mu) - \phi_\gamma(\mathbf{r}, \mathbf{r}', \mu) - \chi_\gamma(\mathbf{r}, \mathbf{r}', \mu) \right] - i\frac{\pi}{2}\mu_\gamma \right\} \quad (79)$$

with $\chi_\gamma(\mathbf{r}, \mathbf{r}', \mu) \equiv 2g(\hbar^2/2m) \int_0^{T_\gamma} |\psi^{(0)}[\mathbf{q}_\gamma(t)]|_\mathrm{d}^2\, dt$. On this level, the nonlinearity therefore induces an effective modification of the action integral along the trajectory γ, in close analogy with the change in action for the dynamics in the presence of a weak static disorder potential [48]. This modification, however, does not at all affect the calculation of mean densities within the billiard using the diagonal approximation: evaluating the wavefunction $\psi(\mathbf{r})$ according to Eq. (19) with $\overline{G}$ being replaced by $\overline{G}_\ell$, we would essentially obtain $|\psi(\mathbf{r})|_\mathrm{d}^2 = |\psi^{(0)}(\mathbf{r})|_\mathrm{d}^2$, the latter being given by Eq. (72) where the phases χ_γ appearing in Eq. (79) drop out.

The same reasoning applies if we replace $\psi^{(0)}$ by ψ in the definition of the nonlinearity-induced modification of the effective action associated with the trajectory γ, i.e., to (re-)define

$$\chi_\gamma(\mathbf{r}, \mathbf{r}', \mu) \equiv g\frac{\hbar^2}{m} \int_0^{T_\gamma} |\psi[\mathbf{q}_\gamma(t)]|_\mathrm{d}^2\, dt \quad (80)$$

and to use this expression in the definition of G_ℓ according to Eq. (79). This amounts to replacing the diagrammatic representation (78) by

$$\quad (81)$$

which, when being expanded in powers of g and evaluated using the stationary phase approximation, involves all possible ladder-type (parallel) pairings of G and G^*, i.e.,

$$\quad (82)$$

up to second order in g. The mean density within the billiard as evaluated using the diagonal approximation is then given by

$$|\psi(\mathbf{r})|_\mathrm{d}^2 = |S_0|^2 \frac{\pi\hbar}{W}\left[\sum_\gamma \left|\overline{A}_\gamma(\mathbf{r}, \mathbf{z}_i^+, \mu)\right|^2 + \sum_\gamma \left|\overline{A}_\gamma(\mathbf{r}, \mathbf{z}_i^-, \mu)\right|^2 \right] \quad (83)$$

19

as in the case of the linear scattering problem [see Eq. (72)] [49].

It is worthwhile to calculate the energy average of the density within the billiard using the Hannay-Ozorio de Almeida sum rule [47]. As shown in Appendix Appendix C, we have [see Eq. (C.13)]

$$\sum_\gamma \left\langle \left| \overline{A}_\gamma(\mathbf{r}, \mathbf{z}', \mu) \right|^2 \right\rangle = \frac{m^2 W}{2\pi\hbar^4} \frac{\tau_D}{\tau_H} \frac{1}{\sqrt{2m\mu - p_y'^2}}. \tag{84}$$

This eventually yields

$$\langle |\psi(\mathbf{r})|^2 \rangle_{\mathrm{d}} = \left| \frac{mS_0}{\hbar} \right|^2 \frac{\tau_D}{\tau_H} \frac{1}{\hbar p_i^1(\mu)} = \frac{mj^i}{\hbar} \frac{\tau_D}{\tau_H} = \frac{\tau_D}{\Omega} j^i \tag{85}$$

when being expressed in terms of the incident current $j^i = m|S_0|^2/[\hbar^2 p_i^1(\mu)]$. The mean density is therefore obtained from an equidistribution of the population in the case of a stationary flow, which is given by the ratio of the feeding rate j^i and the decay rate τ_D^{-1}.

3.4. Crossed contributions

As seen above, the nonlinear ladder contributions vanish on average. However, we have so far neglected the influence of terms arising from the association of trajectories according to the remaining (and less intuitive) case (70). As was argued above, the contributions of such terms to the local density is generally suppressed with respect to the ladder-type contributions arising from the cases (68) and (69), due to the fact that case (70) requires not only the time-reversed counterpart of trajectory γ_3 to represent the direct continuation of trajectory γ_1, but also that the point of observation $\mathbf{r}$ lie on the trajectory γ_2 connecting the source with the interaction point $\mathbf{r}'$. In the case of retro-reflection into the incident channel, however, where $\mathbf{r}$ lies directly at the location of the source, this latter condition is satisfied by default, and we should therefore expect a finite contribution from this "crossed" association of trajectories to the probability of coherent backscattering.

It is instructive to first compute the influence of such crossed terms in linear order in the nonlinearity. We evaluate for this purpose the remaining term $\delta\psi_c^{(1)}(\mathbf{r})$ in Eq. (71) that is associated with the case (70). The requirement that the time-reversed counterpart of γ_3 represent the direct continuation of γ_1 allows one to apply the stationary phase approximation in order to evaluate the spatial integral in Eq. (66). In close analogy with Eq. (73), we then obtain a single sum over all trajectories γ that connect the initial phase-space point $\mathbf{z}_i^{\nu_1}$ with the final point $\mathbf{z}_i^{\nu_3}$ ($\nu_1, \nu_3 = \pm 1$) both being associated with the incident channel $\chi_i(y)$. An important extension as compared to the structure of Eq. (73) is provided by the paramagnetic contribution (15) to the effective action integral, which changes its sign under the time-reversal of the trajectory γ_3.

Calculating the overlap of $\delta\psi_c^{(1)}(\mathbf{r})$ with the incident channel, we obtain the associated

first-order correction to the backscattering amplitude as

$$\delta\psi_i^{(c)} \equiv \int_0^W \chi_i^*(y)\delta\psi_c^{(1)}(x_L, y)dy \tag{86}$$

$$= S_0\frac{\pi\hbar}{W}\sum_{\nu_1,\nu_3=\pm1}(-\nu_1\nu_3)\sum_\gamma \widetilde{\overline{A}}_\gamma(\mathbf{z}_i^{\nu_3}, \mathbf{z}_i^{\nu_1}, \mu)$$

$$\times \exp\left\{\frac{i}{\hbar}\left[\widetilde{\overline{S}}_\gamma(\mathbf{z}_i^{\nu_3}, \mathbf{z}_i^{\nu_1}, \mu) - \widetilde{\overline{\phi}}_\gamma(\mathbf{z}_i^{\nu_3}, \mathbf{z}_i^{\nu_1}, \mu)\right] - i\frac{\pi}{2}\widetilde{\overline{\mu}}_\gamma\right\}$$

$$\times \left(-\frac{i}{\hbar}\right)\frac{\hbar^2}{2m}\int_0^{T_\gamma}C^{(0)}[\mathbf{q}_\gamma(t)]\exp\left\{-\frac{2i}{\hbar}\widetilde{\varphi}_\gamma[\mathbf{z}_i^{\nu_3}, \mathbf{q}_\gamma(t), \mu]\right\}dt \tag{87}$$

where we define

$$C^{(0)}(\mathbf{r}) = |S_0|^2\frac{\pi\hbar}{W}\left\{\sum_{\gamma_2}|\overline{A}_{\gamma_2}(\mathbf{r}, \mathbf{z}_i^+, \mu)|^2\exp\left[-\frac{2i}{\hbar}\overline{\varphi}_{\gamma_2}(\mathbf{r}, \mathbf{z}_i^+, \mu)\right]\right.$$

$$\left.+\sum_{\gamma_2}|\overline{A}_{\gamma_2}(\mathbf{r}, \mathbf{z}_i^-, \mu)|^2\exp\left[-\frac{2i}{\hbar}\overline{\varphi}_{\gamma_2}(\mathbf{r}, \mathbf{z}_i^-, \mu)\right]\right\} \tag{88}$$

as "crossed density" within the billiard. The latter quantity can be interpreted as the semiclassical evaluation of

$$\mathcal{C}^{(0)}(\mathbf{r}) = |S_0|^2\frac{\pi\hbar}{W}\left[\overline{G}^*(\mathbf{r}, \mathbf{z}_i^+, \mu)\widetilde{G}(\mathbf{z}_i^+, \mathbf{r}, \mu) + \overline{G}^*(\mathbf{r}, \mathbf{z}_i^-, \mu)\widetilde{G}(\mathbf{z}_i^-, \mathbf{r}, \mu)\right] \tag{89}$$

within the diagonal approximation. In contrast to the actual density within the billiard, given in leading order by the expression (83), $C^{(0)}(\mathbf{r})$ is, in general, not invariant under gauge transformations $\mathbf{A} \mapsto \mathbf{A} + \nabla\chi$ of the effective vector potential $\mathbf{A}(\mathbf{r})$, due to the presence of the phase factors containing the paramagnetic contribution to the effective action integral. The combination of those phase factors with the corresponding one arising in Eq. (87), however, gives rise to an overall expression that is invariant under gauge transformations.

To verify this, we introduce for each point $\mathbf{r}$ within the billiard a straight-line trajectory, denoted by the index ω, that connects this point to a fixed reference point $\mathbf{r}_L$ within the incident lead, given, e.g., by $\mathbf{r}_L \equiv (x_L, W/2)$. This straight-line trajectory can be defined as

$$\mathbf{q}_\omega(t) \equiv \mathbf{r} + \frac{t}{T_\omega}(\mathbf{r}_L - \mathbf{r}), \tag{90}$$

$$\mathbf{p}_\omega(t) \equiv \frac{\hbar}{T_\omega}(\mathbf{r}_L - \mathbf{r}), \tag{91}$$

with $T_\omega \equiv \hbar|\mathbf{r}_L - \mathbf{r}|/\sqrt{2m\mu}$ [50]. We now define for each "incident" trajectory γ, i.e. which connects a phase-space point $\mathbf{z}$ within the incident lead to a spatial point $\mathbf{r}$ within the billiard, its "completion" as $\bar\gamma \equiv \omega \circ \gamma$. In physical terms, $\bar\gamma$ traces the motion of a particle that follows γ and is then scattered back to the incident lead due to the presence of a local

perturbation within the billiard (a point scatterer) at position $\mathbf{r}$. We obviously have the relation

$$\overline{\varphi}_{\bar{\gamma}}(\mathbf{r}_L, \mathbf{r}, \mathbf{z}, \mu) = \varphi_\omega(\mathbf{r}_L, \mathbf{r}, \mu) + \overline{\varphi}_\gamma(\mathbf{r}, \mathbf{z}, \mu) \tag{92}$$

for the paramagnetic action integral along the trajectory $\bar{\gamma}$. As integrations of $\mathbf{p}(t) \cdot \mathbf{A}[\mathbf{q}(t)]$ along paths that are entirely contained within the incident lead obviously vanish due to the local absence of the vector potential, we can state that $\overline{\varphi}_{\bar{\gamma}}(\mathbf{r}_L, \mathbf{r}, \mathbf{z}, \mu)$ is invariant under gauge transformations. Analogously, a trajectory γ' that leads from a spatial point $\mathbf{r}$ within the billiard to a phase-space point $\mathbf{z}$ within the incident lead is "completed" as $\bar{\gamma}' \equiv \gamma' \circ \omega$ with the associated paramagnetic action integral

$$\widetilde{\varphi}_{\bar{\gamma}'}(\mathbf{z}, \mathbf{r}, \mathbf{r}_L, \mu) = \widetilde{\varphi}_{\gamma'}(\mathbf{z}, \mathbf{r}, \mu) + \varphi_\omega(\mathbf{r}, \mathbf{r}_L, \mu) . \tag{93}$$

The crossed density (88) can therefore be re-expressed in terms of such completed trajectories $\bar{\gamma}_2$ through

$$C^{(0)}(\mathbf{r}) = c^{(0)}(\mathbf{r}) \exp\left[\frac{2i}{\hbar} \varphi_\omega(\mathbf{r}_L, \mathbf{r}, \mu)\right] \tag{94}$$

where its gauge-invariant part is introduced as

$$
\begin{aligned}
c^{(0)}(\mathbf{r}) \;\equiv\; |S_0|^2 \frac{\pi\hbar}{W} &\left\{ \sum_{\gamma_2} \left|\overline{A}_{\gamma_2}(\mathbf{r}_L, \mathbf{r}, \mathbf{z}_i^+, \mu)\right|^2 \exp\left[-\frac{2i}{\hbar}\overline{\varphi}_{\bar{\gamma}_2}(\mathbf{r}_L, \mathbf{r}, \mathbf{z}_i^+, \mu)\right] \right. \\
&\left. + \sum_{\gamma_2} \left|\overline{A}_{\gamma_2}(\mathbf{r}_L, \mathbf{r}, \mathbf{z}_i^-, \mu)\right|^2 \exp\left[-\frac{2i}{\hbar}\overline{\varphi}_{\bar{\gamma}_2}(\mathbf{r}_L, \mathbf{r}, \mathbf{z}_i^-, \mu)\right] \right\} .
\end{aligned}
\tag{95}
$$

As in the case of "ordinary" backscattering trajectories, the energy average of the paramagnetic phase factor of $\bar{\gamma}$ yields, in analogy with Eq. (52),

$$\left\langle \exp\left[-\frac{2i}{\hbar}\overline{\varphi}_{\bar{\gamma}}(\mathbf{r}_L, \mathbf{r}, \mathbf{z}, \mu)\right]\right\rangle = \exp\left(-\frac{T_\gamma}{\tau_B}\right) \tag{96}$$

with τ_B the characteristic time scale associated with the magnetic field, defined by Eq. (53). We neglect in this expression the contribution of T_ω to the total propagation time of $\bar{\gamma}$ (which is, in fact, canceled in the nonlinear diagrams contributing to the backscattering probability to be discussed below, as the latter involve, by construction, flux integrals along closed paths) and assume $T_{\bar{\gamma}} \simeq T_\gamma$. In perfect analogy with the derivation of the energy-averaged density within the billiard, we then obtain [see Eqs. (C.8) and (C.13)]

$$\left\langle c^{(0)}(\mathbf{r})\right\rangle = \left|\frac{mS_0}{\hbar}\right|^2 \left(\frac{\tau_H}{\tau_D} + \frac{\tau_H}{\tau_B}\right)^{-1} \frac{1}{\hbar p_i^1(\mu)} = \frac{\tau_D}{\tau_H} \frac{1}{1 + \tau_D/\tau_B} \frac{m}{\hbar} j^{\mathrm{i}} \equiv \left\langle c^{(0)}\right\rangle \tag{97}$$

for the energy average of the gauge-invariant part of the crossed density.

This expression can be used in order to evaluate the first-order correction to the crossed contribution $\langle|\psi_i|^2\rangle_c^{(g)}$ of the nonlinear backscattering probability according to

$$\langle|\psi_i|^2\rangle_c^{(g)} = \langle|\psi_i|^2\rangle_c^{(0)} + g\left[\left\langle\psi_i^* \delta\psi_i^{(c)}\right\rangle + \left\langle\left(\delta\psi_i^{(c)}\right)^* \psi_i\right\rangle\right] + \mathcal{O}(g^2) \tag{98}$$

where $\langle|\psi_i|^2\rangle_c^{(0)}$ represents the linear crossed contribution as defined in Eq. (46). Within the diagonal approximation, we obtain

$$\left\langle \psi_i^* \delta\psi_i^{(c)} \right\rangle = -\frac{i}{\hbar}\frac{\hbar^2}{2m}\left|S_0\frac{\pi\hbar}{W}\right|^2 \sum_{\nu_1,\nu_3=\pm 1}\sum_\gamma \left\langle \left|\widetilde{\overline{A}}_\gamma(\mathbf{z}_i^{\nu_3},\mathbf{z}_i^{\nu_1},\mu)\right|^2\right\rangle \int_0^{T_\gamma} dt \left\langle c^{(0)}[\mathbf{q}_\gamma(t)]\right\rangle$$

$$\times \left\langle \exp\left\{-\frac{2i}{\hbar}\widetilde{\varphi}_{\bar\gamma}[\mathbf{z}_i^{\nu_3},\mathbf{q}_\gamma(t),\mathbf{r}_L,\mu]\right\} + \exp\left\{\frac{2i}{\hbar}\overline{\varphi}_{\bar\gamma}[\mathbf{r}_L,\mathbf{q}_\gamma(t),\mathbf{z}_i^{\nu_1},\mu]\right\}\right\rangle \quad (99)$$

where, in the second line of Eq. (99), we account for the fact that each trajectory γ can be paired with itself as well as with its time-reversed counterpart, the latter giving rise to a different paramagnetic phase factor. For both possibilities of the pairing, the remaining piece of the trajectory γ, respecively connecting $\mathbf{q}_\gamma(t)$ with $\mathbf{z}_i^{\nu_3}$ as well as $\mathbf{z}_i^{\nu_1}$ with $\mathbf{q}_\gamma(t)$, can be "completed" by combining it with the straight-line trajectory ω from $\mathbf{q}_\gamma(t)$ to r_L that is introduced through the factorization (94).

We can now perform the energy average of the paramagnetic phase factors according to Eq. (96), taking into account that the effective propagation times of the pieces of trajectories under consideration equal $T_\gamma - t$ as well as t, respectively, for the two phase factors appearing in the second line of Eq. (99) (the additional contribution of the straight-line trajectory ω to the total propagation time is neglected). This gives, for both phase factors, rise to integrals that are straightforwardly evaluated as

$$\int_0^{T_\gamma} \exp\left(-\frac{t}{\tau_B}\right) dt = \tau_B\left[1 - \exp\left(-\frac{T_\gamma}{\tau_B}\right)\right]. \quad (100)$$

We therefore obtain

$$\left\langle \psi_i^* \delta\psi_i^{(c)} \right\rangle = -\frac{i}{\hbar}\frac{\hbar^2}{2m}\left|S_0\frac{\pi\hbar}{W}\right|^2 \left\langle c^{(0)}\right\rangle \sum_{\nu_1,\nu_3=\pm 1} 2\tau_B \sum_\gamma \left\langle\left|\widetilde{\overline{A}}_\gamma(\mathbf{z}_i^{\nu_3},\mathbf{z}_i^{\nu_1},\mu)\right|^2\right\rangle\left[1 - \exp\left(-\frac{T_\gamma}{\tau_B}\right)\right]$$

$$(101)$$

which, after applying the Hannay-Ozorio de Almeida sum rule [see Eq. (C.15)], is evaluated as

$$\left\langle \psi_i^* \delta\psi_i^{(c)} \right\rangle = -i\left|\frac{mS_0}{\hbar p_i^1(\mu)}\right|^4 \left(\frac{\tau_H}{\tau_D} + \frac{\tau_H}{\tau_B}\right)^{-2}\frac{p_i^1(\mu)\tau_D}{m} \quad (102)$$

using the expression (97) for the average of the crossed density $\left\langle c^{(0)}\right\rangle$. As this expression is purely imaginary, the modification of the backscattering probability due to the presence of the nonlinearity vanishes in first order in g, as seen from Eq. (98).

Going beyond the first order in g, we can express the full nonlinear coherent backscattering probability, as evaluated using the semiclassical stationary phase approximation, in

diagrammatic terms according to

$$\text{(diagram)} = \text{(diagram)} + \text{(diagram)} + \text{(diagram)} + \text{(diagram)} + 2\,\text{(diagram)} + 2\,\text{(diagram)} + \mathcal{O}(g^3)\,. \quad (103)$$

Here, $\longrightarrow$ represents, according to Eq. (81), the modified Green function G_ℓ due to the inclusion of ladder contributions. All types of ladder diagrams that were discussed in the previous subsection 3.3 are therefore implicitly included in this representation. As in Eq. (82), the prefactors 2 symbolize the fact that two different possibilities of pairings have to be counted for certain diagrams.

In analogy with the derivation undertaken in Ref. [32], this series of diagrams can be exactly summed yielding

$$\text{(diagram)} = \text{(diagram)} + \text{(diagram)} + \text{(diagram)} + \text{(diagram)} \quad (104)$$

where we define the nonlinear crossed density $\longleftrightarrow$ and its complex conjugate $\longleftrightarrow$ in a self-consistent manner through

$$\text{(diagram)} = \text{(diagram)} + 2\,\text{(diagram)}\,, \quad (105)$$

$$\text{(diagram)} = \text{(diagram)} + 2\,\text{(diagram)}\,, \quad (106)$$

This nonlinear crossed density can be expressed through a transport equation of the form

$$
\begin{aligned}
C^{(g)}(\mathbf{r}) &= C^{(0)}(\mathbf{r}) + 2g\frac{\hbar^2}{2m}|S_0|^2\frac{\pi\hbar}{W}\sum_{\nu_1,\nu_2=\pm1}\nu_1\nu_2 \\
&\times \int d^2r'\, C^{(g)}(\mathbf{r}')G_\ell(\mathbf{r}',\mathbf{r},\mu)\overline{G}_\ell(\mathbf{r}',\mathbf{z}_i^{\nu_1},\mu)\overline{G}_\ell^*(\mathbf{r},\mathbf{z}_i^{\nu_2},\mu)
\end{aligned}
\tag{107}
$$

which involves the modified Green function (79) that takes into account the average shift of the effective potential within the billiard due to the presence of the nonlinearity. Being invariant under time-reversal, the nonlinearity-induced contribution χ_γ (80) to the action integral does not play any role for the determination of the nonlinear crossed density. Indeed, applying the stationary phase and diagonal approximations in Eq. (107), we obtain

$$
\begin{aligned}
C^{(g)}(\mathbf{r}) &= C^{(0)}(\mathbf{r}) + g|S_0|^2\frac{\pi\hbar^3}{mW}\sum_{\nu=\pm1}\left|\overline{A}_\gamma(\mathbf{r},\mathbf{z}_i^\nu,\mu)\right|^2 \\
&\times \left(-\frac{i}{\hbar}\right)\int_0^{T_\gamma}C^{(g)}[\mathbf{q}_\gamma(t)]\exp\left\{-\frac{2i}{\hbar}\varphi_\gamma[\mathbf{r},\mathbf{q}_\gamma(t),\mu]\right\}dt
\end{aligned}
\tag{108}
$$

which does not involve any reference to χ_γ.

Quite obviously, the nonlinear crossed density $C^{(g)}(\mathbf{r})$ is not invariant under gauge transformations of the effective vector potential. In perfect analogy with $C^{(0)}(\mathbf{r})$, however, we can describe the explicit gauge dependence of $C^{(g)}(\mathbf{r})$ in terms of a phase factor that contains the paramagnetic contribution of a straight-line trajectory ω from $\mathbf{r}$ to the reference point $\mathbf{r}_L$ within the incident lead [50]. In analogy with Eq. (94), we therefore propose

$$
C^{(g)}(\mathbf{r}) \equiv c^{(g)}(\mathbf{r})\exp\left[\frac{2i}{\hbar}\varphi_\omega(\mathbf{r}_L,\mathbf{r},\mu)\right]
\tag{109}
$$

as definition for the gauge-invariant part $c^{(g)}(\mathbf{r})$ of the nonlinear crossed density, which in turn satisfies the gauge-invariant transport equation

$$
\begin{aligned}
c^{(g)}(\mathbf{r}) &= c^{(0)}(\mathbf{r}) + g|S_0|^2\frac{\pi\hbar^3}{mW}\sum_{\nu=\pm1}\left|\overline{A}_\gamma(\mathbf{r},\mathbf{z}_i^\nu,\mu)\right|^2 \\
&\times \left(-\frac{i}{\hbar}\right)\int_0^{T_\gamma}c^{(g)}[\mathbf{q}_\gamma(t)]\exp\left\{-\frac{2i}{\hbar}\varphi_{\bar\gamma}[\mathbf{r},\mathbf{q}_\gamma(t),\mathbf{r}_L,\mu]\right\}dt\ .
\end{aligned}
\tag{110}
$$

We can now compute the energy average of $c^{(g)}(\mathbf{r})$ by assuming that it is, as the one for $c^{(0)}(\mathbf{r})$ [see Eq. (97)], independent of the position $\mathbf{r}$ within the billiard, which is to be verified *a posteriori*. Using Eqs. (96), (97), and (100), (C.8), and (C.13), we obtain

$$
\begin{aligned}
\left\langle c^{(g)}\right\rangle &= \left\langle c^{(0)}\right\rangle - ig|S_0|^2\frac{\pi\hbar^2}{mW}\left\langle c^{(g)}\right\rangle\sum_{\nu=\pm1}\sum_\gamma\left\langle\left|\overline{A}_\gamma(\mathbf{r},\mathbf{z}_i^\nu,\mu)\right|^2\right\rangle\left[1-\exp\left(-\frac{T_\gamma}{\tau_B}\right)\right] \\
&= \left\langle c^{(0)}\right\rangle - ig\frac{\hbar\tau_D}{m}\left|\frac{mS_0}{\hbar}\right|^2\left(\frac{\tau_H}{\tau_D}+\frac{\tau_H}{\tau_B}\right)^{-1}\frac{1}{\hbar p_i^l(\mu)}\left\langle c^{(g)}\right\rangle \\
&= \left\langle c^{(0)}\right\rangle - ig\frac{\hbar\tau_D}{m}\left\langle c^{(0)}\right\rangle\left\langle c^{(g)}\right\rangle
\end{aligned}
\tag{111}
$$

which is straightforwardly solved as

$$\left\langle c^{(g)} \right\rangle = \frac{\left\langle c^{(0)} \right\rangle}{1 + ig\tau_D \frac{\hbar}{m} \left\langle c^{(0)} \right\rangle} . \tag{112}$$

We are now in a position to evaluate the full nonlinear coherent backscattering probability according to the diagrammatic representation (104). Denoting the linear crossed contribution to the backscattering probability by

$$c_{ii}^{(0)} \equiv \left| \frac{\hbar p_i^l(\mu)}{m S_0} \right|^2 \left\langle |\psi_i|^2 \right\rangle_c = \left(\frac{\tau_H}{\tau_D} + \frac{\tau_H}{\tau_B} \right)^{-1} \tag{113}$$

we have, as a generalization of Eq. (57),

$$r_{ii} = \frac{\tau_D}{\tau_H} + c_{ii}^{(g)} \tag{114}$$

with

$$c_{ii}^{(g)} = c_{ii}^{(0)} + \left(\frac{\pi \hbar^2 p_i^l(\mu)}{mW} \right)^2 \left\langle g\delta c_{ii}^{(1)} + g\left(\delta c_{ii}^{(1)}\right)^* + g^2 \delta c_{ii}^{(2)} \right\rangle \tag{115}$$

where we introduce

$$\delta c_{ii}^{(1)} = \frac{\hbar^2}{2m} \sum_{\nu_1,\nu_2,\nu_3,\nu_4=\pm 1} \nu_1\nu_2\nu_3\nu_4 \int d^2r\, C^{(g)}(\mathbf{r}) \overline{G}_\ell(\mathbf{r}, \mathbf{z}_i^{\nu_1}, \mu) \overline{G}_\ell(\mathbf{r}, \mathbf{z}_i^{\nu_2}, \mu) \widetilde{\overline{G}}_\ell^*(\mathbf{z}_i^{\nu_3}, \mathbf{z}_i^{\nu_4}, \mu) \tag{116}$$

and

$$\begin{aligned}
\delta c_{ii}^{(2)} &= \left(\frac{\hbar^2}{2m} \right)^2 \sum_{\nu_1,\nu_2,\nu_3,\nu_4=\pm 1} \nu_1\nu_2\nu_3\nu_4 \int d^2r\, C^{(g)}(\mathbf{r}) \overline{G}_\ell(\mathbf{r}, \mathbf{z}_i^{\nu_1}, \mu) \overline{G}_\ell(\mathbf{r}, \mathbf{z}_i^{\nu_2}, \mu) \\
&\quad \times \int d^2r'\, \left[C^{(g)}(\mathbf{r}') \right]^* \overline{G}_\ell^*(\mathbf{r}', \mathbf{z}_i^{\nu_3}, \mu) \overline{G}_\ell^*(\mathbf{r}', \mathbf{z}_i^{\nu_4}, \mu)
\end{aligned} \tag{117}$$

as contributions that result from the nonlinear diagrams in Eq. (104). Again, stationary phase and diagonal approximations are employed in order to evaluate these contributions, and we also use Eqs. (109) and (112) in order to express the nonlinear crossed density $C^{(g)}(\mathbf{r})$. This yields for the energy average

$$\begin{aligned}
\left\langle \delta c_{ii}^{(1)} \right\rangle &= -i\frac{\hbar}{2m} \left\langle c^{(g)} \right\rangle \sum_{\nu_1,\nu_2} \sum_\gamma \left\langle \left| \widetilde{\overline{A}}_\gamma(\mathbf{z}_i^{\nu_1}, \mathbf{z}_i^{\nu_2}, \mu) \right|^2 \right\rangle \\
&\quad \times \int_0^{T_\gamma} dt \left\langle \exp\left\{ -\frac{2i}{\hbar} \widetilde{\varphi}_{\bar{\gamma}}[\mathbf{z}_i^{\nu_1}, \mathbf{q}_\gamma(t), \mathbf{r}_L, \mu] \right\} + \exp\left\{ \frac{2i}{\hbar} \overline{\varphi}_{\bar{\gamma}}[\mathbf{r}_L, \mathbf{q}_\gamma(t), \mathbf{z}_i^{\nu_2}, \mu] \right\} \right\rangle \\
&= -i\frac{\hbar\tau_D}{m} \left\langle c^{(g)} \right\rangle \left(\frac{mW}{\pi\hbar^2 p_i^l(\mu)} \right)^2 \left(\frac{\tau_H}{\tau_D} + \frac{\tau_H}{\tau_B} \right)^{-1}
\end{aligned} \tag{118, 119}$$

26

(the real part of which is nonzero due to the fact that $\left\langle c^{(g)} \right\rangle$ is complex) and

$$
\left\langle \delta c_{ii}^{(2)} \right\rangle = \frac{\hbar^2}{2m^2} \left| \left\langle c^{(g)} \right\rangle \right|^2 \sum_{\nu_1,\nu_2} \sum_{\gamma} \left\langle \left| \widetilde{\overline{A}}_\gamma(\mathbf{z}_i^{\nu_1}, \mathbf{z}_i^{\nu_2}, \mu) \right|^2 \right\rangle \tag{120}
$$

$$
\times \int_0^{T_\gamma} dt \int_0^{T_\gamma} dt' \left\langle \exp\left\{ -\frac{2i}{\hbar} \overline{\varphi}_{\bar\gamma}[\mathbf{r}_L, \mathbf{q}_\gamma(t), \mathbf{z}_i^{\nu_2}, \mu] + \frac{2i}{\hbar} \overline{\varphi}_{\bar\gamma}[\mathbf{r}_L, \mathbf{q}_\gamma(t'), \mathbf{z}_i^{\nu_2}, \mu] \right\} \right\rangle
$$

$$
= \frac{\hbar^2 \tau_D^2}{m^2} \left| \left\langle c^{(g)} \right\rangle \right|^2 \left(\frac{mW}{\pi\hbar^2 p_i^1(\mu)} \right)^2 \left(\frac{\tau_H}{\tau_D} + \frac{\tau_H}{\tau_B} \right)^{-1} \tag{121}
$$

where we evaluate

$$
\int_0^{T_\gamma} dt \int_0^{T_\gamma} dt' \left\langle \exp\left\{ -\frac{2i}{\hbar} \overline{\varphi}_{\bar\gamma}[\mathbf{r}_L, \mathbf{q}_\gamma(t), \mathbf{z}_i^{\nu_2}, \mu] + \frac{2i}{\hbar} \overline{\varphi}_{\bar\gamma}[\mathbf{r}_L, \mathbf{q}_\gamma(t'), \mathbf{z}_i^{\nu_2}, \mu] \right\} \right\rangle
$$

$$
= \int_0^{T_\gamma} dt \int_0^t dt' \left\langle \exp\left\{ -\frac{2i}{\hbar} \varphi_\gamma[\mathbf{q}_\gamma(t), \mathbf{q}_\gamma(t'), \mu] \right\} \right\rangle \quad + \quad \text{c.c.}
$$

$$
= 2\tau_B^2 \left[\frac{T_\gamma}{\tau_B} + \exp\left(-\frac{T_\gamma}{\tau_B} \right) - 1 \right]. \tag{122}
$$

Altogether, we then obtain

$$
c_{ii}^{(g)} = c_{ii}^{(0)} \left| 1 - ig\tau_D \frac{\hbar}{m} \left\langle c^{(g)} \right\rangle \right|^2 = c_{ii}^{(0)} \left| 1 - \frac{ig\tau_D \frac{\hbar}{m} \left\langle c^{(0)} \right\rangle}{1 + ig\tau_D \frac{\hbar}{m} \left\langle c^{(0)} \right\rangle} \right|^2 = \frac{c_{ii}^{(0)}}{1 + \left(g\tau_D \frac{\hbar}{m} \left\langle c^{(0)} \right\rangle \right)^2} \tag{123}
$$

which together with Eq. (97) yields

$$
c_{ii}^{(g)} = \frac{c_{ii}^{(0)}}{1 + \left(gj^{\mathrm{i}} \tau_D c_{ii}^{(0)} \right)^2} = \frac{\dfrac{\tau_D}{\tau_H} \dfrac{1}{1 + \tau_D/\tau_B} \dfrac{m}{\hbar} j^{\mathrm{i}}}{1 + \left(gj^{\mathrm{i}} \tau_D \dfrac{\tau_D}{\tau_H} \dfrac{1}{1 + \tau_D/\tau_B} \right)^2} \tag{124}
$$

where j^{i} is the incident current. The probability for retro-reflection into the incident channel $n = i$ is then obtained as

$$
r_{ii} = \frac{\tau_D}{\tau_H} + \frac{\tau_D/\tau_H}{1 + \dfrac{\tau_D}{\tau_B} + \dfrac{\left(gj^{\mathrm{i}} \tau_D^2/\tau_H \right)^2}{1 + \tau_D/\tau_B}}. \tag{125}
$$

This is the main result of Section 3. It essentially states that the presence of the nonlinearity g constitutes another dephasing mechanism in addition to the magnetic field.

3.5. Alternative approach in terms of nonlinearity blocks

Inspired from Refs. [30, 31, 32], we outline, in this subsection, an alternative approach to determine the nonlinearity-induced modifications to the retro-reflection probability, which
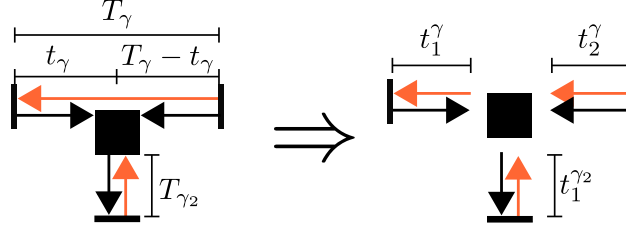
27

Figure 2: Nonlinear diagram corresponding to the calculation of $\langle \psi_i^* (\delta \psi_i^{(c)}) \rangle$. The left-hand side shows the diagram together with the durations that represent the integration variables appearing in Eq. (126). The right-hand side illustrates the variable transformation leading to Eq. (127). In effect, the diagram can be cut into individual "links" the contributions of which can be determined by separate integrals.

will become useful in the subsequent section on loop contributions. We reconsider for that purpose the calculation of $\langle \psi_i^* (\delta \psi_i^{(c)}) \rangle$ on the basis of Eq. (99), which was done using the expressions (52) and (96) for the average magnetic phase factors and the sum rules (C.13) and (C.15). If we deliberately keep the occurring integrations over trajectory durations as they appear in the sum rules [see Eq. (C.5)], we obtain as an intermediate result

$$
\begin{aligned}
\left\langle \psi_i^* \delta \psi_i^{(c)} \right\rangle &= -i \left| \frac{mS_0}{\hbar p_i^1(\mu)} \right|^4 \frac{p_i^1(\mu)}{2m\tau_H^2} \int_0^\infty dT_\gamma \int_0^{T_\gamma} dt_\gamma \int_0^\infty dT_{\gamma_2} \exp\left(-\frac{T_{\gamma_2}}{\tau_D} - \frac{T_{\gamma_2}}{\tau_B} \right) \\
&\quad \times \left[\exp\left(-\frac{T_\gamma}{\tau_D} - \frac{t_\gamma}{\tau_B} \right) + \exp\left(-\frac{T_\gamma}{\tau_D} - \frac{T_\gamma - t_\gamma}{\tau_B} \right) \right] ,
\end{aligned}
\tag{126}
$$

which transforms into

$$
\begin{aligned}
\left\langle \psi_i^* \delta \psi_i^{(c)} \right\rangle &= -i \left| \frac{mS_0}{\hbar p_i^1(\mu)} \right|^4 \frac{p_i^1(\mu)}{2m\tau_H^2} \int_0^\infty dt_1^\gamma \int_0^\infty dt_2^\gamma \int_0^\infty dt_1^{\gamma_2} \exp\left(-\frac{t_1^{\gamma_2}}{\tau_D} - \frac{t_1^{\gamma_2}}{\tau_B} \right) \\
&\quad \times \left[\exp\left(-\frac{t_1^\gamma + t_2^\gamma}{\tau_D} - \frac{t_1^\gamma}{\tau_B} \right) + \exp\left(-\frac{t_1^\gamma + t_2^\gamma}{\tau_D} - \frac{t_2^\gamma}{\tau_B} \right) \right]
\end{aligned}
\tag{127}
$$

after applying the variable transformation $t_1^\gamma \equiv t_\gamma$, $t_2^\gamma \equiv T_\gamma - t_\gamma$, $t_1^{\gamma_2} \equiv T_{\gamma_2}$ that is motivated from Ref. [51]. Figure 2 illustrates this variable transformation in the corresponding nonlinear diagram. In effect, the transformation cuts the diagram into separate pieces of trajectories which we shall, as done in Ref. [51], refer to as "links" and which are connected with each other at the "nonlinearity block" ■. Each link gives rise to a separate integration yielding either τ_D for ladder-type links ⟹ or $\tau_D/(1+\tau_D/\tau_B)$ for crossed-type links ⟸. Applying this rule to the diagram under consideration, we obtain again the expression (102) for $\langle \psi_i^* (\delta \psi_i^{(c)}) \rangle$.

This reasoning can be generalized to more complicated diagrams involving more than one nonlinearity block. Under consideration of the sum rules (C.13) – (C.15) and of the combinatorial prefactors 2 arising in front of each nonlinearity block [see Eq. 82], we can state the following rules:

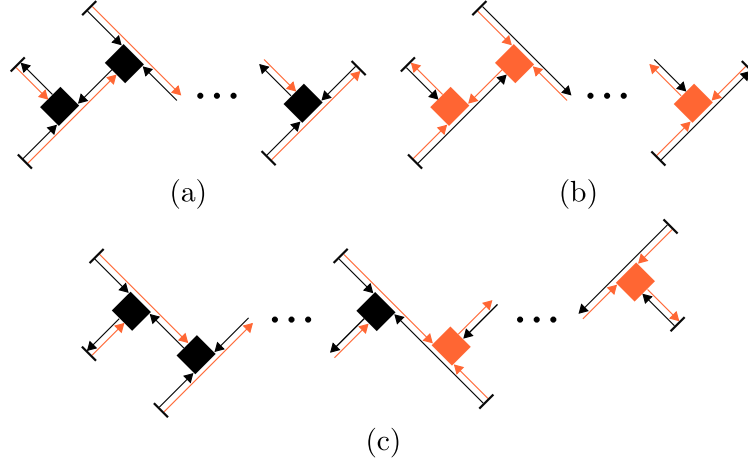(1) each source ▮ contributes a factor $\hbar/p_i^1(\mu)$;

Figure 3: Relevant diagrams for the calculation of the nonlinear contribution to the backscattering probability. Diagrams (a), (b), and (c) respectively correspond to the second, the third, and the fourth term on the right-hand side of Eq. (104) as well as to the second, the third, and the fourth line of Eq. (128).

(2) each arrow emanating from a source $\longmapsto$ contributes a factor S_0 (and each conjugate arrow $\longmapsto$ a factor S_0^*);

(3) each trajectory, scattering from lead to lead or ending at a nonlinearity event within the billiard, contributes a factor $m^2/(\hbar^4 \tau_H)$;

(4) each nonlinearity event $\blacksquare$ in the scattering wavefunction contributes a factor $-ig\hbar/m$ (and each nonlinearity event $\blacksquare$ in the conjugate wavefunction contributes a factor $ig\hbar/m$);

(5) each ladder-type link $\Longrightarrow$ contributes a factor τ_D;

(6) each crossed-type link $\Longleftrightarrow$ contributes a factor $(1/\tau_D + 1/\tau_B)^{-1}$.

Using these rules, we can re-calculate the crossed contribution $c_{ii}^{(g)}$ to the retro-reflection intensity. In contrast to Section 3.4, we do not explicitly need to introduce the nonlinear crossed density $C^{(g)}(\mathbf{r})$ as done in Eq. (107). Instead, we directly sum over all possible combinations of crossed diagrams as they are depicted in Fig. 3. Together with the contribution
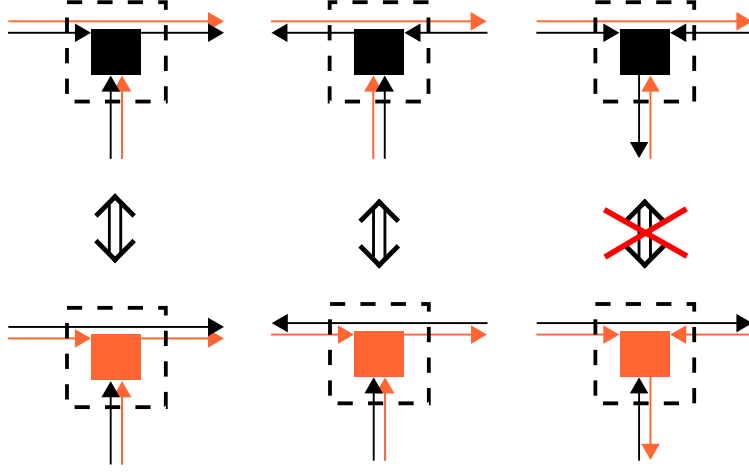
Figure 4: Basic building blocks with which all possible diagrams can be constructed. As shown in the left and central columns, blocks with ladder-type input can be incorporated in both the ψ and the ψ^* branch for the same orientation and pairing of the trajectories outside the block region (depicted by the dashed square). This is not the case for blocks with crossed-type input shown in the right column, due to the mismatch of trajectories entering and leaving the block. Consequently, the contributions resulting from those blocks do not cancel each other, in contrast to the blocks with ladder-type input, but give rise to a finite modification of the reflection and transmission probabilities in the presence of the nonlinearity.

of the diagram $\longmapsto$, this yields

$$
\begin{aligned}
\langle|\psi_i|^2\rangle_{\mathrm{c}} &= |S_0|^2 \left(\frac{\hbar}{p_i^{\mathrm{l}}(\mu)}\right)^2 \frac{m^2}{\hbar^4 \tau_H} \left(\frac{1}{\tau_D} + \frac{1}{\tau_B}\right)^{-1} \\
&\quad + \sum_{k=1}^{\infty} \left(-i\frac{\hbar}{m}g\tau_D\right)^k \left[|S_0|^2 \frac{m^2}{\hbar^4 \tau_H}\left(\frac{1}{\tau_D}+\frac{1}{\tau_B}\right)^{-1}\right]^{k+1} \left(\frac{\hbar}{p_i^{\mathrm{l}}(\mu)}\right)^{k+2} \\
&\quad + \sum_{k=1}^{\infty} \left(i\frac{\hbar}{m}g\tau_D\right)^k \left[|S_0|^2 \frac{m^2}{\hbar^4 \tau_H}\left(\frac{1}{\tau_D}+\frac{1}{\tau_B}\right)^{-1}\right]^{k+1} \left(\frac{\hbar}{p_i^{\mathrm{l}}(\mu)}\right)^{k+2} \\
&\quad + \sum_{k,k'=1}^{\infty} i^{k-k'} \left(\frac{\hbar}{m}g\tau_D\right)^{k+k'} \left[|S_0|^2 \frac{m^2}{\hbar^4 \tau_H}\left(\frac{1}{\tau_D}+\frac{1}{\tau_B}\right)^{-1}\right]^{k+k'+1} \left(\frac{\hbar}{p_i^{\mathrm{l}}(\mu)}\right)^{k+k'+2} \\
&= \frac{\left|\frac{mS_0}{\hbar p_i^{\mathrm{l}}(\mu)}\right|^2 \left(\frac{\tau_H}{\tau_D}+\frac{\tau_H}{\tau_B}\right)^{-1}}{1 + \left[g\tau_D \frac{m|S_0|^2}{\hbar^2 p_i^{\mathrm{l}}(\mu)} \left(\frac{\tau_H}{\tau_D}+\frac{\tau_H}{\tau_B}\right)^{-1}\right]^2}
\end{aligned}
\tag{128}
$$

which is perfectly equivalent to Eq. (124).

The approach on the basis of nonlinearity blocks also provides an alternative understanding why blocks with ladder-type input [i.e. where a ladder pairing is employed along
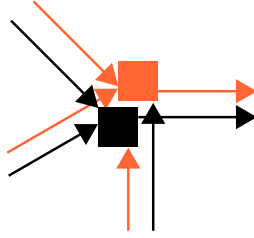
Figure 5: Example for a nonlinear diagram that is not accounted for in the present diagrammatic theory. This diagram requires the presence of two nonlinearity blocks at the same spatial location and is therefore not expected to be of relevance for weak nonlinearity strengths.

the trajectory that ends at the nonlinearity event, corresponding to the cases (68) and (69) in Section 3.2, and displayed in the left and central columns of Fig. 4], do not affect the mean values of densities and currents of the propagating condensate. We remark for this purpose that the individual factor provided by each nonlinearity block is purely *imaginary* (as stated above by rule 4), with a negative imaginary part for blocks ■ that are incorporated within ψ and with a positive imaginary part for blocks ■ within ψ^*. Two diagrams that are almost identical except for the incorporation of one single nonlinearity block, which is placed within ψ in one of the diagrams and within ψ^* in the other diagram, will therefore cancel each other in summations over all possible diagrams, as they contribute with equal amplitudes and opposite signs. As illustrated in Fig. 4, this is the case for each diagram containing a block with ladder-type input, which has a counterpart in which this block is incorporated in the opposite manner. Such diagrams do therefore not need to be considered for the calculation of mean densities or currents of the propagating condensate. Blocks with crossed-type input, on the other hand, can, in general, not be paired with cancelling counterparts, which is shown in the right column of Fig. 4.

Let us finally point out that the validity of the present diagrammatic theory is still limited to weak nonlinearity strengths, despite the above summations to infinite order in g. This is illustrated in Fig. 5 which shows an example for a diagram of second order in g that is not accounted for in our diagrammatic theory. It represents diffraction of the matter wave by short-ranged spatial fluctuations of the nonlinear term $g\frac{\hbar^2}{2m}|\Psi(\mathbf{r}, t)|^2$ in the Gross-Pitaevskii equation (1). As it requires the presence of two nonlinearity events within a region of the order of one wavelength, its contribution is strongly suppressed in the semiclassical regime as compared to other diagrams of second order in g in which the nonlinearity blocks are spatially uncorrelated. We do expect, however, that diagrams of the type shown in Fig. 5 will become relevant for large nonlinearity strengths, possibly in the regime in which the scattering process destabilizes and develops turbulent-like flow.

4. Loop corrections

In the previous section, we developed a semiclassical description of weak localization in the presence of a weak atom-atom interaction restricting ourselves to the diagonal approximation. This theory will fail to describe the occurring phenomena quantitatively, as it
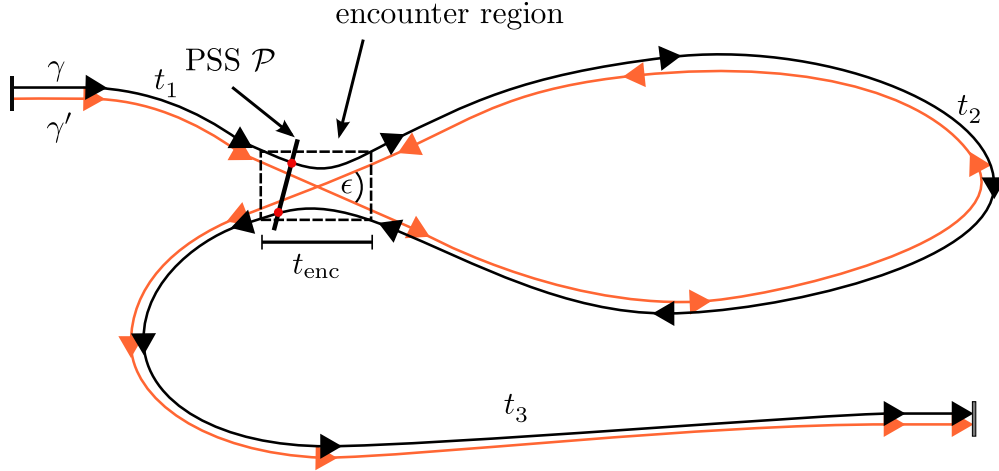
Figure 6: Sketch of a trajectory γ which experiences a self encounter and its corresponding partner trajectory γ'. In configuration space, which is depicted here, one trajectory crosses itself with a small crossing angle ϵ whereas the other one avoids the crossing. Also shown is the position of a possible Poincaré surface of section $\mathcal{P}$ used to determine the action difference. We note here that this sketch is widely overestimating the crossing angle ϵ and underestimating the trajectory lengths before and after the encounter region.

violates current conservation both in the absence and in the presence of the nonlinearity. The reason for this failure lies in the use of the diagonal approximation, i.e. we only used identical or time-reversed trajectories when our methods demanded correlated trajectory pairs. However, as originally shown in Refs. [52, 53] for the spectral form factor and in Ref. [28] for the Landauer conductance in the transport of electrons through two-dimensional uniformly hyperbolic systems with time-reversal symmetry, there is, besides the above mentioned one, a second type of correlated trajectory pairs giving significant contributions to the reflection and transmission probabilities, the so-called "loops" or "Sieber-Richter pairs". These are pairs of trajectories with nearly identical initial and final conditions; as illustrated in Fig. 6, one of the two trajectories undergoes a self-crossing with a small crossing angle ϵ whereas the other one avoids that crossing. More generally speaking, as originally worked out in Refs. [54, 55] for the spectral form factor, these trajectories exhibit an encounter in phase space with their time-reversed counterparts, which allows for the existence of a partner trajectory that switches from the original trajectory to the time-reversed counterpart. We shall adopt this more general phase space picture to derive the corrections to weak localization in the linear and in the nonlinear case.

4.1. Loop corrections in the linear case

Our calculation of the contributions to weak localization in the case $g = 0$ mainly follows Refs. [56, 51]. We shall restrict ourselves here and in the following to the case of at most one Sieber-Richter pair per diagram, as the presence of more such pairs would only result in higher-order contributions in $\tau_D/\tau_H = 1/(N_c + \tilde{N}_c)$. For the sake of definiteness, we shall consider the problem of determining the transmission probability $t_{\tilde{n}i} \equiv j_{\tilde{n}}/j^{\mathrm{i}}$ that is

associated with the scattering process from the incident channel i in the left lead to the final channel $\tilde{n}$ in the right lead. Our purpose is therefore to calculate

$$\left\langle |\psi_{\tilde{n}}^{(0)}|^2 \right\rangle = \left| S_0 \frac{\pi \hbar}{\sqrt{W\tilde{W}}} \right|^2 \sum_{\nu_1, \nu_1' = \pm 1} \sum_{\nu_2, \nu_2' = \pm 1} \nu_1 \nu_1' \nu_2 \nu_2' \left\langle \widetilde{\overline{G}} \left(\mathbf{z}_{\tilde{n}}^{\nu_1}, \mathbf{z}_i^{\nu_1'}, \mu \right) \widetilde{\overline{G}}^* \left(\mathbf{z}_{\tilde{n}}^{\nu_2}, \mathbf{z}_i^{\nu_2'}, \mu \right) \right\rangle . \quad (129)$$

As this quantity involves a product of two Green functions, we are concerned with sums over pairs of classical trajectories γ, γ' here. In the context of the diagonal approximation, we already evaluated in Section 3 the most dominant contribution to this transmission probability, for which γ' is identical to γ.

The next group of systematically correlated trajectories consists of pairs γ, γ' that exhibit, as sketched in Fig. 6, a self-encounter in phase space [52, 28, 51]. Their action difference can be determined by defining a Poincaré surface of section $\mathcal{P}$ within the encounter region, which is oriented perpendicular to γ on the first passage of this trajectory through it, i.e., which is pierced by the first stretch of γ at its origin. Linearizing the classical dynamics in the vicinity of this trajectory, we can define two basis vectors e_s and e_u within the two-dimensional surface of section $\mathcal{P}$ that are respectively oriented along the stable and unstable manifold of γ. The action difference between γ and γ' is then evaluated as [54, 55]

$$\Delta S_{\gamma,\gamma'} \equiv \widetilde{\overline{S}}_\gamma - \widetilde{\overline{S}}_{\gamma'} = su \quad (130)$$

where s and u denote the coordinates with respect to the basis vectors e_s and e_u, respectively, at which the trajectory γ pierces through $\mathcal{P}$ for the second time. Obviously, $\Delta S_{\gamma,\gamma'}$ can be sufficiently small, i.e. of the order of $\hbar$, if, as depicted in Fig. 6, one of the two trajectories exhibits a self-crossing in configuration space with a very small crossing angle ϵ [52, 28]. The partner trajectory, whose existence and uniqueness is granted by the chaoticity of the classical dynamics, will then avoid that self-crossing and follow the loop in between the two piercings through $\mathcal{P}$ in the opposite direction.

In order to evaluate the contributions of such Sieber-Richter pairs to Eq. (129), we need to determine the probability of a trajectory γ to exhibit a near-encounter in phase space. Due to ergodicity, the probability density for the trajectory γ to pierce again through the Poincaré surface of section in the opposite direction at given coordinates s and u and after a given propagation time $\tilde{t}_2$ after the first piercing is given by the Liouville measure $\delta[\mu - H_0(\mathbf{p}, \mathbf{q})]/\Sigma(\mu)$ with $(\mathbf{p}, \mathbf{q})$ the coordinates of the second piercing in the full phase space and $\Sigma(\mu) \equiv \int d^2q' \int d^2p' \delta[\mu - H_0(\mathbf{p}', \mathbf{q}')]$ the phase-space volume of the energy shell. If we want to calculate the probability density for a trajectory γ with a given total propagation time T to have a partner trajectory γ' with a given action difference $\Delta S_{\gamma,\gamma'} \equiv \Delta S$, we are tempted to integrate this Liouville measure over all "intermediate" propagation times $\tilde{t}_2$ between the first and the second intersection through the Poincaré surface of section $\mathcal{P}$, over all "initial" propagation times $\tilde{t}_1$ from the incident channel to the first intersection through $\mathcal{P}$, over all "final" propagation times $\tilde{t}_3$ from the second intersection through $\mathcal{P}$ to the outgoing channel, as well as over all possible phase-space coordinates s, u that γ exhibits within $\mathcal{P}$ at its second piercing, with the requirements that $su = \Delta S$ and $\tilde{t}_1 + \tilde{t}_2 + \tilde{t}_3 = T$. This naïve

integration would, however, lead to *multiple countings* of such trajectory pairs. Indeed, the placement of the Poincaré surface of section $\mathcal{P}$ is not unique, but can be shifted along the first stretch of the trajectory γ. This generally will lead to different coordinates s, u of the second stretch of γ when passing through $\mathcal{P}$, but the product su of these coordinates will not change, provided the second piercing point of γ is also in a sufficiently close neigbourhood of the origin of $\mathcal{P}$ such that the linearization of the classical dynamics around γ is still valid (see also the calculations in Appendix Appendix E).

The contribution of an individual Sieber-Richter pair with an action difference ΔS would, when performing the above-mentioned integration, therefore effectively be overweighted by a factor $t_{\text{enc}} \equiv t_{\text{enc}}(\Delta S)$ that corresponds to the typical "duration" of the encounter, i.e., the typical propagation time within which one of the trajectories "sees" the other one within a distance that is within the linearization region of its transverse dynamics. Defining by λ the Lyapunov exponent of the ergodic system [57], and introducing c as the maximal distance along the stable and unstable manifolds e_s, e_u for the linearization of the transverse dynamics within the Poincaré surface of section $\mathcal{P}$ to be valid (i.e., we require that $-c < s, u < c$; the precise value of c, which is related to the Ehrenfest time of the system as pointed out in Appendix Appendix E.1, will not be of relevance in the end), we can define [56, 51]

$$t_{\text{enc}}(su) = \frac{1}{\lambda} \ln\left(\frac{c^2}{|su|}\right) .$$
(131)

This duration $t_{\text{enc}}(su)$ reflects the fact that some minimal time is needed for the two nearby trajectory stretches to part from each other, in order to form the loop on one end and to exit toward different leads on the other end of the encounter region.

In view of these considerations, we define (see also Ref. [51])

$$w(\Delta S, t_2; T) = \int\limits_0^\infty \int\limits_0^\infty dt_1 dt_3 \int\limits_{-c}^c \int\limits_{-c}^c ds\, du \frac{\delta(su - \Delta S)}{\Sigma(\mu)t_{\text{enc}}(su)} \delta[t_1 + t_2 + t_3 + 2t_{\text{enc}}(su) - T]$$
(132)

as the probability density for a trajectory γ with the total propagation time T to have a partner trajectory γ' with an action difference ΔS and a loop duration t_2. This loop duration t_2 as well as the initial and final propagation times t_1 and t_3 that appear in the integrations in Eq. (132) are, as illustrated in Fig. 6, defined not with respect to the particular placement of the Poincaré surface of section, but with respect to the location of the encounter region along the trajectory. Using $\overline{\widetilde{A}}_\gamma \simeq \overline{\widetilde{A}}_{\gamma'}$ and $\overline{\widetilde{\mu}}_\gamma \simeq \overline{\widetilde{\mu}}_{\gamma'}$ for the trajectory pair γ, γ', the loop contributions to $\langle |\psi_{\tilde{n}}^{(0)}|^2 \rangle$ are calculated as

$$\left\langle \left|\psi_{\tilde{n}}^{(0)}\right|^2 \right\rangle_{\text{loop}} = \frac{|S_0|^2 (\pi\hbar)^2}{W\tilde{W}} \sum_{\nu,\nu'=\pm 1} \int_{-\infty}^\infty d(\Delta S) \int_0^\infty dt_2 \sum_\gamma \left\langle \left|\widetilde{A}_\gamma\left(\mathbf{z}_{\tilde{n}}^\nu, \mathbf{z}_i^{\nu'}, \mu\right)\right|^2 \right\rangle$$

$$\times w(\Delta S, t_2; T_\gamma) \exp\left(\frac{i}{\hbar}\Delta S\right) \exp\left(-\frac{t_2}{\tau_B}\right),$$
(133)

34

where the dephasing factor $\exp(-t_2/\tau_B)$ originates from $\varphi_\gamma\left[\mathbf{r}_\gamma(t_1 + t_{\mathrm{enc}} + t_2), \mathbf{r}_\gamma(t_1 + t_{\mathrm{enc}}), \mu\right]$, the flux integral along the loop according to Eq. (52). We neglect here the contribution of the flux inside the encounter region, which will be discussed in the next subsection.

When applying the sum rule (C.15), we have to use a modified survival probability $\exp\left[-(T - t_{\mathrm{enc}})/\tau_d\right]$ in Eq. (C.6). Indeed, if the first stretch of the encounter lies within the billiard, the second one does so as well, thus the trajectory does not risk to escape during its second passing through the encounter region. The relevant time for the survival probability has therefore to be reduced by the duration t_{enc} of this second stretch. We then obtain

$$
\begin{aligned}
\left\langle \left|\psi_{\tilde{n}}^{(0)}\right|^2 \right\rangle_{\mathrm{loop}} &= \left|\frac{mS_0}{\hbar}\right|^2 \frac{1}{\tau_H p_{\tilde{n}}^{\mathrm{l}}(\mu) p_i^{\mathrm{l}}(\mu)} \int_0^\infty dt_1 \int_0^\infty dt_2 \int_0^\infty dt_3 \exp\left(-\frac{t_1 + t_2 + t_3}{\tau_D} - \frac{t_2}{\tau_B}\right) \\
&\quad \times \int_{-c}^c ds \int_{-c}^c du \frac{1}{\Sigma(\mu)t_{\mathrm{enc}}(su)} \exp\left(\frac{i}{\hbar}su\right) \exp\left(-\frac{t_{\mathrm{enc}}(su)}{\tau_D}\right) \\
&= -\frac{m}{p_{\tilde{n}}^{\mathrm{l}}(\mu)} j^{\mathrm{i}} \left(\frac{\tau_D}{\tau_H}\right)^2 \frac{1}{1 + \tau_D/\tau_B} \,,
\end{aligned}
\tag{134}
$$

as shown in Appendix Appendix E.1. In a similar way as for nonlinearity blocks (see the discussion in Section 3.5), the encounter region cuts the diagram into three "links" contributing either τ_D or $\tau_D/(1 + \tau_D/\tau_B)$.

The same derivation can be applied in order to calculate the loop contributions to the reflection probability into channel n, leading to exactly the same result as in Eq. (134). We therefore obtain

$$
\delta\left(t_{\tilde{n}i}^{(0)}\right)^{\mathrm{loop}} = \delta\left(r_{ni}^{(0)}\right)^{\mathrm{loop}} = -\left(\frac{\tau_D}{\tau_H}\right)^2 \frac{1}{1 + \tau_D/\tau_B}
\tag{135}
$$

as loop contributions to the reflection and transmission probabilities $r_{ni}^{(0)}$ and $t_{\tilde{n}i}^{(0)}$ in the absence of interaction. These corrections do indeed restore current conservation in leading semiclassical order. Combining all ladder, crossed, and loop contributions that are evaluated in Eqs. (42), (57), and (135), respectively, we obtain with Eq. (44)

$$
r_{ii}^{(0)} = \frac{\tau_D}{\tau_H}\left(1 + \frac{\tau_H - \tau_D}{\tau_H}\frac{1}{1 + \tau_D/\tau_B}\right) = \frac{1}{N_c + \tilde{N}_c}\left(1 + \frac{N_c + \tilde{N}_c - 1}{N_c + \tilde{N}_c}\frac{1}{1 + B^2/B_0^2}\right)
\tag{136}
$$

for the probability of retro-reflection into the incident channel $n = i$, as well as

$$
r_{ni}^{(0)} = t_{\tilde{n}i}^{(0)} = \frac{\tau_D}{\tau_H}\left(1 - \frac{\tau_D}{\tau_H}\frac{1}{1 + \tau_D/\tau_B}\right) = \frac{1}{N_c + \tilde{N}_c}\left(1 - \frac{1}{N_c + \tilde{N}_c}\frac{1}{1 + B^2/B_0^2}\right)
\tag{137}
$$

for the probabilities of reflection into a different channel $n \neq i$ and of transmission into channel $\tilde{n}$. This yields the total reflection and transmission probabilities

$$
\begin{aligned}
R^{(0)} &= \frac{N_c}{N_c + \tilde{N}_c} + \frac{\tilde{N}_c}{(N_c + \tilde{N}_c)^2}\frac{1}{1 + B^2/B_0^2} \,, \tag{138} \\
T^{(0)} &= \frac{\tilde{N}_c}{N_c + \tilde{N}_c} - \frac{\tilde{N}_c}{(N_c + \tilde{N}_c)^2}\frac{1}{1 + B^2/B_0^2} \,, \tag{139}
\end{aligned}
$$

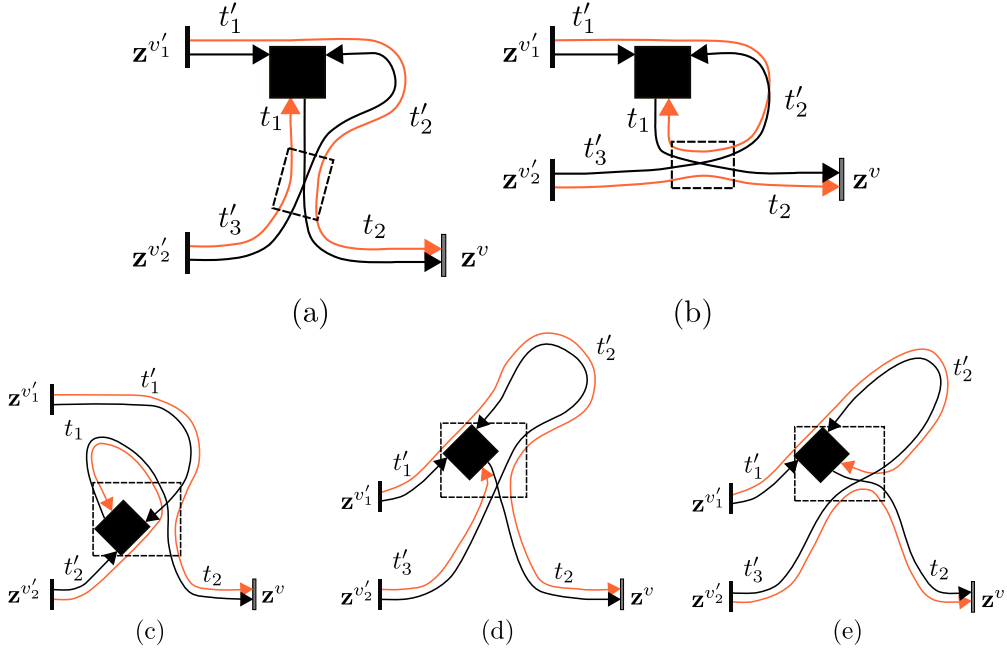in the linear case $g = 0$, which obviously satify $R^{(0)} + T^{(0)} = 1$.

Figure 7: Diagrammatic representation of the nonlinear loop contributions that arise in first order in the nonlinearity strength g. These diagrams involve encounters between different trajectories rather than a self-encounter of one trajectory. The upper and lower rows show, respectively, the two diagrams (a) and (b) in which the nonlinearity block is located outside the encounter region, as well as the three possibilities (c), (d), and (e) for the nonlinearity event to enter the encounter region. The diagram (c), in which the nonlinearity block moves along a stretch through the whole encounter region, corresponds to the transition from diagram (a) to diagram (b). Diagrams (d) and (e), on the other hand, are obtained from diagrams (a) and (b), respectively, by pushing, in these latter two diagrams, the nonlinearity block along the trajectory that starts at the block into the encounter region.

4.2. Contributions of first order in the nonlinearity

In the case of non-vanishing interaction between the atoms, the determination of the loop contributions to reflection and transmission probabilities becomes more involved due to richer possibilities for associating correlated trajectories that exhibit small action differences. Loop contributions arise not only from self-encounters of single trajectories, but also from encounters of different trajectories in phase space. This is illustrated in Fig. 7 which shows the nonlinear diagrams that contribute to loop corrections of the reflection and transmission probabilities in linear order in g. As it is quite instructive, we begin our analysis of loop corrections in the nonlinear case with the calculation of the contributions of these diagrams. We shall first focus on diagrams (a) and (b) of Fig. 7 in which the nonlinearity event can only move along parts of trajectories that are outside the encounter region.

As a starting point, we have to define the probability density $\tilde{w}$ for having a pair of trajectories γ and γ' that exhibit a near-encounter in phase space. This near-encounter results in the existence of an additional pair of partner trajectories $\tilde{\gamma}$, $\tilde{\gamma}'$. In configuration space, the trajectories cross each other under a small angle in one of these two pairs, (γ, γ')
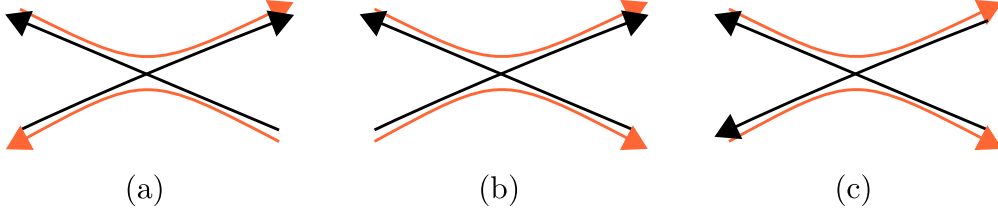
Figure 8: Three different constellations for the stretches involved in an encounter region. In the case of constellation (a), which arises also in the linear case discussed in Section 4.1, the encounter region itself does not provide a significant contribution to the dephasing in the presence of an external magnetic field, since the flux integrals in the phases associated with the individual stretches cancel each other. This is different for the constellations (b) and (c) in which twice (b) and four times (c) the flux integral from a stretch of duration t_{enc} remains, yielding the phase factors $\exp(-t_{\mathrm{enc}}/\tau_B)$ for constellation (b) and $\exp(-2t_{\mathrm{enc}}/\tau_B)$ for constellation (c).

or $(\tilde{\gamma}, \tilde{\gamma}')$, whereas the other pair avoids this crossing.

The probability density $\tilde{w}$ is specified for a given action difference ΔS between the trajectories γ, γ' and the pair of partner trajectories $\tilde{\gamma}, \tilde{\gamma}'$, as well as for given partial propagation times t, t' of the trajectories γ and γ', respectively, before (in the case of trajectory γ) or after (in the case of trajectory γ') the encounter region, which may become relevant for the evaluation of magnetic dephasing. It furthermore depends parametrically on the total propagation times T and T' of the two trajectories γ, γ' as well as on the orientations of the individual trajectory stretches within the encounter region, as these orientations might give rise to additional contributions to the magnetic dephasing. Figure 8 displays three different possibilities for orienting the trajectory stretches within the encounter region. While the encounter region in constellation (a) does not contribute to the dephasing in the presence of a magnetic field, the constellations (b) and (c) contribute with phase factors $\exp(-t_{\mathrm{enc}}/\tau_B)$ and $\exp(-2t_{\mathrm{enc}}/\tau_B)$, respectively, as there are one (b) and two (c) trajectory stretches ⟶ of the linear Green function that are not balanced by the complex conjugate counterparts ⟶ .

Denoting by $n \in \{0, 1, 2\}$ the number of imbalanced pairs of stretches within the encounter region, we define

$$
\begin{aligned}
\tilde{w}(\Delta S, t, t'; T, T', n) &= \int_0^\infty \int_0^\infty d\tilde{t} d\tilde{t}' \int_{-c}^c \int_{-c}^c ds\, du \frac{\delta(\Delta S - su)}{\Sigma(\mu) t_{\mathrm{enc}}(su)} \exp\left[-n \frac{t_{\mathrm{enc}}(su)}{\tau_B} \right] \\
&\quad \times \delta\left(t + \tilde{t} + t_{\mathrm{enc}}(su) - T \right) \delta\left(t' + \tilde{t}' + t_{\mathrm{enc}}(su) - T' \right)
\end{aligned}
\tag{140}
$$

as the density of trajectory pairs γ, γ' that come close to each other in phase space and thus have partner trajectories with a combined action difference ΔS. In this expression, the integration variables $\tilde{t}$ and $\tilde{t}'$ correspond to the propagation times of the final and initial parts of the trajectories γ and γ', respectively, after leaving ($\tilde{t}$) and before entering ($\tilde{t}'$) the encounter region. We have $n = 0 \equiv n_a$ for diagram (a) and $n = 1 \equiv n_b$ for diagram (b) in Fig. 7.

Calculating now the contributions of the diagrams shown in the upper row of Fig. 7 (which are multiplied by a combinatorial factor 2 as there are two possibilities to construct these diagrams), we obtain

$$
\left\langle \psi_{\tilde{n}}^{(0)*} \left(\delta \psi_{\tilde{n}}^{(1)} \right) \right\rangle_{\text{loop, (a/b)}} = 2 \frac{\hbar^2}{2m} \frac{|S_0|^4 (\pi\hbar)^3}{\tilde{W} W^2} \left\langle \sum_{\nu_1', \nu_2', \nu=\pm 1} \widetilde{G}^* \left(\mathbf{z}_{\tilde{n}}^\nu, \mathbf{z}_i^{\nu_1'}, \mu \right) \right.
$$

$$
\times \left. \int_\Omega d^2 r' \widetilde{G} \left(\mathbf{z}_{\tilde{n}}^\nu, \mathbf{r}', \mu \right) \overline{G} \left(\mathbf{r}', \mathbf{z}_i^{\nu_1'}, \mu \right) \overline{G} \left(\mathbf{r}', \mathbf{z}_i^{\nu_2'}, \mu \right) \overline{G}^* \left(\mathbf{r}', \mathbf{z}_i^{\nu_2'}, \mu \right) \right\rangle_{\text{loop, (a/b)}}
$$

$$
= 2 \frac{\hbar^2}{2m} \frac{|S_0|^4 (\pi\hbar)^3}{\tilde{W} W^2} \int_{-\infty}^\infty d(\Delta S) \int_0^\infty dt_1 \int_0^\infty dt_2' \sum_{\nu_1', \nu_2', \nu=\pm 1} \sum_{\gamma'} \left\langle \left| \overline{\widetilde{A}}_{\gamma'} \left(\mathbf{z}_i^{\nu_2'}, \mathbf{z}_i^{\nu_1'}, \mu \right) \right|^2 \right\rangle
$$

$$
\times \left(-\frac{i}{\hbar} \right) \int_0^\infty dt_1' \sum_\gamma \left\langle \left| \widetilde{A}_\gamma [\mathbf{z}_{\tilde{n}}^\nu, \mathbf{r}_{\gamma'}(t_1'), \mu] \right|^2 \right\rangle
$$

$$
\times \tilde{w} \left(\Delta S, t_1, t_2'; T_\gamma, T_{\gamma'} - t_1', n_{a/b} \right) \exp \left(\frac{i}{\hbar} \Delta S \right) \exp \left(-\frac{t_1 + t_2'}{\tau_B} \right)
$$

$$
= -i \frac{m}{p_{\tilde{n}}^l(\mu)} \left(\frac{m|S_0|^2}{\hbar^2 p_i^l(\mu)} \right)^2 \frac{1}{\tau_H^2} \int_0^\infty dt_1' \int_0^\infty dt_2' \int_0^\infty dt_3' \int_0^\infty dt_1 \int_0^\infty dt_2
$$

$$
\times \exp \left(-\frac{t_1' + t_2' + t_3' + t_1 + t_2}{\tau_D} - \frac{t_1 + t_2'}{\tau_B} \right)
$$

$$
\times \int_{-c}^c ds \int_{-c}^c du \frac{1}{\Sigma(\mu) t_{\text{enc}}(su)} \exp \left(\frac{i}{\hbar} su \right) \exp \left[-\frac{t_{\text{enc}}(su)}{\tau_D} - n_{a/b} \frac{t_{\text{enc}}(su)}{\tau_B} \right], \qquad (141)
$$

where we applied the sum rules (C.14, C.15) to convert the sums over classical trajectories γ, γ' into integrations over trajectory durations T_γ, $T_{\gamma'}$, taking into account that we have to use a reduced effective time $T_\gamma + T_{\gamma'} - t_{\text{enc}}$ for the classical survival probability. Gauge invariance of the result is ensured by the fact that the encounter region closes the overall flux integral. The integration over s and u is calculated in Appendix Appendix E.1 and yields $-1/(\tau_D \tau_H)$ for $n = n_a = 0$ as well as $-(1 + \tau_D/\tau_B)/(\tau_D \tau_H)$ for $n = n_b = 1$. We therefore obtain

$$
\left\langle \psi_{\tilde{n}}^{(0)*} \left(\delta \psi_{\tilde{n}}^{(1)} \right) \right\rangle_{\text{loop, (a)}} = i \frac{m}{p_{\tilde{n}}^l(\mu)} (j^i)^2 \left(\frac{\tau_D}{\tau_H} \right)^3 \tau_D \left(\frac{1}{1 + \tau_D/\tau_B} \right)^2, \qquad (142)
$$

$$
\left\langle \psi_{\tilde{n}}^{(0)*} \left(\delta \psi_{\tilde{n}}^{(1)} \right) \right\rangle_{\text{loop, (b)}} = i \frac{m}{p_{\tilde{n}}^l(\mu)} (j^i)^2 \left(\frac{\tau_D}{\tau_H} \right)^3 \tau_D \left(\frac{1}{1 + \tau_D/\tau_B} \right) \qquad (143)
$$

for the cases where the nonlinearity block is located outside the encounter region.

As shown in the lower row of Fig. 7, there are two qualitatively different possibilities for the nonlinearity event to enter the encounter region. In the first scenario, depicted in Fig. 7(c), the nonlinearity event moves along a trajectory that provides a stretch within the encounter region. This scenario corresponds to the transition from diagram (a) to diagram

(b). Its contribution is calculated as

$$
\left\langle \psi_{\tilde{n}}^{(0)*} \left(\delta\psi_{\tilde{n}}^{(1)} \right) \right\rangle_{\text{loop, (c)}} =
$$

$$
= 2\frac{\hbar^2}{2m} \frac{|S_0|^4 (\pi\hbar)^3}{\tilde{W}W^2} \int_{-\infty}^{\infty} d(\Delta S) \int_0^\infty dt_1 \int_0^\infty dt_1' \sum_{\nu_1',\nu_2',\nu=\pm 1} \sum_{\gamma'} \left\langle \left| \widetilde{\overline{A}}_{\gamma'} \left(\mathbf{z}_i^{\nu_2'}, \mathbf{z}_i^{\nu_1'}, \mu \right) \right|^2 \right\rangle
$$

$$
\times \left(-\frac{i}{\hbar} \right) \int_0^{t_{\text{enc}}(\Delta S)} dt' \sum_{\gamma} \left\langle \left| \widetilde{A}_{\gamma} \left[\mathbf{z}_{\tilde{n}}^\nu, \mathbf{r}_{\gamma'}(t_1'+t'), \mu \right] \right|^2 \right\rangle
$$

$$
\times \tilde{w}\left(\Delta S, t_1, t_1'; T_\gamma, T_{\gamma'}, 0\right) \exp\left(\frac{i}{\hbar}\Delta S\right) \exp\left(-\frac{t_1+t'}{\tau_B}\right)
$$

$$
= -i\frac{m}{p_{\tilde{n}}^{\text{l}}(\mu)} \left(j^{\text{i}}\right)^2 \frac{1}{\tau_H^2} \int_0^\infty dt_1' \int_0^\infty dt_2' \int_0^\infty dt_1 \int_0^\infty dt_2
$$

$$
\times \exp\left(-\frac{t_1'+t_2'+t_1+t_2}{\tau_D} - \frac{t_1+t_2'}{\tau_B} \right)
$$

$$
\times \int_{-c}^c ds \int_{-c}^c du \frac{1}{\Sigma(\mu)t_{\text{enc}}(su)} \exp\left(\frac{i}{\hbar}\right) \exp\left(-\frac{t_{\text{enc}}(su)}{\tau_D}\right) \int_0^{t_{\text{enc}}(su)} dt' \exp\left(-\frac{t'}{\tau_B}\right)
$$

$$
= -i\frac{m}{p_{\tilde{n}}^{\text{l}}(\mu)} \left(j^{\text{i}}\right)^2 \left(\frac{\tau_D}{\tau_H}\right)^3 \tau_D \left(\frac{1}{1+\tau_D/\tau_B}\right) = -\left\langle \psi_{\tilde{n}}^{(0)*} \left(\delta\psi_{\tilde{n}}^{(1)} \right) \right\rangle_{\text{loop, (b)}} \tag{144}
$$

[see Fig. 7(c) for the signification of t_1, t_2, t_1', t_2'], where the integrations over s, u and over the propagation time t' within the encounter region (whose gauge field dependence is taken into account in the integration) yield, as shown in Appendix Appendix E.2, $1/\tau_H$.

In the other scenario, depicted in Fig. 7(d) and (e), a trajectory pair leaving the encounter and ending at a nonlinearity event becomes arbitrarily small until finally the nonlinearity event enters the encounter region but does not traverse it. This case requires a modification of the probability density of suitable partner trajectories as some stretches do not leave the encounter region any more but terminate at a certain point within it. Following Refs. [58, 59, 60], we define a reduced encounter region with the duration

$$
\bar{t}_{\text{enc}}(\tilde{t}', u) \equiv \tilde{t}' + \frac{1}{\lambda} \ln\left(\frac{c}{|u|}\right) \tag{145}
$$

where $\tilde{t}' \in [0, (1/\lambda)\ln(c/|s|)]$ is the time interval between the nonlinearity event and the Poincaré surface of section $\mathcal{P}$ that is optimally chosen to be located in the center of the encounter region. As a consequence, we have to extend the integration over s and u, associated with the possible action differences su, by an integration over all possible time spans $\tilde{t}'$ defining the location of the nonlinearity event with respect to $\mathcal{P}$, which substitutes one of the integrations over time in Eq. (140). This yields the modified probability density

$$
\bar{w}(\Delta S, t, t'; T, T', n) = \int_{-c}^c \int_{-c}^c ds\,du \int_0^\infty d\tilde{t} \int_0^{(1/\lambda)\ln(c/|s|)} d\tilde{t}' \frac{\delta(\Delta S - su)}{\Sigma(\mu)\bar{t}_{\text{enc}}(\tilde{t}', u)} \exp\left(-n\frac{\bar{t}_{\text{enc}}(\tilde{t}', u)}{\tau_B}\right)
$$
$$
\times \delta\left[t + \tilde{t} + \bar{t}_{\text{enc}}(\tilde{t}', u) - T\right] \delta\left[t' + \bar{t}_{\text{enc}}(\tilde{t}', u) - T'\right]. \tag{146}
$$

Using this density for the calculation of diagram (d) in Fig. 7, we obtain

$$
\left\langle \psi_{\tilde{n}}^{(0)*} \left(\delta\psi_{\tilde{n}}^{(1)} \right) \right\rangle_{\text{loop, (d)}} =
$$

$$
= 2\frac{\hbar^2}{2m}\frac{|S_0|^4 (\pi\hbar)^3}{\tilde{W}W^2} \int_{-\infty}^{\infty} d(\Delta S) \int_0^{\infty} dt_2 \int_0^{\infty} dt_2' \sum_{\nu_1',\nu_2',\nu=\pm 1} \sum_{\gamma'} \left\langle \left| \widetilde{A}_{\gamma'} \left(\mathbf{z}_i^{\nu_2'}, \mathbf{z}_i^{\nu_1'}, \mu \right) \right|^2 \right\rangle
$$

$$
\times \left(-\frac{i}{\hbar} \right) \int_0^{\infty} dt_1' \sum_{\gamma} \left\langle \left| \widetilde{A}_{\gamma} \left[\mathbf{z}_{\tilde{n}}^{\nu}, \mathbf{r}_{\gamma'}(t_1'), \mu \right] \right|^2 \right\rangle
$$

$$
\times \bar{w}\left(\Delta S, t_2, t_2'; T_\gamma, T_{\gamma'} - t_1', 0\right) \exp\left(\frac{i}{\hbar}\Delta S\right) \exp\left(-\frac{t_2'}{\tau_B}\right)
$$

$$
= -i\frac{m}{p_{\tilde{n}}^1(\mu)} \left(j^{\mathrm{i}}\right)^2 \frac{1}{\tau_H^2} \int_0^{\infty} dt_2 \int_0^{\infty} dt_2' \int_0^{\infty} dt_1' \int_0^{\infty} dt_3' \exp\left(-\frac{t_1' + t_2' + t_3' + t_2}{\tau_D} - \frac{t_2'}{\tau_B} \right)
$$

$$
\times \int_{-c}^{c} ds \int_{-c}^{c} du \int_0^{(1/\lambda)\ln(c/|s|)} dt_1 \frac{1}{\Sigma(\mu)\bar{t}_{\text{enc}}(t_1, u)} \exp\left(\frac{i}{\hbar}su\right) \exp\left(-\frac{\bar{t}_{\text{enc}}(t_1, u)}{\tau_D}\right)
$$

$$
= -i\frac{m}{p_{\tilde{n}}^1(\mu)} \left(j^{\mathrm{i}}\right)^2 \left(\frac{\tau_D}{\tau_H}\right)^3 \tau_D \left(\frac{1}{1 + \tau_D/\tau_B}\right) = \left\langle \psi_{\tilde{n}}^{(0)*} \left(\delta\psi_{\tilde{n}}^{(1)} \right) \right\rangle_{\text{loop, (c)}} \tag{147}
$$

where we evaluate the integration over s, u and t_1 in Appendix Appendix E.2 yielding $1/\tau_H$. The calculation of the contribution of diagram (e) in Fig. 7 proceeds in perfect analogy with the one presented for diagram (d) and yields the same result

$$
\left\langle \psi_{\tilde{n}}^{(0)*} \left(\delta\psi_{\tilde{n}}^{(1)} \right) \right\rangle_{\text{loop, (e)}} = -i\frac{m}{p_{\tilde{n}}^1(\mu)} \left(j^{\mathrm{i}}\right)^2 \left(\frac{\tau_D}{\tau_H}\right)^3 \tau_D \left(\frac{1}{1 + \tau_D/\tau_B}\right) = \left\langle \psi_{\tilde{n}}^{(0)*} \left(\delta\psi_{\tilde{n}}^{(1)} \right) \right\rangle_{\text{loop, (c)}}. \tag{148}
$$

The overall nonlinear loop contribution to $\langle \psi_{\tilde{n}}^{(0)*}(\delta\psi_{\tilde{n}}^{(1)}) \rangle$ originating from the diagrams shown in Fig. 7 therefore sums up to

$$
\left\langle \psi_{\tilde{n}}^{(0)*} \left(\delta\psi_{\tilde{n}}^{(1)} \right) \right\rangle_{\text{loop}} = i\frac{m}{p_{\tilde{n}}^1(\mu)} \left(j^{\mathrm{i}}\right)^2 \left(\frac{\tau_D}{\tau_H}\right)^3 \tau_D \left[\left(\frac{1}{1 + \tau_D/\tau_B}\right)^2 - 2\left(\frac{1}{1 + \tau_D/\tau_B}\right) \right]. \tag{149}
$$

As this expression is purely imaginary, no modifications of transmission and reflection probabilities are expected in linear order in the interaction strength g, which is in perfect accordance with the discussion in Section 3.4 [see Eq. (102)].

4.3. Contributions of arbitrary order in the nonlinearity

As we can see from the above calculations, the presence of an encounter region perfectly fits to the picture of diagrams consisting of separated parts, which was developed in Section 3.5, since we can perform the integrations corresponding to an encounter region independently from the remaining integrations over link durations. Encounter regions can, in the spirit of Section 3.5, be interpreted as extended "blocks" which are connected via four links to other (nonlinearity or encounter) blocks as well as to the leads of the system. Care must

be taken, though, if a nonlinearity block enters the encounter region, as is the case in the diagrams depicted in the lower row of Fig. 7. Under consideration of the calculations performed in Appendix Appendix E, we can extend our diagrammatic rules listed in Section 3.5 by the following ones:

(7) each encounter region containing no nonlinearity event contributes a factor $-(1 + n\tau_B/\tau_D)/(\tau_D\tau_H)$ where $n = 0, 1, 2$ counts the number of trajectory pairs with imbalanced stretches within the encounter region (see Fig. 8);

(8) each encounter region including a nonlinearity event contributes a factor $1/\tau_H$.

As was already argued in Section 3.5, diagrams containing a nonlinearity block with ladder-type input (as the ones shown in the left and central column of Fig. 4) will not contribute to the reflection and transmission probabilities as they are cancelled by counterparts in which this nonlinearity block is attached to the complex conjugate trajectory stretch. We can therefore restrict ourselves to "crossed type" nonlinearity blocks shown in the right column in Fig. 4.

Figure 9 shows the complete set of nonlinear diagrams contributing to reflection and transmission probabilities in arbitrary order in the nonlinearity strength g. These diagrams consist of the same chains of nonlinearity blocks as the ones shown in Fig. 3, with the main difference that these chains cannot be directly attached to a lead as we are calculating the scattering amplitude to an arbitrary (i.e., not necessarily the incident) channel in the reflected or transmitted lead; instead, they have to be connected to ladder links via an encounter region. In perfect analogy with Fig. 7, the nonlinearity blocks at the right ends of the chains in the diagrams (a), (b), (d), and (e) can be moved all the way through the entire encounter region, thereby giving rise to a transition from diagram (a) to diagram (b) as well as from diagram (d) to diagram (e). The other blocks located at the ends of the chains in the diagrams (a) – (g) can, in analogy with the diagrams (d) and (e) of Fig. 7, be pushed into the encounter region by moving them along the trajectories that start or end at those blocks.

Using the diagrammatic rules (1) – (8) stated in Section 3.5 and above, the contributions of these relevant diagrams as well as their corrections due to nonlinearity events entering the encounter region are straightforwardly evaluated. Defining by

$$g_0 \equiv \left(j^i \tau_D c_{ii}^{(0)}\right)^{-1} = \left(j^{\mathrm{i}} \tau_D \frac{\tau_D}{\tau_H} \frac{1}{1 + \tau_D/\tau_B}\right)^{-1} \tag{150}$$

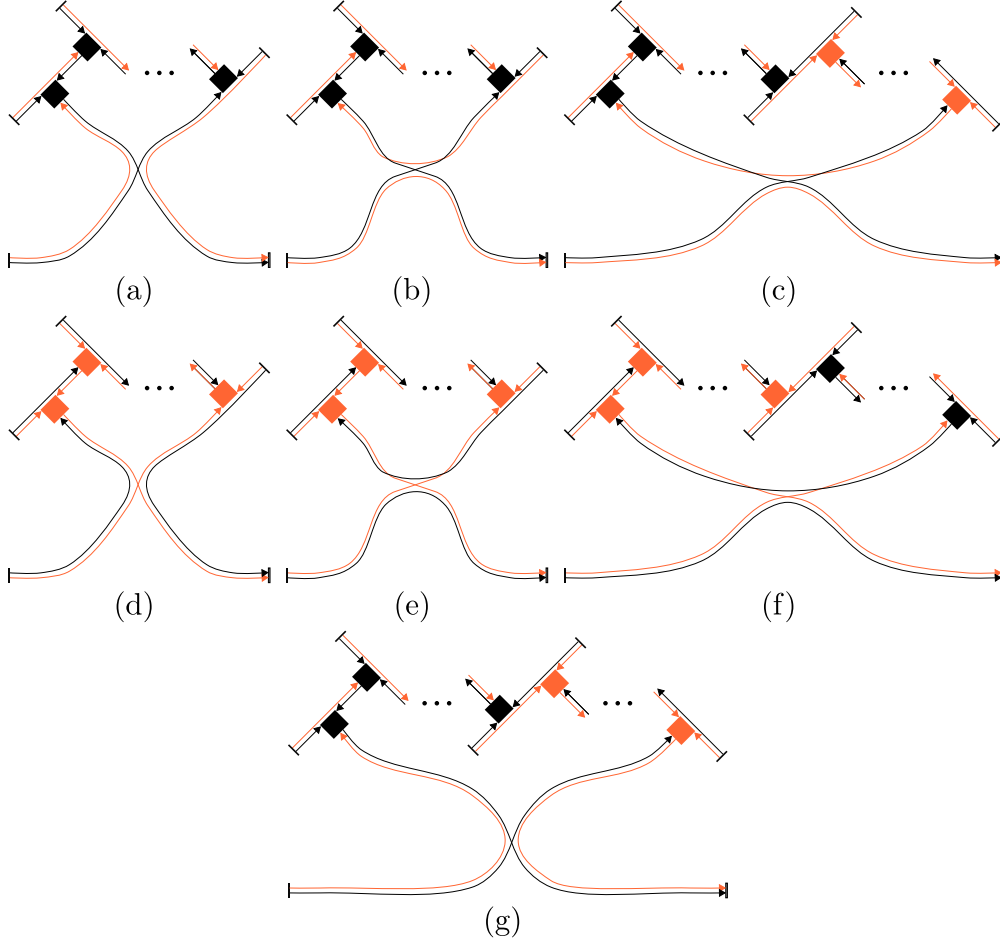the relevant scale for the nonlinearity strength appearing in Eq. (124), we obtain for the

Figure 9: Complete set of diagrams of k-th order in g containing one encounter region and k nonlinearity blocks of the "crossed" type shown in the right column of Fig. 4 which are located outside the encounter region. The diagrams (a) - (f) are contributions coming from $\langle \psi_{\tilde{n}}^{(0)*}(\delta\psi_{\tilde{n}}^{(k)}) \rangle$ and $\langle (\delta\psi_{\tilde{n}}^{(k)*})\psi_{\tilde{n}}^{(0)} \rangle$, respectively, where (c) and (f) only exist for $k \geq 2$. Contrary to the other diagrams, (g) is contained in $\langle (\delta\psi_{\tilde{n}}^{(k_1)*})(\delta\psi_{\tilde{n}}^{(k_2)}) \rangle$ with $k_1 + k_2 = k$ and $k_1, k_2 \geq 1$. As is shown in Eq. (158), the contributions of the diagrams (b), (c), (e), and (f) exactly cancel each other.

diagrams (a) – (g)

$$\left\langle \psi_{\tilde{n}}^{(0)*}\left(\delta\psi_{\tilde{n}}^{(k)}\right)\right\rangle_{\text{loop, (a)}} = \left[\left\langle \psi_{\tilde{n}}^{(0)}\left(\delta\psi_{\tilde{n}}^{(k)}\right)^*\right\rangle_{\text{loop, (d)}}\right]^*$$

$$= -\frac{m}{p_{\tilde{n}}^{\text{l}}(\mu)}j^{\text{i}}\left(\frac{\tau_D}{\tau_H}\right)^2\frac{1}{1+\tau_D/\tau_B}\left(-\frac{i}{g_0}\right)^k, \quad (151)$$

$$\left\langle \psi_{\tilde{n}}^{(0)*}\left(\delta\psi_{\tilde{n}}^{(k)}\right)\right\rangle_{\text{loop, (b)}} = \left[\left\langle \psi_{\tilde{n}}^{(0)}\left(\delta\psi_{\tilde{n}}^{(k)}\right)^*\right\rangle_{\text{loop, (e)}}\right]^*$$

$$= -\frac{m}{p_{\tilde{n}}^{\text{l}}(\mu)}j^{\text{i}}\left(\frac{\tau_D}{\tau_H}\right)^2\left(-\frac{i}{g_0}\right)^k, \quad (152)$$

$$\left\langle \psi_{\tilde{n}}^{(0)*}\left(\delta\psi_{\tilde{n}}^{(k_1+k_2)}\right)\right\rangle_{\text{loop, (c)}} = \left[\left\langle \psi_{\tilde{n}}^{(0)}\left(\delta\psi_{\tilde{n}}^{(k_1+k_2)}\right)^*\right\rangle_{\text{loop, (f)}}\right]^*$$

$$= -\frac{m}{p_{\tilde{n}}^{\text{l}}(\mu)}j^{\text{i}}\left(\frac{\tau_D}{\tau_H}\right)^2\left(-\frac{i}{g_0}\right)^{k_1}\left(\frac{i}{g_0}\right)^{k_2}, \quad (153)$$

$$\left\langle \left(\delta\psi_{\tilde{n}}^{(k_1)*}\right)\left(\delta\psi_{\tilde{n}}^{(k_2)}\right)\right\rangle_{\text{loop, (g)}} = -\frac{m}{p_{\tilde{n}}^{\text{l}}(\mu)}j^{\text{i}}\left(\frac{\tau_D}{\tau_H}\right)^2\frac{1}{1+\tau_D/\tau_B}\left(-\frac{i}{g_0}\right)^{k_1}\left(\frac{i}{g_0}\right)^{k_2} \quad (154)$$

where $\delta\psi_{\tilde{n}}^{(k_1+k_2)}$ denotes the k-th order contribution to $\psi_{\tilde{n}}$, whose diagrammatic representations contain k_1 nonlinearity blocks of the type ■ and k_2 complex conjugate nonlinearity blocks ■ . The corrections to these contributions due to nonlinearity events entering the encounter region are calculated as

$$\left\langle \psi_{\tilde{n}}^{(0)*}\left(\delta\psi_{\tilde{n}}^{(k)}\right)\right\rangle_{\text{loop, (a), correct}} = \left[\left\langle \psi_{\tilde{n}}^{(0)}\left(\delta\psi_{\tilde{n}}^{(k)}\right)^*\right\rangle_{\text{loop, (d), correct}}\right]^*$$

$$= 2\left\langle \psi_{\tilde{n}}^{(0)*}\left(\delta\psi_{\tilde{n}}^{(k)}\right)\right\rangle_{\text{loop, (b), correct}} = 2\left[\left\langle \psi_{\tilde{n}}^{(0)}\left(\delta\psi_{\tilde{n}}^{(k)}\right)^*\right\rangle_{\text{loop, (e), correct}}\right]^*$$

$$= 2\frac{m}{p_{\tilde{n}}^{\text{l}}(\mu)}j^{\text{i}}\left(\frac{\tau_D}{\tau_H}\right)^2\left(-\frac{i}{g_0}\right)^k, \quad (155)$$

$$\left\langle \psi_{\tilde{n}}^{(0)*}\left(\delta\psi_{\tilde{n}}^{(k_1+k_2)}\right)\right\rangle_{\text{loop, (c), correct}} = \left[\left\langle \psi_{\tilde{n}}^{(0)}\left(\delta\psi_{\tilde{n}}^{(k_1+k_2)}\right)^*\right\rangle_{\text{loop, (f), correct}}\right]^*$$

$$= \left\langle \left(\delta\psi_{\tilde{n}}^{(k_1)*}\right)\left(\delta\psi_{\tilde{n}}^{(k_2)}\right)\right\rangle_{\text{loop, (g), correct}} = 2\frac{m}{p_{\tilde{n}}^{\text{l}}(\mu)}j^{\text{i}}\left(\frac{\tau_D}{\tau_H}\right)^2\left(-\frac{i}{g_0}\right)^{k_1}\left(\frac{i}{g_0}\right)^{k_2}. \quad (156)$$

By multiplying these individual contributions with the corresponding powers of g and then summing over all orders k, k_1 and k_2 in analogy with Eq. (128), we finally obtain

$$\left\langle |\psi_{\tilde{n}}|^2\right\rangle_{\text{loop, (a) + (d)}} = -2\left\langle |\psi_{\tilde{n}}|^2\right\rangle_{\text{loop, (g)}} = 2\frac{mj^{\text{i}}}{p_{\tilde{n}}^{\text{l}}(\mu)}\frac{(\tau_D/\tau_H)^2}{1+\tau_D/\tau_B}\frac{(g/g_0)^2}{1+(g/g_0)^2} \quad (157)$$

43

for the summed contributions of the diagrams (a) and (d) as well as for the contributions of the diagrams (g), and

$$\left\langle|\psi_{\tilde{n}}|^2\right\rangle_{\text{loop, (b) + (e)}} = -\left\langle|\psi_{\tilde{n}}|^2\right\rangle_{\text{loop, (c) + (f)}} = 2\frac{mj^{\text{i}}}{p_{\tilde{n}}^{\text{l}}(\mu)}\left(\frac{\tau_D}{\tau_H}\right)^2\frac{(g/g_0)^2}{1+(g/g_0)^2} \tag{158}$$

for the summed contributions of the diagrams (b) and (e) as well as of (c) and (f), which implies that the contributions of these latter four diagrams exactly cancel each other. The summation of the associated corrections due to nonlinearity blocks entering the encounter region yields the contributions

$$-\left\langle|\psi_{\tilde{n}}|^2\right\rangle_{\text{loop, (a) +(d), correct}} = \left\langle|\psi_{\tilde{n}}|^2\right\rangle_{\text{loop, (c) + (f), correct}} = \frac{4mj^{\text{i}}}{p_{\tilde{n}}^{\text{l}}(\mu)}\left(\frac{\tau_D}{\tau_H}\right)^2\frac{(g/g_0)^2}{1+(g/g_0)^2}\,, \tag{159}$$

$$-\left\langle|\psi_{\tilde{n}}|^2\right\rangle_{\text{loop, (b) + (e), correct}} = \left\langle|\psi_{\tilde{n}}|^2\right\rangle_{\text{loop, (g), correct}} = \frac{2mj^{\text{i}}}{p_{\tilde{n}}^{\text{l}}(\mu)}\left(\frac{\tau_D}{\tau_H}\right)^2\frac{(g/g_0)^2}{1+(g/g_0)^2}\,, \tag{160}$$

which exactly cancel each other as well. In effect, therefore, only the diagrams (a), (d), and (g) provide nonvanishing contributions to the reflection or transmission probabilities, which are summed up as

$$\left\langle|\psi_{\tilde{n}}|^2\right\rangle_{\text{loop, (a)+(d)+ (g)}} = \frac{m}{p_{\tilde{n}}^{\text{l}}(\mu)}j^{\text{i}}\left(\frac{\tau_D}{\tau_H}\right)^2\frac{1}{1+\tau_D/\tau_B}\left(\frac{g}{g_0}\right)^2\frac{1}{1+(g/g_0)^2}\,. \tag{161}$$

Together with the result obtained in the linear case, the overall loop contribution to $\langle|\psi_{\tilde{n}}|^2\rangle$ reads

$$\begin{aligned}
\left\langle|\psi_{\tilde{n}}|^2\right\rangle_{\text{loop}} &= \left\langle|\psi_{\tilde{n}}^{(0)}|^2\right\rangle_{\text{loop}} + \left\langle|\psi_{\tilde{n}}|^2\right\rangle_{\text{loop, (a) +(d)+ (g)}} \\
&= -\frac{m}{p_{\tilde{n}}^{\text{l}}(\mu)}j^{\text{i}}\left(\frac{\tau_D}{\tau_H}\right)^2\frac{1}{1+\tau_D/\tau_B}\left[1-\left(\frac{g}{g_0}\right)^2\frac{1}{1+(g/g_0)^2}\right] \\
&= -\frac{m}{p_{\tilde{n}}^{\text{l}}(\mu)}j^{\text{i}}\left(\frac{\tau_D}{\tau_H}\right)^2\frac{1}{1+\tau_D/\tau_B}\frac{1}{1+(g/g_0)^2}\,,
\end{aligned} \tag{162}$$

which yields as the correction to the transmission and reflection probabilities

$$\delta(t_{\tilde{n}i})^{\text{loop}} = \frac{p_{\tilde{n}}^{\text{l}}(\mu)}{mj^{\text{i}}}\left\langle|\psi_{\tilde{n}}|^2\right\rangle_{\text{loop}} = -\left(\frac{\tau_D}{\tau_H}\right)^2\frac{1}{1+\tau_D/\tau_B}\frac{1}{1+(g/g_0)^2}\,. \tag{163}$$

As in the linear case [see Eq. (135)], this correction restores current conservation in the presence of the nonlinearity. With Eq. (124) we obtain

$$r_{ii} = \frac{1}{N_c+\tilde{N}_c} + \frac{(N_c+\tilde{N}_c-1)\,(1+\tau_D/\tau_B)}{(N_c+\tilde{N}_c)^2\,(1+\tau_D/\tau_B)^2+(gj^{\text{i}}\tau_D)^2} \tag{164}$$

44

for the probability of retro-reflection into the incident channel $n = i$, as well as

$$r_{ni} = t_{\tilde{n}i} = \frac{1}{N_c + \tilde{N}_c} - \frac{1 + \tau_D/\tau_B}{(N_c + \tilde{N}_c)^2 \left(1 + \tau_D/\tau_B\right)^2 + \left(gj^{\mathrm{i}}\tau_D\right)^2} \tag{165}$$

for the probability r_{ni} of reflection into a different channel $n \neq i$ of the incident lead and for the probability $t_{\tilde{n}i}$ of transmission into channel $\tilde{n}$. This yields the total reflection and transmission probabilities

$$R = \frac{N_c}{N_c + \tilde{N}_c} + \frac{\tilde{N}_c \left(1 + \tau_D/\tau_B\right)}{(N_c + \tilde{N}_c)^2 \left(1 + \tau_D/\tau_B\right)^2 + \left(gj^{\mathrm{i}}\tau_D\right)^2}, \tag{166}$$

$$T = \frac{\tilde{N}_c}{N_c + \tilde{N}_c} - \frac{\tilde{N}_c \left(1 + \tau_D/\tau_B\right)}{(N_c + \tilde{N}_c)^2 \left(1 + \tau_D/\tau_B\right)^2 + \left(gj^{\mathrm{i}}\tau_D\right)^2}, \tag{167}$$

which obviously satify $R + T = 1$.

5. Comparison with numerical results

Figures 10 and 11 display (in their right columns) the semiclassical prediction (164) for the probability of retro-reflection into the incident channel as evaluated for the billiards a and b, respectively, that are shown in Fig. 1. The sizes of the two billiards are chosen such that both the incident and the transmitted leads exhibit five open channels, i.e. $N_c = \tilde{N}_c = 5$, at the energy that corresponds to the chemical potential μ of the incident beam. We specifically have the areas $\Omega \simeq 3.41 \times 10^3 \, \hbar^2/(m\mu_0)$ for billiard a and $\Omega \simeq 3.29 \times 10^3 \, \hbar^2/(m\mu_0)$ for billiard b, where μ_0 defines the characteristic energy scale for the chemical potential of the atomic beam (i.e. we choose $\mu = \mu_0$ for the evaluation of the semiclassical retro-reflection probability). The incident current is chosen as $j^{\mathrm{i}} = 1.0 \, \mu_0/\hbar$. As described in Appendix Appendix D, the dwell time τ_D and the characteristic scale B_0 of the effective magnetic field were classically determined from the numerically computed length and area distributions within the two billiards, respectively; we obtained $j^{\mathrm{i}}\tau_D \simeq 267$ and $B_0 \simeq 1.55 \times 10^{-3} \, m\mu_0/\hbar \simeq 0.844 \times 2\pi\hbar/\Omega$ for billiard a as well as $j^{\mathrm{i}}\tau_D \simeq 241$ and $B_0 \simeq 4.21 \times 10^{-4} \, m\mu_0/\hbar \simeq 0.221 \times 2\pi\hbar/\Omega$ for billiard b.

In the linear case $g = 0$, a Lorentzian peak is obtained for the retro-reflection probability as a function of the effective magnetic field, on top of an incoherent background at $r_{ii} \simeq 1/(N_c + \tilde{N}_c) = 0.1$. This is the characteristic signature of weak localization. As is evident from Eq. (164), the presence of a finite nonlinearity g gives rise to a reduction of the coherent enhancement of the backscattering probability, which ultimately approaches the incoherent background $1/(N_c + \tilde{N}_c)$ for $g \to \infty$. This reduction, however, is more effective at the center of the backscattering peak than in its wings, such that for intermediate values of g a local minimum may be encountered in the reflection probability around $B = 0$.

This prediction is indeed confirmed by numerical computations of the quasi-stationary transport process within the two billiards under consideration. As explicit numerical propagations of the time-dependent Gross-Pitaevskii equation (5) are rather time-consuming, we use, in practice, a different approach in order to compute the scattering states of the system.
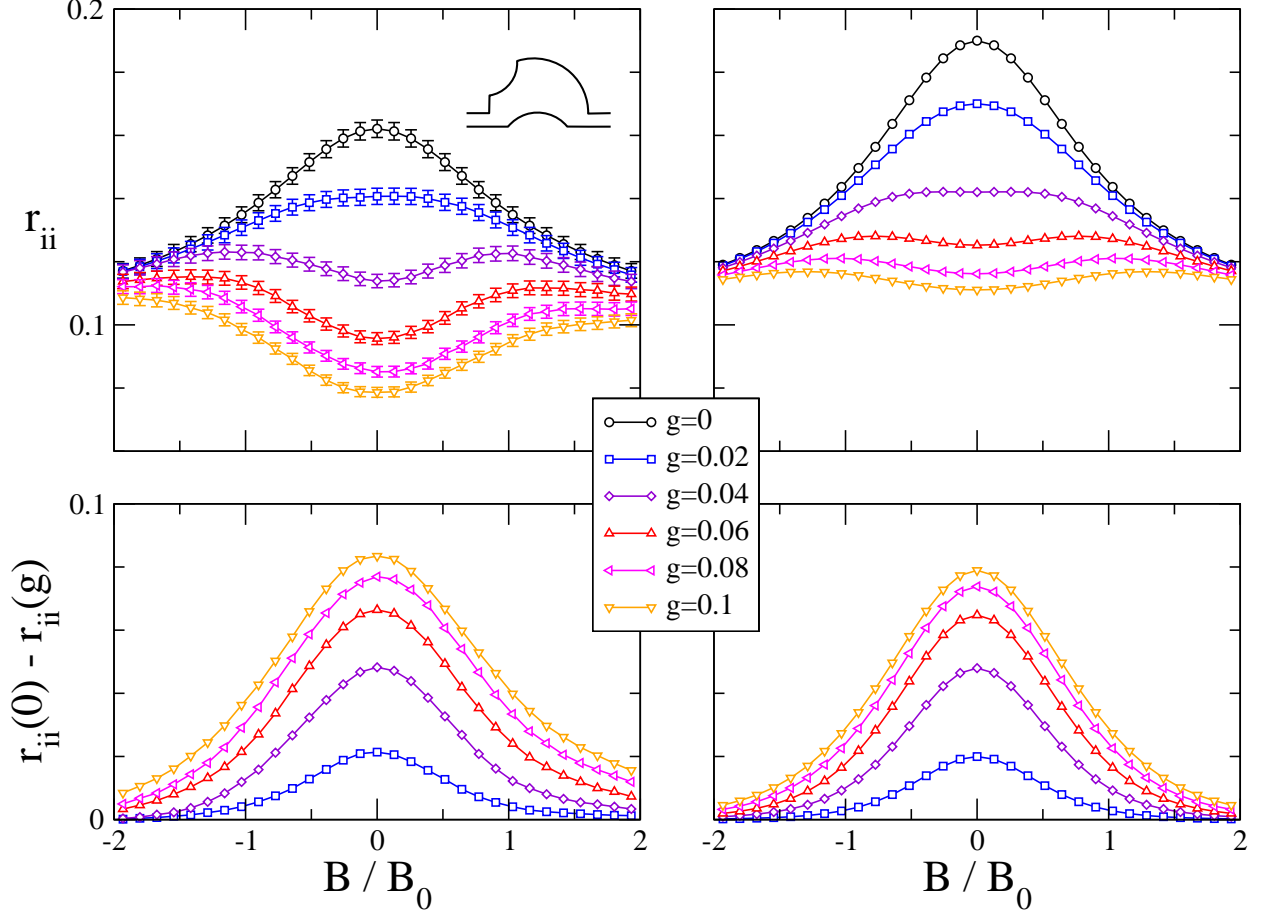
Figure 10: Nonlinearity-induced destruction of weak localization for the billiard a displayed in the left panel of Fig. 1. Plotted are the numerically computed backscattering probabilities (upper left panel) and their semiclassical prediction according to Eq. (164) (upper right panel) as a function of the effective magnetic field for various values of the nonlinearity g. We use the magnetic field scale $B_0 \simeq 1.55 \times 10^{-3} \, m\mu_0/\hbar$ and the average population $j^i\tau_D \simeq 267$, which were inferred from an analysis of the classical dynamics within the billiard. The lower panels display the differences of the backscattering probabilities for finite g with respect to the backscattering probabilities of the linear system. Good agreement is found between the numerical data (lower left panel) and the semiclassical prediction (right panel).
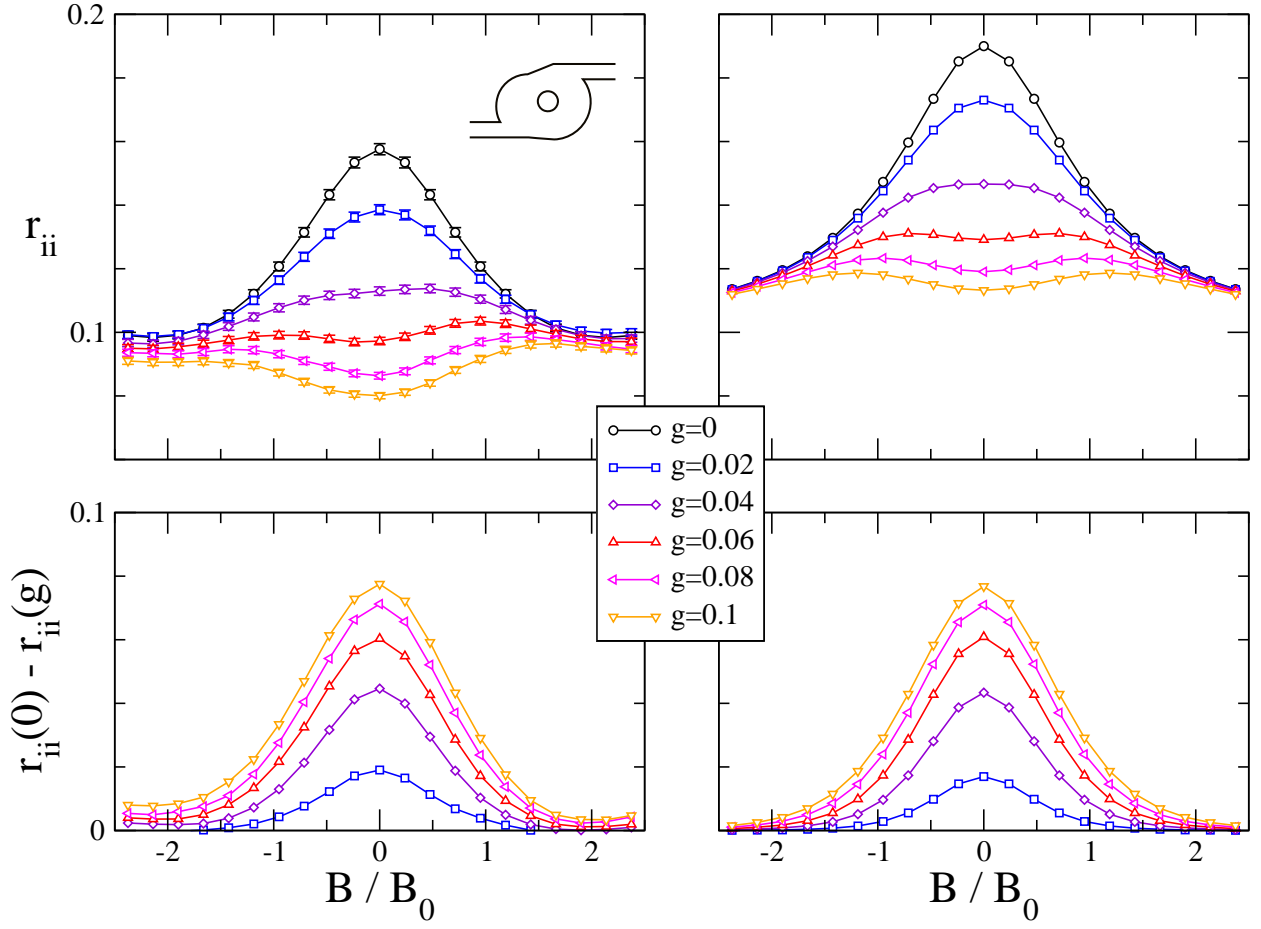
Figure 11: Same as Fig. 10 for the billiard b displayed in the right panel of Fig. 1. We use the magnetic field scale $B_0 \simeq 4.21 \times 10^{-4}\, m\mu_0/\hbar$ and the average population $j^i\tau_D \simeq 241$, which were inferred from an analysis of the classical dynamics within the billiard.
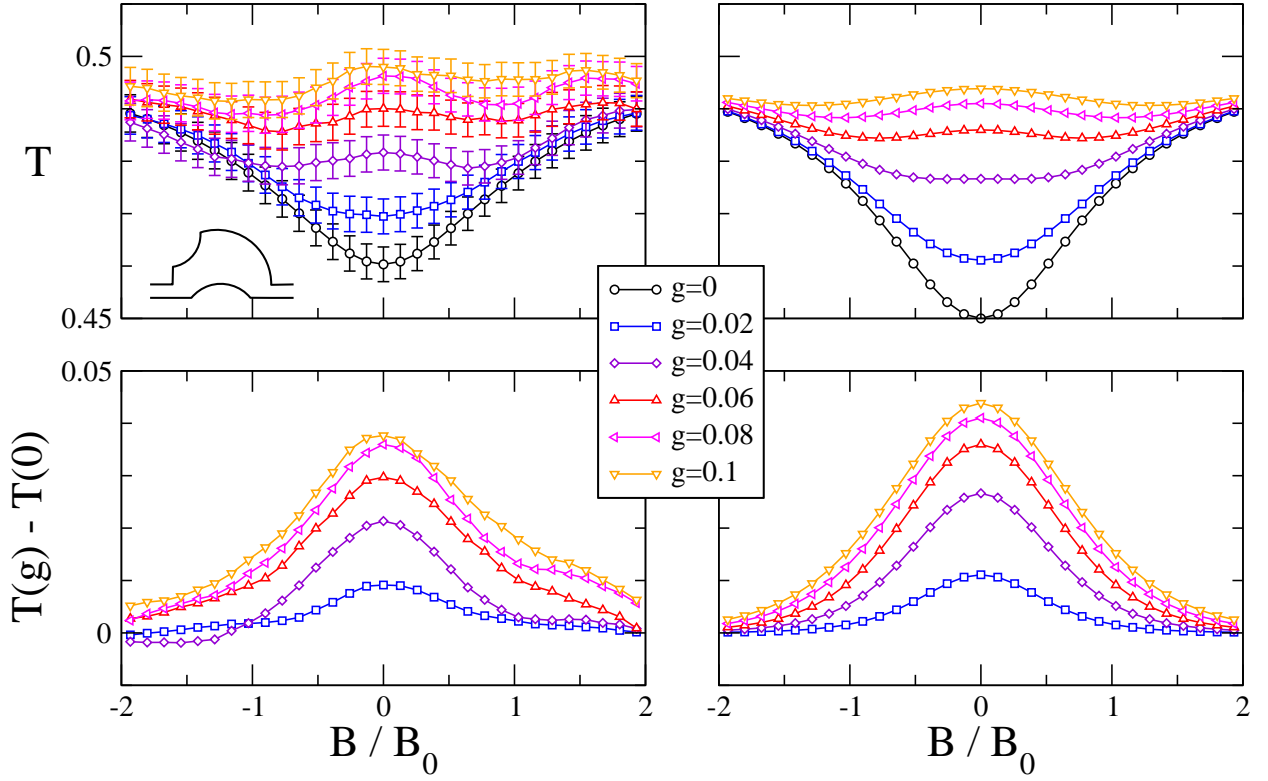
Figure 12: Total transmission for the billiard a. Plotted are the numerically computed transmission probabilities (upper left panel) and their semiclassical prediction according to Eq. (166) (upper right panel) as a function of the effective magnetic field for various values of the nonlinearity g, using the same parameters as for Fig. 10. The lower panels display the differences of the transmission probabilities for finite g with respect to the transmission probabilities of the linear system. Good agreement is found between the numerical data (lower left panel) and the semiclassical prediction (right panel).
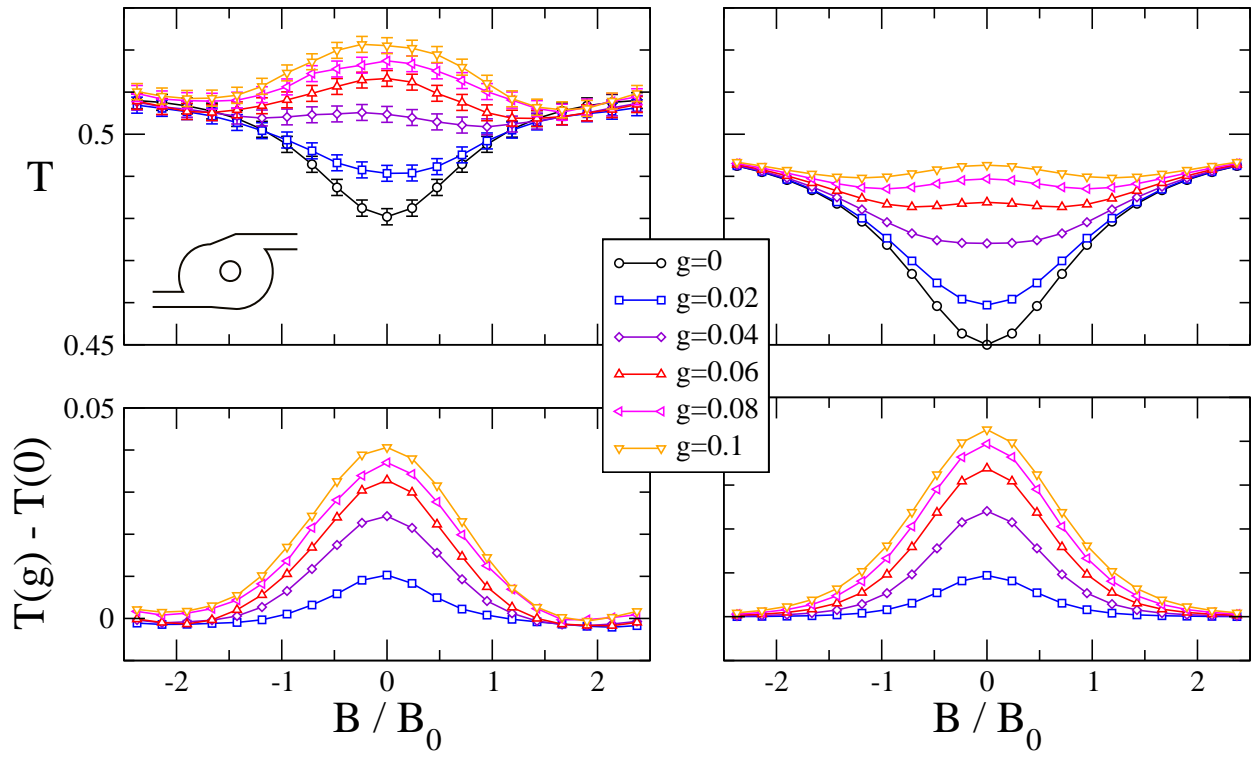
Figure 13: Same as Fig. 12 for the billiard b.

As explained in Appendix Appendix A, this approach uses a Newton search algorithm in order to construct selfconsistent scattering states of the nonlinear system. Among all those scattering states that are identified at given chemical potential μ and given incident current j^{i} (there is only one such scattering state in the linear system, but several of them generally exist in the presence of the nonlinearity, see, e.g., Ref. [61]), we select the one that would be first encountered in the presence of an adiabatic increase of the nonlinearity strength g. More technical details concerning this approach will be provided in a subsequent publication [62].

The left columns of Figs. 10 and 11 display the results that are obtained from these numerical computations. To obtain good statistics, we did not only perform an energy average of the reflection probability, within the energy interval $0.93\,\mu_0 \leq \mu \leq 1.18\,\mu_0$ for which there are exactly 5 open channels within each lead, but also averaged over different positions of the semicircular and circular obstacles in the case of billiard a and b, respectively. This additional configurational average is necessary as the above energy interval contains only a limited number of resonances within the billiard. Moreover, we averaged over different choices of the incident channel i, even though only the choice $i = 1$ appears realistic from the experimental point of view. The error bars attached to the data points consequently indicate the size of the statistical standard deviation that results from these averages.

As shown in the upper panels of Figs. 10 and 11, the relative height of the peak with respect to the incoherent background significantly deviates from the universal semiclassical prediction, even in the linear case $g = 0$. This discrepancy may, on the one hand, be attributed to a limited applicability of the semiclassical framework in our context. Indeed, as is seen in Fig. 1, the wavelength of the matter-wave beam is not sufficiently small to rule out the influence of possible diffraction effects at the rounded corners of the billiard. On the other hand, *nonuniversal* scattering phenomena that explicitly depend on the shape of the billiard under consideration may play a role. Specifically, among the backreflected trajectories that start and end in a given channel, there is possibly a significant fraction of *self-retracing* trajectories which are identical with their time-reversed counterpart. As those self-retracing trajectories do not contribute to the crossed part of the coherent backscattering probability, their semiclassical contribution then should be substracted from the sum-rule based expression (55) of the crossed density. Indeed, the presence of a prominent circular obstacle within billiard b should allow for a number of rather short self-retracing trajectories with a relatively small Lyapunov exponent (and therefore with a relatively large weight in the semiclassical Green function), namely those trajectories that directly head towards the obstacle, undergo a self-retracing reflection there, and subsequently exit the billiard in the incident channel. Similarly relevant self-retracing trajectories bouncing off the semicircular obstacles should exist in billiard a.

In view of the diagrammatic theory developed in Sec. 3, we note that such self-retracing trajectories do not affect the nonlinearity-induced *corrections* $c_{ii}^{(g)} - c_{ii}^{(0)}$ to the coherent backscattering probability. Indeed, as is evident e.g. from Eq. (103), those corrections are distinctly different from ladder contributions and will therefore not be overcounted if they happen to involve self-retracing trajectories. We consequently find, as shown in the lower panels of Figs. 10 and 11, rather good agreement between the numerical data and the
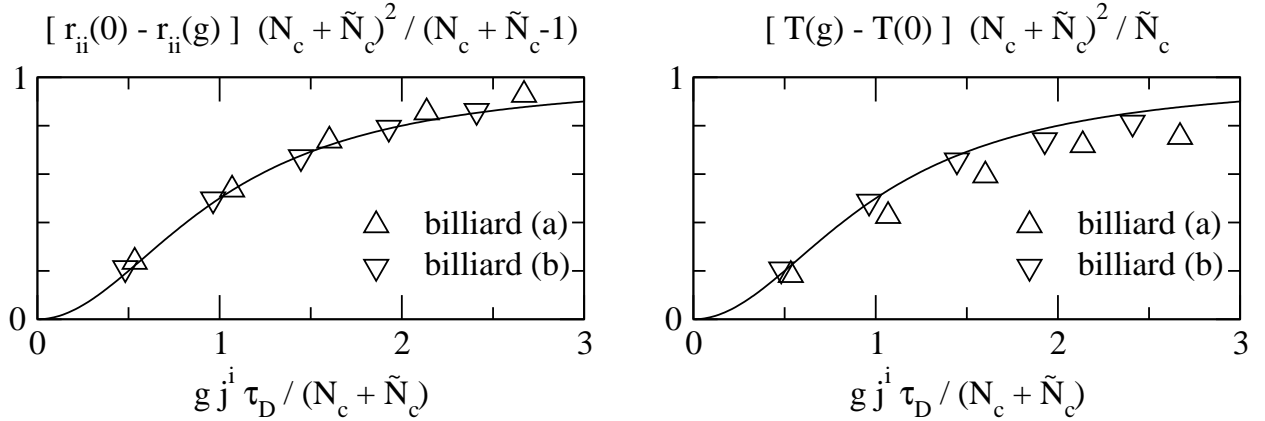
Figure 14: Change of height of the weak localization peak (or dip) at $B = 0$ as compared to the linear case. Plotted are, in the left panel, $[r_{ii}(g = 0) - r_{ii}(g)](N_c + \tilde{N}_c)^2/(N_c + \tilde{N}_c + 1)$ and, in the right panel, $[T(g) - T(g = 0)](N_c + \tilde{N}_c)^2/\tilde{N}_c$ as a function of $gj^i\tau_D/(N_c + \tilde{N}_c)$ for the two billiards under consideration. A comparison with the semiclassical predictions (164) and (167) (solid lines), which are given by $1/(1 + x^{-2})$ with $x \equiv gj^i\tau_D/(N_c + \tilde{N}_c)$ in both cases, shows good agreement.

semiclassical prediction if we specifically compare those corrections, i.e. the reduction of the weak localization peak with respect to the linear case $g = 0$. This is furthermore confirmed in the left panel of Fig. 14 which shows the reduction of the height of the weak localization peak at $B = 0$ as a function of the nonlinearity strength g. Renormalizing the horizontal and vertical axes in terms of the scales that are suggested by the analytical prediction (164), we find rather good agreement with this universal prediction for both billiards. This underlines the validity of the approach developed in Sections 3 and 4.

Finally, in order to demonstrate the relevance of the loop contributions, we show in Figs. 12, 13, and in the right panel of Fig. 14 the comparison of the numerical results for the transmission with our analytical prediction obtained from Eq. (167). Once again, excellent agreement is found after removing non-universal effects. Remarkably, Figs. 12 and 13 display asymmetries in the transmission as a function of the magnetic field, i.e. we do not necessarily have $T(-B) = T(B)$. This finding seems to constitute a violation of Onsager's relations [63] which state that the total mesoscopic transmission $\mathcal{T} \equiv \sum_i \sum_{\tilde{n}} |t_{\tilde{n}i}|^2$, which represents the incoherent sum over the individual transmissions that result from all available choices of the incident channel i (and which is implicitly computed in Figs. 12 and 13 due to the averaging over the incident channel), be symmetric in the magnetic field B for any given scattering geometry at any given chemical potential. It should be noted, however, that Onsager's relations are based on the unitarity of the scattering matrix S and its symmetry property $S(-B) = S^T(B)$ [64] and thereby implicitly rely on the linearity of the scattering process. Indeed, computing the total mesoscopic transmission $\mathcal{T}$ across billiard b in the absence of interaction for a specific choice of the chemical potential, we obtain perfect symmetry of $\mathcal{T}$ in B as shown in Fig. 15. This symmetry is broken at finite values of the nonlinearity g. Similar findings have been reported in electronic transport through mesoscopic structures
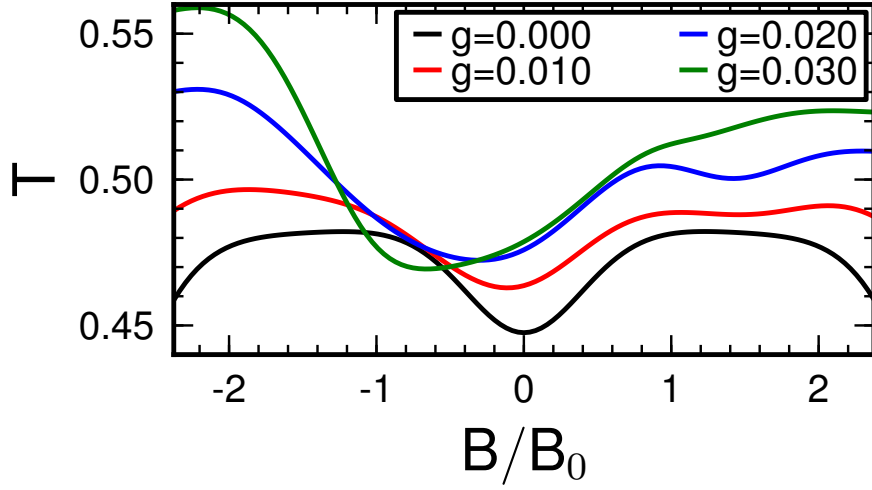
Figure 15: Total mesoscopic transmission $\mathcal{T} = \frac{1}{N_c}\sum_i\sum_{\tilde{n}}|t_{\tilde{n}i}|^2$ as a function of the magnetic field B for billiard b at a fixed chemical potential $\mu = 1.08306\,\mu_0$ and at different strengths of the nonlinearity g. In the absence of interaction (black curve), $\mathcal{T}$ is symmetric in B, which is a consequence of Onsager's relations [63]. This symmetry in B is, however, broken in the presence of the nonlinearity (red, blue, and green curves). A sufficiently large energetic and configurational average would restore the symmetry in B as is visible in Fig. 13.

in the presence of strong bias voltages [65, 66].

6. Conclusion

In summary, we studied, both analytically and numerically, weak localization of guided matter waves that originate from interacting Bose-Einstein condensates and propagate through chaotic billiard geometries. Our analytical approach is based on a nonlinear diagrammatic perturbation theory [30, 31, 32] that originates from the Gross-Pitaevskii equation, which is combined with a semiclassical expansion of the linear (single-particle) Green function within the billiard. Summing all terms of this diagrammatic perturbation theory and utilizing standard semiclassical sum rules in ergodic billiards, we obtain analytical expressions for the retro-reflection probability [Eq. (164)] as well as for the total reflection and transmission [Eqs. (166) and (167)] in dependence of the effective interaction strength and of the strength of an artifical gauge field that breaks time-reversal invariance and simulates the effect of a magnetic field for charged particles. These expressions also involve the analysis of loop corrections in leading order [28] which restore current conservation.

Globally, we find that the peak of weak localization decreases with increasing nonlinearity strength g and eventually disappears beyond a characteristic scale of g given by the inverse average population within the billiard. This suggests that the presence of the nonlinearity introduces an additional dephasing mechanism that affects the constructive interference between backscattered trajectories and their time-reversed counterparts. The decrease of the peak height with g is found to be stronger at the center of the peak (i.e. for vanishing

gauge field $B = 0$) than in its wings, which eventually gives rise to a tiny local dip in the backscattering probability around $B = 0$. While this dip, as it is predicted by the general semiclassical theory, is presumably too small to be of experimental relevance, it can be more pronounced in individual billiard geometries, as the ones specifically studied in this work, in which the backscattering probability develops a global minimum, instead of a maximum, at $B = 0$. We thereby encounter a signature of *weak antilocalization* in those billiards, which is of genuinely different nature than antilocalization in electronic transport processes involving spin-orbit interaction [26].

Comparisons of the numerically computed absolute and relative heights of the weak localization peaks with the semiclassical prediction seem to suggest that this weak antilocalization-type phenomenon is caused by the occurence of *self-retracing* trajectories in the scattering system. Indeed, the presence of such self-retracing trajectories reduces the probability for coherent backscattering as compared to the universal semiclassical prediction in the linear case, as the application of the standard sum rule would give rise to an overcounting of interference contributions between backscattered trajectories and their time-reversed counterparts. It does, however, not affect the nonlinearity-induced corrections to this coherent backscattering probability. Consequently, the peak of weak localization can turn into a finite dip in billiard geometries that exhibit prominent self-retracing trajectories of short length and therefore of large weight in the semiclassical backscattering amplitude.

This observation also sheds new light on the inversion of the coherent backscattering peak that was found in the coherent propagation of Bose-Einstein condensates through two-dimensional disorder potentials [25]. As a matter of fact, such disorder potentials also exhibit self-retracing trajectories, which essentially arise from a retro-reflection at the first impurity that the incident matter wave encounters within the disorder region. Diagrammatic calculations within such disordered systems [67] do indeed suggest that short reflected paths are at the origin of the inversion of the coherent backscattering peak in disordered systems.

In this study, we considered a number of idealizations concerning the setup for the matter-wave transport process. For the sake of analytical tractability of the problem, we particularly imposed hard-wall boundaries of the wave guides and the billiard and assumed a continuous monochromatic flow of atoms through this scattering region. We are convinced, however, that the phenomenology studied in this work should be sufficiently robust to manifest also in the case of harmonic waveguides and harmonic-like confinement geometries with chaotic (or mixed regular-chaotic) dynamics, which could possibly be realized by combinations of red- and blue-detuned laser beams that are perpendicularly focused onto the waveguide, as well as in the case of atomic wave packet scattering processes which may be easier to realize than guided atom-laser beams. Weak localization and antilocalization of interacting Bose-Einstein condensates should therefore be observable with present-day cold-atom technologies.

Appendix A. Numerical computation of stationary scattering states

In this appendix, we explain how we numerically compute stationary solutions $\psi \equiv \psi(\mathbf{r})$ of the time-dependent inhomogeneous Gross-Pitaevskii equation (5). Such stationary solutions satisfy the nonlinear equation

$$[\mu - H]\,\psi(\mathbf{r}) - g(\mathbf{r})\frac{\hbar^2}{2m}|\psi(\mathbf{r})|^2\psi(\mathbf{r}) - S(\mathbf{r}) = 0 \qquad (A.1)$$

with $S(\mathbf{r}) = S_0\chi_i(y)\delta(x - x_L)$, which is equivalent to Eq. (62). This equation is discretized on a two-dimensional lattice where only points inside the cavity and the leads are taken into account. The single-particle Hamiltonian H given by Eq. (6) can be approximated using a finite-difference scheme [63] where we incorporate the vector potential using a Peierls phase [68]. We choose the lattice spacing Δ small enough that the approximation error [which scales as $\mathcal{O}(\Delta^2)$] becomes negligible, which is the case for roughly 30 lattice points per wavelength. The interaction strength $g(\mathbf{r})$ is, as explained in Ref. [69], considered to be constant within the scattering region and adiabatically ramped off in the leads [70]. The effects of the infinite leads can then be incorporated through self-energies as in the recursive Green function method [64, 71], which allows one to restrict the numerical computation to a finite spatial region.

The complex solution $\psi(\mathbf{r})$ of the nonlinear wave equation (A.1) can be represented as a $2\mathcal{N}$-dimensional real vector where $\mathcal{N}$ is the number of grid points. Defining

$$F : \mathbb{R}^{2\mathcal{N}} \longrightarrow \mathbb{R}^{2\mathcal{N}}, \psi(\mathbf{r}) \longmapsto [\mu - H_0]\,\psi(\mathbf{r}) - g(\mathbf{r})\frac{\hbar^2}{2m}|\psi(\mathbf{r})|^2\psi(\mathbf{r}) - S(\mathbf{r})\,, \qquad (A.2)$$

we search now for a solution of $F(\psi) = 0$. This is done with Newton's method [72]. One selects a starting vector $\psi_0(\mathbf{r})$ and constructs a sequence of vectors $\{\psi_k\}_{k=1}^{\infty}$ (here k is the iteration number) using the iteration $\psi_{k+1} = \psi_k - (\mathcal{D}F)^{-1}F(\psi_k)$. If the derivate $\mathcal{D}F$ at the solution is not singular, this iteration is guaranteed to converge to a solution of the nonlinear equation (A.1), provided the starting vector is chosen in a suitably close vicinity of this solution.

The efficiency of this method strongly depends on the starting vector $\psi_0(\mathbf{r})$. An obvious choice would be the solution of the linear wave equation (for $g = 0$). This choice, however, works out only for very small nonlinearities. In the general case, one has to use a continuation method [72, 73]. To this end, we consider g, i.e. the constant value of the interaction strength within the billiard [74], as an additional free parameter and reinterpret $F \equiv F[\psi(\mathbf{r}); g]$ as a function $F : \mathbb{R}^{2\mathcal{N}} \times \mathbb{R} \to \mathbb{R}^{2\mathcal{N}}$. Now $F^{-1}(0)$ is a one-dimensional manifold [75] which can be conveniently parametrized by the arclength s through the parametric curve $s \mapsto [g(s), \psi(s)]$. Starting from $g = 0$, the numerical algorithm follows this curve until the desired value g of the nonlinearity strength is reached, and returns the wavefunction $\psi(\mathbf{r})$ that is obtained at the end of this curve-tracking process [76].

Fig. A.16 shows, for a specific set of parameters, a projection of this curve onto the two-dimensional parameter space spanned by the nonlinearity strength g and the total transmission that is associated with the stationary scattering state $\psi(\mathbf{r})$. As is characteristic for
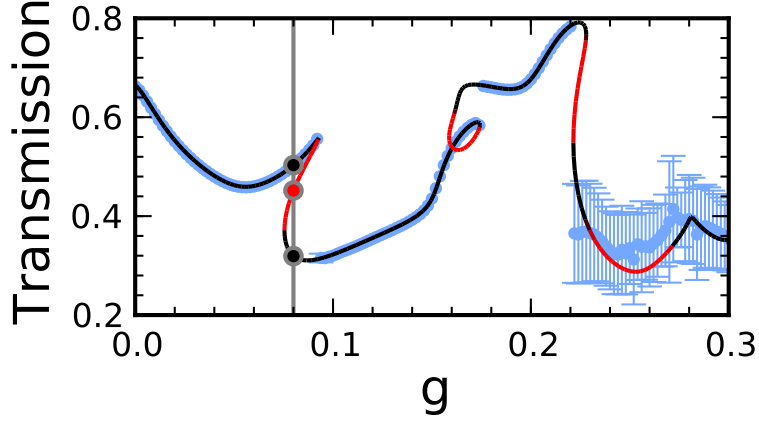
Figure A.16: Transmission of the stationary scattering state versus the interaction strength g as obtained from the numerical curve-tracking method. Black lines indicate dynamically stable, red lines dynamically unstable branches. Due to the nonlinearity in the wave equation, several scattering states with different transmissions may be encountered at a given value of g. At $g = 0.08$ for instance, there are three different scattering states, two of them being dynamically stable (black dots) and one being unstable (red dot). The light-blue data points show the time-averaged transmissions that are obtained from a numerical simulation of the time-dependent scattering process in the presence of an adiabatically slow ramping of the source amplitude. As is visible from the error bars which indicate the associated standard deviation of the transmission at given value of g, the atomic current through the billiard develops a pronounced time dependence in the absence of stable stationary scattering states (e.g. around $g = 0.25$). The calculation is done for billiard b at $B = -0.001\, m\mu_0/\hbar$ and $\mu = 0.935102\, \mu_0$, with the condensate being injected in the transverse ground mode ($i = 1$) of the incident lead.

nonlinear wave equations, several stationary solutions are found for some values of g, e.g. at $g = 0.08$. Some of these solutions may be dynamically unstable and can therefore not be populated in the time-dependent propagation process. At sufficently large values of the nonlinearity, no dynamically stable scattering state is found any longer, which implies that the scattering process becomes permanently time-dependent and develops turbulent-like behaviour [41].

To determine the dynamical stability of the numerically computed stationary scattering state, we linearize the time-dependent Gross-Pitaevskii equation around the stationary solution $\psi(\mathbf{r})$ using the Bogoliubov ansatz

$$\tilde{\psi}(\mathbf{r},t) = [\psi(\mathbf{r}) + u(\mathbf{r}) \exp\left(-i\xi t\right) + v^*(\mathbf{r}) \exp\left(i\xi^* t\right)] \exp\left(-\frac{i}{\hbar}\mu t\right) \tag{A.3}$$

for the time-dependent scattering wavefunction $\tilde{\psi}(\mathbf{r}, t)$. This leads to the Bogoliubov-de Gennes equation [77]

$$\begin{pmatrix} H - \mu + 2g(\mathbf{r})\frac{\hbar^2}{2m}|\psi(\mathbf{r})|^2 & g(\mathbf{r})\frac{\hbar^2}{2m}[\psi(\mathbf{r})]^2 \\ g(\mathbf{r})\frac{\hbar^2}{2m}[\psi^*(\mathbf{r})]^2 & H - \mu + 2g(\mathbf{r})\frac{\hbar^2}{2m}|\psi(\mathbf{r})|^2 \end{pmatrix} \begin{pmatrix} u(\mathbf{r}) \\ v(\mathbf{r}) \end{pmatrix} = \hbar\xi \begin{pmatrix} +1 & 0 \\ 0 & -1 \end{pmatrix} \begin{pmatrix} u(\mathbf{r}) \\ v(\mathbf{r}) \end{pmatrix}. \tag{A.4}$$
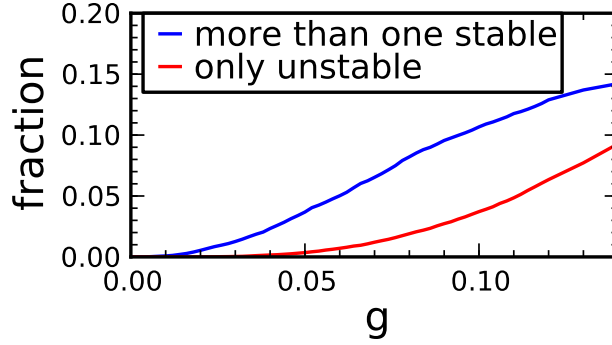
Figure A.17: This figure shows as a function of g the fraction of configurations of B, μ and the incident mode i that exhibit only dynamically unstable solutions (red curve) or support more than one dynamically stable solution (blue curve). In the latter case, we select the one that is first encountered in the curve-tracking algorithm starting from $g = 0$.

This generalized eigenvalue problem is numerically solved using the implicit restarted Arnoldi method as realized in the software library `ARPACK` [78]. Special care must be taken in order to describe the infinite leads properly. This is done using the method of smooth exterior complex scaling [79] which exponentially damps the outgoing waves of the collective modes in the leads. As a consequence, the Bogoliubov eigenfrequencies ξ become *complex*. If one of them is found to exhibit a positive imaginary part, i.e. $\text{Im}(\xi) > 0$, we can infer from Eq. (A.3) that the scattering state $\psi(\mathbf{r})$ under consideration is dynamically unstable.

Fig. A.17 shows (red curve) the fraction of parameter configurations of the chemical potential μ, the magnetic field B, and the incident mode number i for which no dynamically stable scattering state is found. This fraction of unstable configurations is found to increase with the nonlinearity strength g, which imposes restrictions on the shape of the cavities and the maximum value of g one can use for numerical simulations. In particular, we find that the fraction of configurations that support no stable solution increases rather rapidly with g for small widths of the leads, i.e. for a very low number of open channels. This is attributed to the reduced spectral width that quasi-bound resonance states within the billiard exhibit in that case, which in turn leads to an enhanced interaction energy $\int d\mathbf{r} g(\mathbf{r}) |\psi(\mathbf{r})|^4$ at such resonances. Rather wide leads with a large number of open channels, on the other hand, compromise the effect of weak localization and reduce the visibility of its signature in the reflection and transmission probabilities. For the billiard sizes and geometries under consideration, the fraction of configurations with unstable solutions remains below 0.02 until $g = 0.08$.

When encountering a configuration with only unstable solutions, we select the one that exhibits the smallest Lyapunov exponent, the latter being defined by the largest imaginary part of the eigenvalues ξ of the Bogoliubov-de Gennes equations (A.4). This choice is supported by time-dependent propagations of the inhomogeneous Gross-Pitaevskii equation (5), which directly simulate, as in Ref. [25], the time-dependent scattering process in the presence of an adiabatic increase of the source amplitude. In such simulations, which were carried out

for specific parameter configurations, we find, for not too large values of g, that the time-dependent current in the transmitted lead displays regular oscillations around the current of the stationary solution that is the least unstable one and exhibits the smallest Lyapunov exponent. The *time-averaged* transmission, which is the main experimental observable in such scattering processes, is then correctly reproduced by the transmission of the unstable stationary scattering state. For larger values of g, however, the time-dependent dynamics of the propagating wavefunction becomes chaotic, which means that the transmission associated with an unstable stationary scattering state loses its significance.

Appendix B. The eikonal approximation

In this appendix, we explicitly derive the semiclassical expression for the Green function in the presence of a weak perturbation of the Hamiltonian. Considering the Hamiltonian $H = H_0 + \delta H$ with $H_0 \equiv H_0(\mathbf{p}, \mathbf{r})$ the unperturbed part and $\delta H \equiv \delta H(\mathbf{p}, \mathbf{r})$ a perturbation that is slowly varying with $\mathbf{r}$, and defining $G_0 \equiv (E - H_0 + i0)^{-1}$, we can express the Green function of the system by means of a Dyson equation of the form

$$G \equiv (E - H + i0)^{-1} = G_0 + G_0 \delta H G = G_0 \sum_{k=0}^{\infty} (\delta H G_0)^k \,. \tag{B.1}$$

Let us first evaluate the first-order term of this Born series,

$$\delta G^{(1)}(\mathbf{r}, \mathbf{r}', E) \equiv \langle \mathbf{r} | G_0 \delta H G_0 | \mathbf{r}' \rangle = \int d^2 r'' G_0(\mathbf{r}, \mathbf{r}'', E) \delta H(\hat{\mathbf{p}}, \mathbf{r}'') G_0(\mathbf{r}'', \mathbf{r}', E) \,, \tag{B.2}$$

in the semiclassical approximation. Using the semiclassical expression (10) for the Green function,

$$G_0(\mathbf{r}, \mathbf{r}', E) = \sum_{\gamma} A_\gamma(\mathbf{r}, \mathbf{r}', E) \exp\left[\frac{i}{\hbar} S_\gamma(\mathbf{r}, \mathbf{r}', E) - i\frac{\pi}{2}\mu_\gamma\right] \,. \tag{B.3}$$

we see that the momentum operator $\hat{\mathbf{p}}$ in δH acts, in leading semiclassical order (i.e., in lowest order in $\hbar$), only on the action integrals $S_\gamma(\mathbf{r}'', \mathbf{r}', E)$ in the exponents. This means that $\hat{\mathbf{p}}$ can be replaced by the final momenta of the trajectories leading from $\mathbf{r}'$ to $\mathbf{r}''$. We therefore obtain

$$\delta G^{(1)}(\mathbf{r}, \mathbf{r}', E) = \int d^2 r'' \sum_{\gamma_1, \gamma_2} A_{\gamma_2}(\mathbf{r}, \mathbf{r}'', E) A_{\gamma_1}(\mathbf{r}'', \mathbf{r}', E) \delta H(\mathbf{p}'', \mathbf{r}'')$$
$$\times \exp\left\{\frac{i}{\hbar}[S_{\gamma_2}(\mathbf{r}, \mathbf{r}'', E) + S_{\gamma_1}(\mathbf{r}'', \mathbf{r}', E)] - i\frac{\pi}{2}(\mu_{\gamma_1} + \mu_{\gamma_2})\right\} \tag{B.4}$$

with $\mathbf{p}'' \equiv \mathbf{p}_{\gamma_1}^{\mathrm{f}}(\mathbf{r}'', \mathbf{r}', E)$, where the indices γ_1 and γ_2 respectively represent the trajectories from $\mathbf{r}'$ to $\mathbf{r}''$ and from $\mathbf{r}''$ to $\mathbf{r}$.

Using now the fact that A_{γ_1}, A_{γ_2}, and $\delta H(\mathbf{p}'', \mathbf{r}'')$ are slowly varying functions of $\mathbf{r}''$ on the length scale of the de Broglie wavelength of the atoms, we can apply the stationary phase approximation to evaluate the integral over $\mathbf{r}''$. The stationary phase condition yields

$$\frac{\partial}{\partial \mathbf{r}''} \left[S_{\gamma_2}(\mathbf{r}, \mathbf{r}'', E) + S_{\gamma_1}(\mathbf{r}'', \mathbf{r}', E) \right] = 0 \,, \tag{B.5}$$

i.e., $\mathbf{p}_{\gamma_1}^{\mathrm{f}}(\mathbf{r}'', \mathbf{r}', E) = \mathbf{p}_{\gamma_2}^{\mathrm{i}}(\mathbf{r}, \mathbf{r}'', E)$. This condition is satisfied if and only if the trajectory γ_2 is the direct continuation of γ_1. The double sum in Eq. (B.4) can therefore be contracted to a single sum over trajectories γ that are going from $\mathbf{r}'$ to $\mathbf{r}$ at energy E. Combining the prefactors that result from the spatial integration perpendicular to this trajectory as well as from the amplitudes $A_{\gamma_1}, A_{\gamma_2}$, and transforming the spatial integration parallel to the trajectory into an integration along the propagation time, we finally obtain

$$\delta G^{(1)}(\mathbf{r}, \mathbf{r}', E) = -\frac{i}{\hbar} \sum_\gamma A_\gamma(\mathbf{r}, \mathbf{r}', E) \exp\left[\frac{i}{\hbar} S_\gamma(\mathbf{r}, \mathbf{r}', E) - i\frac{\pi}{2}\mu_\gamma \right] \int_0^{T_\gamma} \delta H[\mathbf{p}_\gamma(t), \mathbf{q}_\gamma(t)]dt \,. \tag{B.6}$$

Similarly, higher order terms in the Born series (B.1) can be evaluated yielding

$$\begin{aligned}
\delta G^{(k)}(\mathbf{r}, \mathbf{r}', E) &\equiv \langle \mathbf{r}|G_0(\delta H G_0)^k|\mathbf{r}'\rangle \\
&= \sum_\gamma A_\gamma(\mathbf{r}, \mathbf{r}', E) \exp\left[\frac{i}{\hbar} S_\gamma(\mathbf{r}, \mathbf{r}', E) - i\frac{\pi}{2}\mu_\gamma \right] \\
&\quad \times \frac{1}{k!}\left(-\frac{i}{\hbar}\int_0^{T_\gamma} \delta H[\mathbf{p}_\gamma(t), \mathbf{q}_\gamma(t)]dt \right)^k \,.
\end{aligned} \tag{B.7}$$

This finally yields the modified Green function

$$G(\mathbf{r}, \mathbf{r}', E) = \sum_\gamma A_\gamma(\mathbf{r}, \mathbf{r}', E) \exp\left[\frac{i}{\hbar} S_\gamma(\mathbf{r}, \mathbf{r}', E) - i\frac{\pi}{2}\mu_\gamma - \frac{i}{\hbar}\phi_\gamma(\mathbf{r}, \mathbf{r}', E) \right] \tag{B.8}$$

where

$$\phi_\gamma(\mathbf{r}, \mathbf{r}', E) \equiv \int_0^{T_\gamma} \delta H[\mathbf{p}_\gamma(t), \mathbf{q}_\gamma(t)]dt \,. \tag{B.9}$$

represents an effective modification of the action integral S_γ due to the presence of the perturbation. Eq. (B.8) reflects a general result in classical mechanics that, to leading order in the perturbation, the action difference between unperturbed and perturbed orbits is, for periodic orbits, given by Eq. (B.9) [80].

In the case of a perturbation due to a weak magnetic field, we have

$$\delta H(\mathbf{p}, \mathbf{r}) = -\frac{1}{m}\mathbf{A}(\mathbf{r}) \cdot \mathbf{p} + \frac{1}{2m}\mathbf{A}^2(\mathbf{r}) \,. \tag{B.10}$$

Hence, we can write $\phi_\gamma = -\varphi_\gamma - \tilde{\varphi}_\gamma$ with

$$\varphi_\gamma(\mathbf{r}, \mathbf{r}', E) \equiv \frac{1}{m}\int_0^{T_\gamma} \mathbf{p}_\gamma(t) \cdot \mathbf{A}[\mathbf{q}_\gamma(t)]dt \,, \tag{B.11}$$

$$\tilde{\varphi}_\gamma(\mathbf{r}, \mathbf{r}', E) \equiv -\frac{1}{2m}\int_0^{T_\gamma} \mathbf{A}^2[\mathbf{q}_\gamma(t)]dt \tag{B.12}$$

58

corresponding, respectively, to a paramagnetic and a diamagnetic contribution to the effective action integral.

Also the presence of a weak nonlinearity within the scattering system can be accounted for in this framework, provided only ladder contributions are considered. Comparing Eq. (66) in the cases (68) and (68) with Eq. (B.2), we see that we have to set

$$\delta H(\mathbf{r}) = 2g \frac{\hbar^2}{2m} |\psi^{(0)}(\mathbf{r})|_d^2 \tag{B.13}$$

where $|\psi^{(0)}(\mathbf{r})|_d^2$ represents, according to Eq. (72), the density at position $\mathbf{r}$ as evaluated within the diagonal approximation. We then obtain the effective modification of the action integral [defined by $\chi_\gamma(\mathbf{r}, \mathbf{r}', \mu)$ in Sec. 3.3] as

$$\phi_\gamma(\mathbf{r}, \mathbf{r}', \mu) = g \frac{\hbar^2}{m} \int_0^{T_\gamma} |\psi^{(0)}[\mathbf{q}_\gamma(t)]|_d^2 \, dt \,. \tag{B.14}$$

Appendix C. Sum rules

In this appendix, we derive the generalized Hannay-Ozorio de Almeida sum rules [46, 47] that we need in order to evaluate energy averages of squares of the Green function in the diagonal approximation. To keep the derivation as general as possible, we introduce a new parametrization of the initial and final phase space points according to $(\mathbf{p}, \mathbf{r}) \equiv (\xi_1, \xi_2, \xi_3, \xi_4)$ and $(\mathbf{p}', \mathbf{r}') \equiv (\eta_1', \eta_2', \eta_3', \eta_4')$ where the sets $(\xi_1, \xi_2, \xi_3, \xi_4)$ and $(\eta_1', \eta_2,' \eta_3,' \eta_4')$ contain the components (p_x, p_y, x, y) and (p_x', p_y', x', y') of the final and initial phase space points, respectively, in some arbitrary order. We shall now be interested in the Green function from the coordinates (η_1', η_2') to the coordinates (ξ_1, ξ_2). In the diagonal approximation, the energy average of the modulus square of this Green function reads

$$\left\langle |G[(\xi_1, \xi_2), (\eta_1', \eta_2'), E]|^2 \right\rangle_d = \sum_\gamma \left\langle |A_\gamma[(\xi_1, \xi_2), (\eta_1', \eta_2'), E]|^2 \right\rangle \tag{C.1}$$

$$= \frac{1}{2\pi\hbar^3} \sum_\gamma \left\langle \left| \det \frac{\partial [(p_x', p_y'), (x', y'), T]}{\partial [(\xi_1, \xi_2), (\eta_1', \eta_2'), E]} \right| \right\rangle \,. \tag{C.2}$$

We furthermore need the corresponding expression for the crossed average which includes, in addition, a magnetic dephasing. This yields

$$\langle G^*[(\eta_1', \eta_2'), (\xi_1, \xi_2), E] \, G[(\xi_1, \xi_2), (\eta_1', \eta_2'), E] \rangle_c =$$
$$= \sum_\gamma \left\langle |A_\gamma[(\xi_1, \xi_2), (\eta_1', \eta_2'), E]|^2 \right\rangle \exp\left(-\frac{T_\gamma}{\tau_B}\right) \tag{C.3}$$

$$= \frac{1}{2\pi\hbar^3} \sum_\gamma \left\langle \left| \det \frac{\partial [(p_x', p_y'), (x', y'), T]}{\partial [(\xi_1, \xi_2), (\eta_1', \eta_2'), E]} \right| \right\rangle \exp\left(-\frac{T_\gamma}{\tau_B}\right) \tag{C.4}$$

where $\tau_B \sim B^{-2}$ [see Eq. (53)] is the dephasing time.

Applying standard rules for multidimensional integrations over δ-distributions, we can derive

$$\sum_\gamma \left| \det \frac{\partial[(p'_x, p'_y), (x', y'), T]}{\partial[(\xi_1, \xi_2), (\eta'_1, \eta'_2), E]} \right| f(T_\gamma) \;=\; \int d\xi_3 \int d\xi_4 \int d\eta'_3 \int d\eta'_4 \int_0^\infty dT \delta\left[E - H_0(\mathbf{p}', \mathbf{r}')\right]$$

$$\times \delta\left[\mathbf{r} - \mathbf{q}(\mathbf{p}', \mathbf{r}', T)\right] \delta\left[\mathbf{p} - \mathbf{p}(\mathbf{p}', \mathbf{r}', T)\right] f(T) \quad \text{(C.5)}$$

for any $f(T)$, where we define $\mathbf{q}(\mathbf{p}', \mathbf{r}', T) \equiv (q_x, q_y)(\mathbf{p}', \mathbf{r}', T)$ and $\mathbf{p}(\mathbf{p}', \mathbf{r}', T) \equiv (p_x, p_y)(\mathbf{p}', \mathbf{r}', T)$ as the position and momentum variables that result from the propagation of a classical trajectory over time T with the initial values $\mathbf{p}' \equiv (p'_x, p'_y)$ and $\mathbf{r}' \equiv (x', y')$. Furthermore, assuming classical ergodicity, which is valid if the dynamics within the billiard is fully chaotic, we can state that each phase-space point $(\mathbf{p}, \mathbf{r})$ within the billiard has equal probability to be hit by a given trajectory after a given evolution time T, provided it lies within the shell of constant energy E. This probability, however, decreases exponentially with the evolution time, due to the possibility for escape from the billiard via the openings. We therefore obtain

$$\left\langle \delta\left[\mathbf{r} - \mathbf{q}(\mathbf{p}', \mathbf{r}', T)\right] \delta\left[\mathbf{p} - \mathbf{p}(\mathbf{p}', \mathbf{r}', T)\right] \right\rangle = \frac{\delta\left[H_0(\mathbf{p}', \mathbf{r}') - H_0(\mathbf{p}, \mathbf{r})\right]}{\int d^2 p \int d^2 q \, \delta\left[H_0(\mathbf{p}', \mathbf{r}') - H_0(\mathbf{p}, \mathbf{q})\right]} \exp\left(-\frac{T}{\tau_D}\right)$$

$$\text{(C.6)}$$

where the "dwell time" τ_D corresponds to the mean evolution time that a classical trajectory spends within the billiard before escaping to one of the waveguides. This altogether yields

$$\left\langle \left|G\left[(\xi_1, \xi_2), (\eta'_1, \eta'_2), E\right]\right|^2 \right\rangle_{\mathrm{d}} = \frac{\tau_D}{2\pi\hbar^3} \frac{\int d\xi_3 \int d\xi_4 \delta\left[E - H_0(\mathbf{p}, \mathbf{r})\right] \int d\eta'_3 \int d\eta'_4 \delta\left[E - H_0(\mathbf{p}', \mathbf{r}')\right]}{\int d^2 p \int d^2 q \, \delta\left[E - H_0(\mathbf{p}, \mathbf{q})\right]}$$

$$\text{(C.7)}$$

and

$$\left\langle G^*\left[(\eta'_1, \eta'_2), (\xi_1, \xi_2), E\right] G\left[(\xi_1, \xi_2), (\eta'_1, \eta'_2), E\right] \right\rangle_{\mathrm{c}} = \frac{1}{1 + \tau_D/\tau_B} \left\langle \left|G\left[(\xi_1, \xi_2), (\eta'_1, \eta'_2), E\right]\right|^2 \right\rangle_{\mathrm{d}} . $$

$$\text{(C.8)}$$

The phase space integrals appearing in Eq. (C.7) can be straightforwardly computed. We obtain

$$\int d^2 q \, \delta\left[E - H_0(\mathbf{p}, \mathbf{q})\right] \;=\; \Omega \delta\left(E - \frac{p^2}{2m}\right) , \quad \text{(C.9)}$$

$$\int d^2 p \, \delta\left[E - H_0(\mathbf{p}, \mathbf{q})\right] \;=\; 2\pi m \chi_\Omega(\mathbf{q}) , \quad \text{(C.10)}$$

$$\int d^2 p \int d^2 q \, \delta\left[E - H_0(\mathbf{p}, \mathbf{q})\right] \;=\; 2\pi m \Omega , \quad \text{(C.11)}$$

where $\chi_\Omega(\mathbf{q})$ represents the characteristic function of the scattering system and Ω denotes the area of the billiard. Furthermore, for the case of "mixed" initial or final conditions $\mathbf{z} \equiv (x_L, p_y)$ specified within the incident lead, we calculate

$$\int dy \int dp_x \delta\left[E - H_0(\mathbf{p}, \mathbf{q})\right] = \int_0^W dy \int_0^\infty dp_x \delta\left(E - \frac{p_x^2 + p_y^2}{2}\right) = \frac{mW}{\sqrt{2mE - p_y^2}} . \quad \text{(C.12)}$$

60

Here the longitudinal momentum p_x is restricted to positive (or negative) values corresponding to an initial (or final) condition with an incoming (or outgoing) trajectory. The width W of the waveguide is to be replaced by $\tilde{W}$ in the case of a final condition within the transmitted lead.

Putting these ingredients together and specifying the choice of the phase space variables (ξ_1, ξ_2) and (η_1, η_2) that appear as arguments in the Green function, we finally obtain

$$\left\langle \left| \overline{G}\left(\mathbf{r}, \mathbf{z}', E\right) \right|^2 \right\rangle_{\mathrm{d}} = \frac{\tau_D}{\tau_H} \left(\frac{m}{\hbar^2} \right)^2 \chi_\Omega(\mathbf{r}) \frac{W}{2\pi} \frac{1}{\sqrt{2mE - p_y'^2}} , \tag{C.13}$$

$$\left\langle \left| \widetilde{G}\left(\mathbf{z}, \mathbf{r}, E\right) \right|^2 \right\rangle_{\mathrm{d}} = \frac{\tau_D}{\tau_H} \left(\frac{m}{\hbar^2} \right)^2 \chi_\Omega(\mathbf{r}) \frac{\tilde{W}}{2\pi} \frac{1}{\sqrt{2mE - p_y^2}} , \tag{C.14}$$

$$\left\langle \left| \widetilde{\overline{G}}\left(\mathbf{z}, \mathbf{z}', E\right) \right|^2 \right\rangle_{\mathrm{d}} = \frac{\tau_D}{\tau_H} \left(\frac{m}{\hbar^2} \right)^2 \frac{W\tilde{W}}{(2\pi)^2} \frac{1}{\sqrt{2mE - p_y^2}} \frac{1}{\sqrt{2mE - p_y'^2}} \tag{C.15}$$

for $\mathbf{z}$, $\mathbf{z}'$ being defined in the transmitted and incident lead, respectively, where $\tau_H \equiv m\Omega/\hbar$ denotes the Heisenberg time of the billiard. The corresponding energy-averaged crossed densities are obtained by a multiplication with the prefactor $(1 + \tau_D/\tau_B)^{-1}$, as is seen from Eq. (C.8).

Appendix D. Analysis of the classical dynamics

The aim of this section is to explain how we numerically determine the classical dwell time τ_D and the dimensionless scaling parameter η appearing in Eq. (58) that characterizes magnetic dephasing. To this end, we compute, with a ray-tracing algorithm, an ensemble of classical trajectories that enter the cavity from the left lead. The initial conditions $(x^{(0)}, y^{(0)}, p_x^{(0)}, p_y^{(0)})$ of these trajectories are randomly selected from the intervals $y^{(0)} \in [0, W]$ and $p_y^{(0)} \in [-p, p]$ in a uniform manner, while we fix $x^{(0)} = x_L$ and $p_x^0 = \sqrt{p^2 - [p_y^{(0)}]^2}$ (with $p \equiv \sqrt{2m\mu}$ the total momentum of the classical particle). The propagation of a trajectory is continued until it exits the billiard via one of the leads.

Fig. D.18 shows, for the case of the annular stadium billiard shown in Fig. 1((b), the numerically obtained probability distributions for the path length L and for the modulus of the directed area $\mathcal{A}$ that is accumulated along the trajectories according to Eq. (49). As it is expected for chaotic motion [44, 81], both probability distributions follow an exponential law after a short transient region. Fitting an exponential decay $P(L) \propto \exp(-L/L_0)$ to the asymptotic behaviour of the probability distribution for the trajectory lengths, we obtain the dwell time via $\tau_D = L_0/v$ with $v \equiv p/m$ the velocity of the particle.

The distribution of directed areas $P(\mathcal{A})$ can be determined from the distribution $P(t, \mathcal{A})$ [see Eq. (51)] via

$$P(\mathcal{A}) = \tau_D^{-1} \int_0^\infty P(t, \mathcal{A}) \exp(-t/\tau_D) dt = \frac{1}{\sqrt{\eta \Omega^{3/2} v \tau_D}} \exp\left[-\frac{2\,|\mathcal{A}|}{\sqrt{\eta \Omega^{3/2} v \tau_D}} \right] \tag{D.1}$$
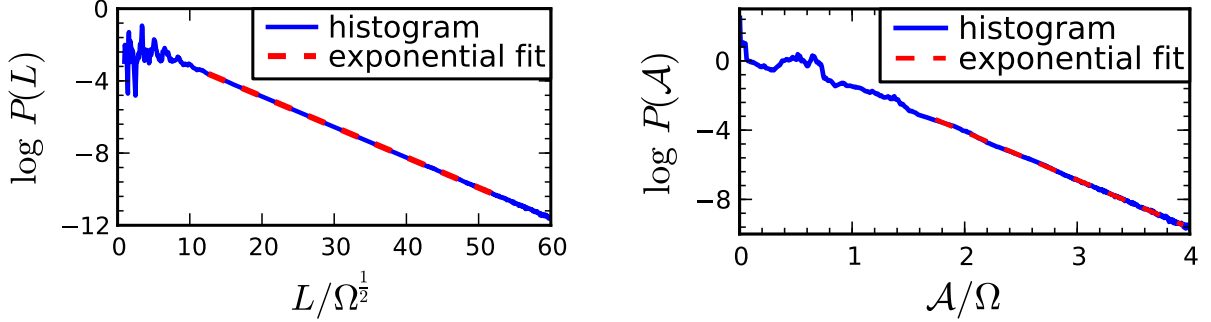
Figure D.18: Probability distributions (blue lines) for the path length L (left panel) and for the directed area $\mathcal{A}$ (right panel) for the case of the the annular stadium billiard shown in Fig. 1((b). Neglecting a short transient region, an exponential decay (red dashed lines) is fitted to these distributions.

and is also predicted to decrease exponentially with $|\mathcal{A}|$ [44, 81]. The exponential decay $P(\mathcal{A}) \propto \exp\left(-|\mathcal{A}|/\mathcal{A}_0\right)$ that is numerically encountered after a short transient region allows us to determine the characteristic scaling parameter via $\eta = 4\mathcal{A}_0^2/(\Omega^{3/2} v \tau_D)$, using the dwell time τ_D that is obtained from the length distribution as explained above.

Comparing the numerically computed dwell time $\tau_D^{(\text{num.})}$ with the "universal" prediction (43), we obtain $\tau_D^{(\text{num.})} \simeq 0.79(\pi\Omega)/[(W + \tilde{W})v]$. This deviation is attributed to the finite width of the leads, which effectively compromises the assumption of ergodic motion that underlies the derivation of Eq. (43). Regular islands of appreciable size, which might also give rise to a deviation of the dwell time from the universal prediction, could not be identified in the phase space of the two billiards.

Appendix E. Frequent integrals in the calculations of loop corrections

Appendix E.1. The standard encounter integral

In this appendix, we calculate the contribution of the encounter region. We first consider the absence of a nonlinearity. The corresponding integral is given by

$$I_1^n(E) = \left\langle \int_{-c}^c ds \int_{-c}^c du \frac{1}{\Sigma(E) t_{\text{enc}}(su)} \exp\left(\frac{i}{\hbar} su\right) \exp\left(-\frac{t_{\text{enc}}(su)}{\tau_n}\right) \right\rangle, \qquad \text{(E.1)}$$

where $1/\tau_n \equiv 1/\tau_D + n/\tau_B$ accounts for the fact that we can have $n \in \{0, 1, 2\}$ stretches with a gauge field dependence within the encounter region, and $\Sigma(E) = 2\pi m\Omega$ is the volume of the energy shell in phase space. Following Ref. [58], we first split the integration over u in two parts,

$$\int_{-c}^c du \ldots = \int_{-c}^0 du \ldots + \int_0^c du \ldots, \qquad \text{(E.2)}$$

and make the variable transformation $(s, u) \mapsto (S, y)$ with $S \equiv su/c^2 \in [-1, 1]$ and $y \equiv c/|u| = \mp c/u \in [1, 1/S]$, with the associated Jacobian determinant c^2/y, where the sign in the definition of y refers to the first and the second integral on the right-hand side of

62

Eq. (E.2), respectively. In physical terms, we transform here from the phase space coordinates s, u to the action difference su measured in terms of c^2, and to a coordinate y related to the time $t_u = (1/\lambda)\ln(c/u)$ needed for the unstable phase space coordinate to evolve from the Poincaré surface of section $\mathcal{P}$ to the limiting value $\mp c$.

As $t_{\text{enc}}(su) = (1/\lambda)\ln(c^2/|su|) = t_{\text{enc}}(|S|)$ does not depend on y, we obtain

$$\int_1^{1/|S|} dy \frac{1}{y} = \ln\left(\frac{1}{|S|}\right) = \lambda t_{\text{enc}}(|S|) \tag{E.3}$$

for the integration over y. We then have

$$
\begin{aligned}
I_1^n(E) &= \left\langle \frac{2c^2\lambda}{\Sigma(E)} \int_{-1}^1 dS \exp\left(\frac{i}{\hbar}Sc^2\right) \exp\left(-\frac{t_{\text{enc}}(|S|)}{\tau_n}\right) \right\rangle \\
&= \left\langle \frac{4c^2\lambda}{\Sigma(E)} \int_0^1 dS \cos\left(\frac{Sc^2}{\hbar}\right) S^{1/(\lambda\tau_n)} \right\rangle \\
&= \left\langle \frac{4\hbar\lambda}{\Sigma(E)} \sin\left(\frac{c^2}{\hbar}\right) \right\rangle - \left\langle \frac{4\hbar}{\Sigma(E)\tau_n} \int_0^1 dS \frac{\sin(Sc^2/\hbar)}{S} S^{1/(\lambda\tau_n)} \right\rangle .
\end{aligned} \tag{E.4}
$$

As the limiting scale c for the coordinates s and u (i.e., the scale until which the linerization around the reference trajectory is still valid) generally depends on the energy E, the first term in Eq. (E.4) is expected to strongly oscillate when varying E and would thus vanish when performing the energy average. For the second term, we obtain after the transformation $S \mapsto S' \equiv Sc^2/\hbar$

$$I_1^n(E) = -\left\langle \frac{4\hbar}{\Sigma(E)\tau_n} \int_0^{c^2/\hbar} dS' \frac{\sin(S')}{S'} \left(\frac{S'\hbar}{c^2}\right)^{1/(\lambda\tau_n)} \right\rangle . \tag{E.5}$$

Assuming that the Ehrenfest time $\tau_E \equiv (1/\lambda)\ln(c^2/\hbar)$ is much smaller than the dwell time τ_D and the magnetic dephasing time scale τ_B, we have $\tau_E \ll \tau_n$ as well as $\lambda\tau_n \gg 1$ and can approximate

$$\left(\frac{S'\hbar}{c^2}\right)^{1/(\lambda\tau_n)} = (S')^{1/(\lambda\tau_n)} \exp\left[-\frac{\tau_E}{\tau_n}\right] \simeq 1 . \tag{E.6}$$

The remaining integral can then be evaluated in the semiclassical limit $\hbar \to 0$ by sending the upper limit of the integration (E.5) to infinity, which finally yields

$$I_1^n(E) = -\frac{4\hbar}{\Sigma(E)\tau_n} \int_0^\infty dS \frac{\sin(S)}{S} = -\frac{2\pi\hbar}{\Sigma(E)\tau_n} = -\frac{1}{\tau_D\tau_H}\left(1 + n\frac{\tau_D}{\tau_B}\right) . \tag{E.7}$$

Appendix E.2. The encounter integral with an embedded nonlinearity event

Now we consider the presence of a nonlinearity event within the encounter region. We first focus on the case that the nonlinearity event is moving along a stretch all the way

Figure E.19: Sketch of the two different possibilities for a nonlinearity event to enter the encounter region. In the scenario depicted on the left-hand side, the nonlinearity event moves along a stretch all the way through the encounter region. On the right-hand side, two of the four encounter stretches end at the nonlinearity block. This gives rise to a reduced encounter duration $\bar{t}_{\mathrm{enc}}(t, u) = t + t_u$ which depends on the time interval t between the nonlinearity event and the Poincaré surface of section $\mathcal{P}$, and on the time $t_u = (1/\lambda)\ln(c/|u|)$ between $\mathcal{P}$ and the borders of the encounter region.

through the encounter region, as depicted on the left-hand side of Fig. E.19. For this case, we have to evaluate the integral

$$
I_2(E) = \left\langle \int\limits_{-c}^{c} \int\limits_{-c}^{c} ds du \frac{1}{\Sigma(E) t_{\mathrm{enc}}(su)} \exp\left(\frac{i}{\hbar} su\right) \exp\left[-\frac{t_{\mathrm{enc}}(su)}{\tau_D}\right] \int_0^{t_{\mathrm{enc}}(su)} dt \exp\left(-\frac{t}{\tau_B}\right) \right\rangle ,
\tag{E.8}
$$

where the additional integration variable t represents the location of the nonlinearity on a stretch within the encounter region. The gauge field dependence, manifested by the dephasing factor $\exp(-t/\tau_B)$, emerges from the stretch along which the nonlinearity moves. We have

$$
\int_0^{t_{\mathrm{enc}}} dt \exp\left(-\frac{t}{\tau_B}\right) = \tau_B \left[1 - \exp\left(-\frac{t_{\mathrm{enc}}}{\tau_B}\right)\right] ,
\tag{E.9}
$$

which would also be obtained if the integrand in Eq. (E.8) was $\exp[-(t_{\mathrm{enc}} - t)/\tau_B]$, corresponding to the case that the other part of the stretch guiding the nonlinearity event would provide the gauge field dependence. Using the results from section Appendix E.1, we obtain

$$
I_2(E) = \tau_B \left[I_1^0(E) - I_1^1(E)\right] = \frac{1}{\tau_H} .
\tag{E.10}
$$

We now analyze the second scenario, shown on the right-hand side of Fig. E.19, where stretches of the encounter region terminate at a nonlinearity. The integral that has to be evaluated in this case is given by

$$
I_3^n(E) = \left\langle \int\limits_{-c}^{c} \int\limits_{-c}^{c} ds du \int_0^{(1/\lambda)\ln(c/|s|)} dt \frac{1}{\Sigma(E) \bar{t}_{\mathrm{enc}}(t, u)} \exp\left(\frac{i}{\hbar} su\right) \exp\left(-\frac{\bar{t}_{\mathrm{enc}}(t, u)}{\tau_n}\right) \right\rangle ,
\tag{E.11}
$$

where we define $\bar{t}_{\mathrm{enc}}(t, u) \equiv t + (1/\lambda)\ln(c/|u|)$ as the reduced encounter time and $1/\tau_n \equiv 1/\tau_D + n/\tau_B$, with $n = 0, 1, 2$ the number of pairs of imbalanced stretches that give rise to a

gauge field dependence. As indicated in Fig. E.19, the integration variable t represents the time between the nonlinearity and the Poincaré surface of section $\mathcal{P}$ within which the stable and unstable coordinates are defined.

Following Refs. [58, 59, 60], we split, as in Section Appendix E.1, the integration over u according to Eq. (E.2) and make the variable transformation $(s, u, t) \mapsto (S, y, \bar{t})$ with $S \equiv su/c^2 \in [-1, 1]$, $\bar{t} \equiv \bar{t}_{\text{enc}}(t, u) = t + (1/\lambda)\ln(c/|u|) \in [0, (1/\lambda)\ln(1/|S|)]$, and $y \equiv c/|u| \in [1, \exp(\lambda\bar{t})]$, with the associated Jacobian determinant c^2/y. The integration over y yields

$$\int_1^{\exp(\lambda\bar{t})} dy \frac{1}{y} = \lambda\bar{t}\,. \tag{E.12}$$

We then evaluate

$$
\begin{aligned}
I_3^n(E) &= \left\langle \frac{2c^2\lambda}{\Sigma(E)} \int_{-1}^1 dS \int_0^{(1/\lambda)\ln(1/|S|)} d\bar{t}\, \exp\left(\frac{i}{\hbar}Sc^2\right) \exp\left(-\frac{\bar{t}}{\tau_n}\right) \right\rangle \\
&= \left\langle \frac{2c^2\lambda\tau_n}{\Sigma(E)} \int_{-1}^1 dS \left[1 - |S|^{1/(\tau_n\lambda)}\right] \exp\left(\frac{i}{\hbar}Sc^2\right) \right\rangle \\
&= \left\langle \frac{4c^2\lambda\tau_n}{\Sigma(E)} \left[\frac{\hbar}{c^2}\sin\left(\frac{c^2}{\hbar}\right) - \int_0^1 dS \cos\left(\frac{Sc^2}{\hbar}\right) S^{1/(\tau_n\lambda)}\right] \right\rangle\,.
\end{aligned} \tag{E.13}
$$

The first contribution in the last line of Eq. (E.13) vanishes when performing the energy average, whereas the second term yields $[-(\hbar\pi)/(2\lambda c^2\tau_n)]$, as seen in Section Appendix E.1. We thus obtain

$$I_3^n(E) = \frac{4c^2\lambda\tau_n}{\Sigma(E)} \frac{\hbar\pi}{2\lambda c^2\tau_n} = \frac{2\pi\hbar}{\Sigma(E)} = \frac{1}{\tau_H}\,. \tag{E.14}$$
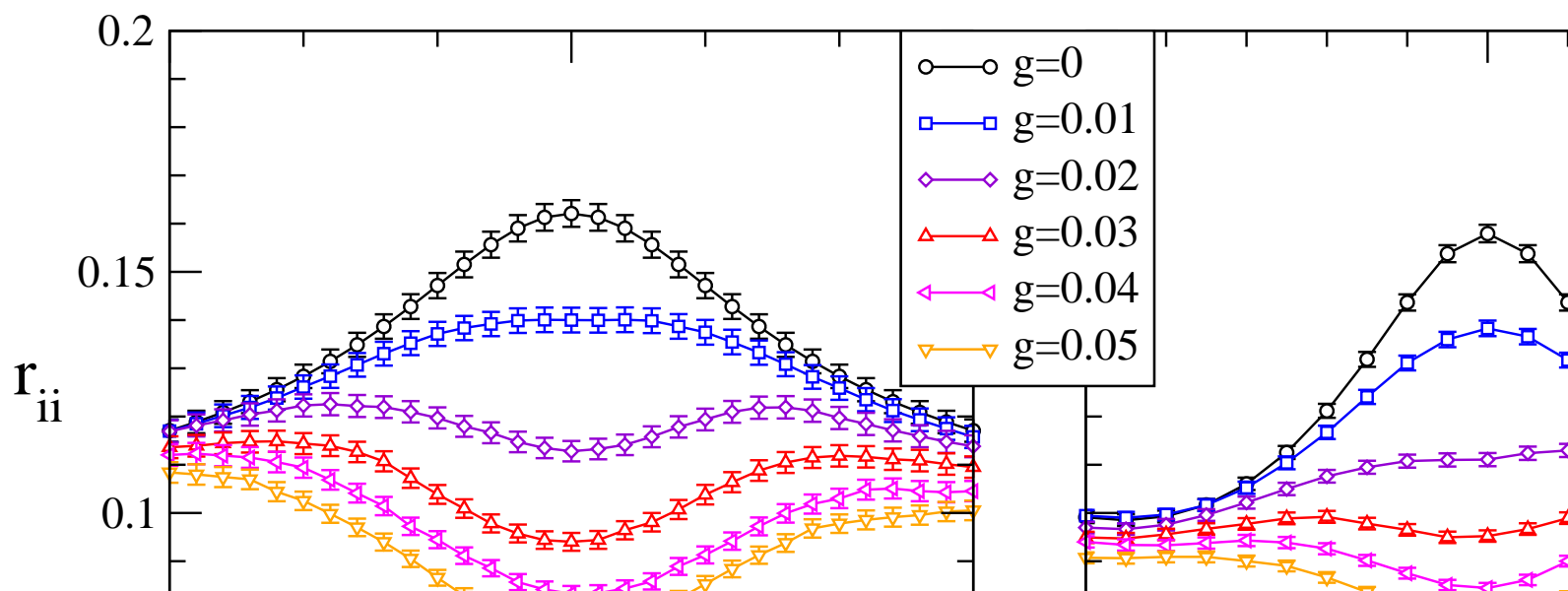
References

References
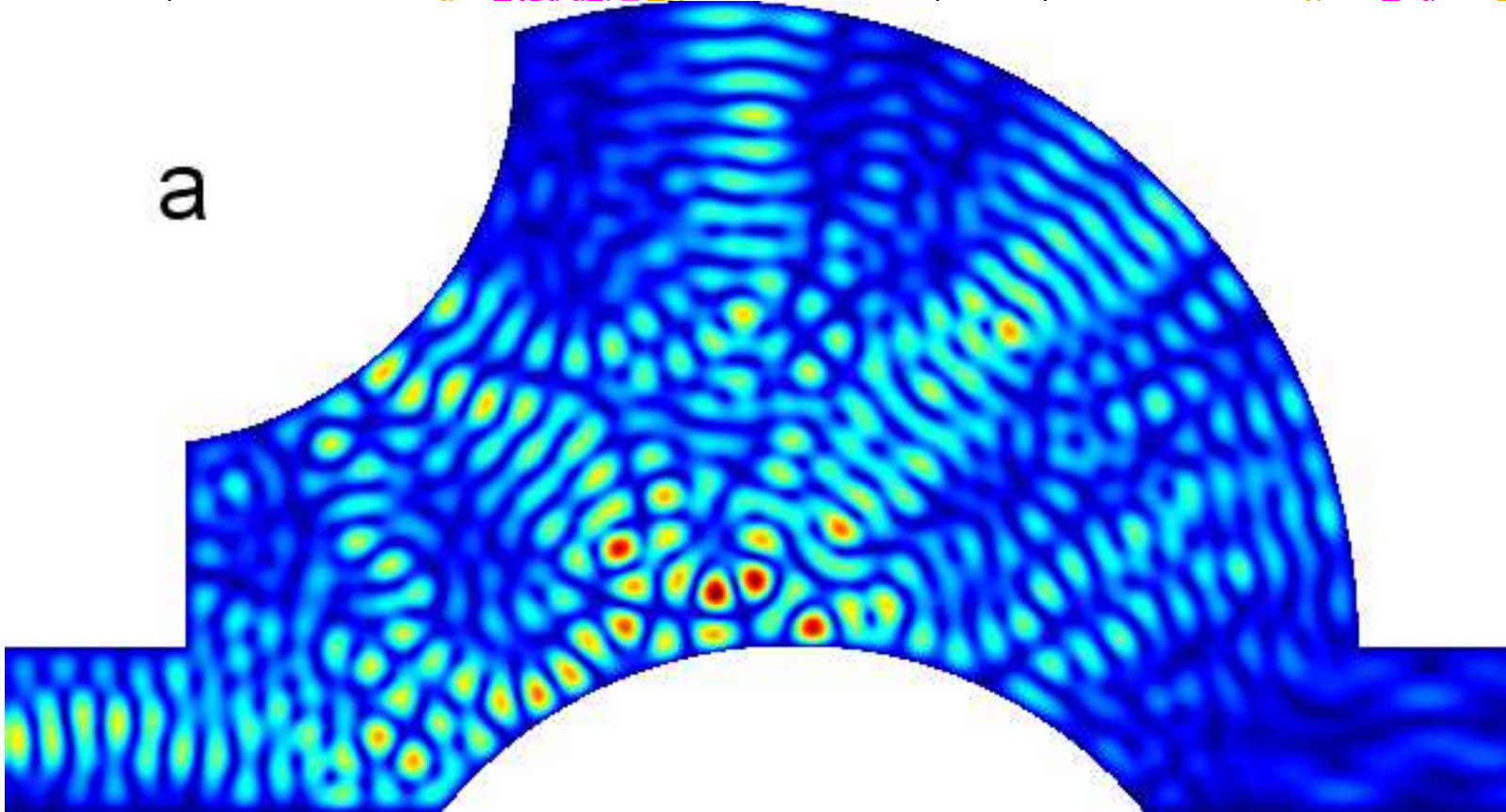
[1] R. Dumke, T. Müther, M. Volk, W. Ertmer, G. Birkl, Phys. Rev. Lett. 89 (2002) 220402.

[2] R. Folman, P. Krüger, D. Cassettari, B. Hessmo, T. Maier, J. Schmiedmayer, Phys. Rev. Lett. 84 (2000) 4749.

[3] J. Fortágh, C. Zimmermann, Rev. Mod. Phys. 79 (2007) 235.

[4] W. Guerin, J.-F. Riou, J. P. Gaebler, V. Josse, P. Bouyer, A. Aspect, Phys. Rev. Lett. 97 (2006) 200402.

[5] A. Couvert, M. Jeppesen, T. Kawalec, G. Reinaudi, R. Mathevet, D. Guéry-Odelin, EPL 83 (2008) 50001.

[6] V. Milner, J. L. Hanssen, W. C. Campbell, M. G. Raizen, Phys. Rev. Lett. 86 (2001) 1514.

[7] N. Friedman, A. Kaplan, D. Carasso, N. Davidson, Phys. Rev. Lett. 86 (2001) 1518.

[8] K. Henderson, C. Ryu, C. MacCormick, M. G. Boshier, New J. Phys. 11 (2009) 043030.

[9] J. Billy, V. Josse, Z. Zuo, A. Bernard, B. Hambrecht, P. Lugan, D. Clément, L. Sanchez-Palencia, P. Bouyer, A. Aspect, Nature 453 (2008) 891.

[10] G. Roati, C. D'Errico, L. Fallani, M. Fattori, C. Fort, M. Zaccanti, G. Modugno, M. Modugno, M. Inguscio, Nature 453 (2008) 895.

[11] A. Stibor, S. Kraft, T. Campey, D. Komma, A. Günther, J. Fortágh, C. J. Vale, H. Rubinsztein-Dunlop, C. Zimmermann, Phys. Rev. A 76 (2007) 033614.

[12] Y.-J. Lin, R. L. Compton, A. R. Perry, W. D. Phillips, J. V. Porto, I. B. Spielman, Phys. Rev. Lett. 102 (2009) 130401.

[13] G. Juzeliūnas, P. Öhberg, J. Ruseckas, A. Klein, Phys. Rev. A 71 (2005) 053614.

[14] J. Ruseckas, G. Juzeliūnas, P. Öhberg, M. Fleischhauer, Phys. Rev. Lett. 95 (2005) 010404.

[15] J. Dalibard, F. Gerbier, G. Juzeliūnas, P. Öhberg, Rev. Mod. Phys. 83, 1523 (2011) 83 (2011) 1523.

[16] B. L. Altshuler, D. Khmel'nitzkii, A. I. Larkin, P. A. Lee, Phys. Rev. B 22 (1980) 5142.

[17] G. Bergmann, Phys. Rep. 107 (1984) 1.

[18] M. P. Van Albada, A. Lagendijk, Phys. Rev. Lett. 55 (1985) 2692.

[19] P.-E. Wolf, G. Maret, Phys. Rev. Lett. 55 (1985) 2696.

[20] A. G. Aronov, Y. V. Sharvin, Rev. Mod. Phys. 59 (1987) 755.

[21] A. M. Chang, H. U. Baranger, L. N. Pfeiffer, K. W. West, Phys. Rev. Lett. 73 (1994) 2111.

[22] B. L. Altshuler, A. G. Aronov, D. E. Khmelnitsky, J. Phys. C: Solid State Phys. 15 (1982) 7367.

[23] B. L. Altshuler, A. G. Aronov, in: A. L. Efros, M. Pollak (Eds.), Electron-electron interaction in disordered systems, Elsevier, Amsterdam, 1985, p. 1.

[24] R. S. Whitney, P. Jacquod, C. Petitjean, Phys. Rev. B 77 (2008) 045315.

[25] M. Hartung, T. Wellens, C. A. Müller, K. Richter, P. Schlagheck, Phys. Rev. Lett. 101 (2008) 020603.

[26] D. M. Zumbühl, J. B. Miller, C. M. Marcus, K. Campman, A. C. Gossard, Phys. Rev. Lett. 89 (2002) 276803.

[27] H. U. Baranger, R. A. Jalabert, A. D. Stone, Chaos 3 (1993) 665.

[28] K. Richter, M. Sieber, Phys. Rev. Lett. 89 (2002) 206801.

[29] S. Heusler, S. Müller, P. Braun, F. Haake, Phys. Rev. Lett. 96 (2006) 066804.

[30] T. Wellens, B. Grémaud, Phys. Rev. Lett. 100 (2008) 033902.

[31] T. Wellens, B. Grémaud, Phys. Rev. A 80 (2009) 063827.

[32] T. Wellens, Applied Physics B 95 (2009) 189.

[33] P. Leboeuf, N. Pavloff, Phys. Rev. A 64 (2001) 033602.

[34] R. Landauer, IBM J. Res. Dev. 1 (1957) 223.

[35] R. Landauer, Philos. Mag. 21 (1970) 863.

[36] M. Büttiker, Y. Imry, R. Landauer, S. Pinhas, Phys. Rev. B 31 (1985) 6207.

[37] F. Dalfovo, S. Giorgini, L. P. Pitaevskii, S. Stringari, Rev. Mod. Phys. 71 (1999) 463.

[38] T. Ernst, T. Paul, P. Schlagheck, Phys. Rev. A 81 (2010) 013631.

[39] S. E. Skipetrov, R. Maynard, Phys. Rev. Lett. 85 (2000) 736.

[40] B. Spivak, A. Zyuzin, Phys. Rev. Lett. 84 (2000) 1970.

[41] T. Paul, P. Leboeuf, N. Pavloff, K. Richter, P. Schlagheck, Phys. Rev. A 72 (2005) 063621.

[42] At the largest value $g = 0.1$ of the nonlinearity that we consider, we find stable solutions for about 95 percent of all choices of the billiard geometry, the chemical potential, and the effective magnetic field.

[43] M. C. Gutzwiller, Chaos in Classical and Quantum Mechanics, Springer, New York, 1990.

[44] R. A. Jalabert, in: G. Casati, I. Guarneri, U. Smilansky (Eds.), Proceedings of the International School of Physics "Enrico Fermi" Course CXLIII, IOS Press, Amsterdam, 2000, p. 145.

[45] K. Richter, Semiclassical Theory of Mesoscopic Quantum Systems, Springer, Heidelberg, 2000.

[46] J. H. Hannay, A. M. Ozorio De Almeida, J. Phys. A: Math. Gen. 17 (1984) 3429.

[47] M. Sieber, J. Phys. A: Math. Gen. 32 (1999) 7679.

[48] K. Richter, D. Ullmo, R. A. Jalabert, Phys. Rev. B 54, R5219 (1996) 54 (199) R5219.

[49] This would be different in the presence of a *complex* nonlinearity strength $g \neq g^*$, which arises in the case of nonlinear photonic transport through atomic disorder geometries [32].

[50] In the case that the point $\mathbf{r}$ cannot be connected to $\mathbf{r}_L$ by a straight-line trajectory due to geometric reasons (e.g. because such a trajectory would cross boundaries of the billiard), one can alternatively define another trajectory for the point $\mathbf{r}$ that leads from there to $\mathbf{r}_L$ within a few bounces.

[51] S. Müller, S. Heusler, P. Braun, F. Haake, New J. Phys. 9 (2007) 12.

[52] M. Sieber, K. Richter, Phys. Scr. T90 (2001) 128.

[53] M. Sieber, J. Phys. A: Math. Gen. 35 (2002) L613.

[54] M. Turek, K. Richter, J. Phys. A: Math. Gen. 36 (2003) L455.

[55] D. Spehner, J. Phys. A: Math. Gen. 36 (2003) 7269.

[56] S. Müller, S. Heusler, P. Braun, F. Haake, A. Altland, Phys. Rev. E 72 (2005) 046207.

[57] Note that our results are also valid for the general hyperbolic case. For this case one then has to use the asymptotic Lyapunov exponent for long trajectories, as e.g. done in [54].

[58] P. W. Brouwer, S. Rahav, Phys. Rev. B 74 (2006) 075322.

[59] D. Waltner, M. Gutiérrez, A. Goussev, K. Richter, Phys. Rev. Lett. 101 (2008) 174101.

[60] M. Gutiérrez, D. Waltner, J. Kuipers, K. Richter, Phys. Rev. E 79 (2009) 046212.

[61] T. Paul, K. Richter, P. Schlagheck, Phys. Rev. Lett. 94 (2005) 020404.

[62] In preparation.

[63] D. K. Ferry, S. M. Goodnick, Transport in Nanostructures, Cambridge University Press, Cambridge, first edition, 1997.

[64] S. Datta, Electronic Transport in Mesoscopic Systems, Cambridge University Press, Cambridge, 2007.

[65] D. Sánchez, M. B¨ttiker, Phys. Rev. Lett. 93 (2004) 106802.

[66] G. M. Gusev, Z. D. Kvon, E. B. Olshanetsky, A. Y. Plotnikov, EPL 88 (2009) 47007.

[67] F. Eckert, Transport in non-linear disordered media, Master's thesis, Universität Freiburg, 2010.

[68] R. Peierls, Z. Phys. A 80 (1933) 763.

[69] T. Paul, M. Hartung, K. Richter, P. Schlagheck, Phys. Rev. A 76 (2007) 063605.

[70] In a physical realization of this transport setup, this can be accomplished e.g. by varying the lateral confinement of the leads.

[71] P. A. Lee, D. S. Fisher, Phys. Rev. Lett. 47 47 (1981) 882.

[72] J. Nocedal, S. J. Wright, Numerical Optimization, Springer, Berlin, second edition, 2006.

[73] R. Seydel, From Equilibrium to Chaos - Practical Bifurcation and Stability Analysis, Elsevier, Amsterdam, 1988.

[74] Formally, we set $g(\mathbf{r}) \equiv g g_0(\mathbf{r})$ and vary g while keeping $g_0(\mathbf{r})$ fixed.

[75] We assume that the derivative $\mathcal{D}F$ has full rank on all solutions of $F(\psi; g) = 0$. Cases in which this assumption fails are very rare. This can happen at bifurcations or cusps.

[76] In practice, a single sweep of the nonlinearity strength is sufficent to compute all relevant scattering states within a finite interval $0 \le g \le g_{\max}$.

[77] C. J. Pethick, H. Smith, Bose-Einstein Condensation in Dilute Gases, Cambridge University Press, Cambridge, 2002.

[78] R. B. Lehoucq, D. C. Sorensen, C. Yang, ARPACK Users' Guide: Solution of Large Scale Eigenvalue Problems with Implicitly Restarted Arnoldi Methods, Siam, 1997.

[79] N. Moiseyev, Phys. Rep. 302 (1998) 212–293.

[80] O. Bohigas, M.-J. Giannoni, A. M. Ozorio de Almeida, C. Schmit, Nonlinearity 8 (1995) 203.

[81] R. V. Jensen, Chaos 1 (1991) 101.

Legend:
- g=0
- g=0.01
- g=0.02
- g=0.03
- g=0.04
- g=0.05

a

b